SCIENCE • TECHNOLOGY • RESEARCH HIGHLIGHTS • VISIONS
22

RANS analyses of cavitating propeller flows

Tuomas Sipilä

VTT

VTT SCIENCE 22

RANS analyses of cavitating propeller flows

Tuomas Sipilä

Licentiate's Thesis submitted in partial fulfilment of the requirements for the degree of Licentiate of Science in Technology at the Aalto University School of Engineering, on the 10th of September, 2012.

ISBN 978-951-38-7946-4 (soft back ed.)
ISSN 2242-119X (soft back ed.)

ISBN 978-951-38-7947-1 (URL: http://www.vtt.fi/publications/index.jsp)
ISSN 2242-1203 (URL: http://www.vtt.fi/publications/index.jsp)

JULKAISIJA – UTGIVARE – PUBLISHER

VTT
PL 1000 (Tekniikantie 4 A, Espoo)
02044 VTT
Puh. 020 722 111, faksi 020 722 7001

VTT
PB 1000 (Teknikvägen 4 A, Esbo)
FI-2044 VTT
Tfn. +358 20 722 111, telefax +358 20 722 7001

VTT Technical Research Centre of Finland
P.O. Box 1000 (Tekniikantie 4 A, Espoo)
FI-02044 VTT, Finland
Tel. +358 20 722 111, fax +358 20 722 7001

Technical editing Anni Repo

Kopijyvä Oy, Kuopio 2012

RANS analyses of cavitating propeller flows

Kavitoivien potkurivirtausten RANS-analyysi. **Tuomas Sipilä.** Espoo 2012. VTT Science 22. 136 p.

Abstract

This publication presents validation studies for the cavitation model implemented in the Reynolds-averaged Navier-Stokes equation solver FINFLO. The validation studies relate to ship propellers in uniform and non-uniform inflow conditions.

The main physical phenomena involved in cavitation are first introduced. Then, the cavitation phenomena related to marine applications are presented, and the physics behind sheet and vortex cavitation are explained. As cavitating flows are strongly related to turbulence, the physics behind turbulence and its simulation methods are also introduced.

The benefits and uncertainties related to cavitation tests are described. It is important to understand the drawbacks of experimental methods when comparing the simulation results with the test observations. A brief description of the existing cavitation models is also given, and the utilized cavitation model and its numerical implementation are described in detail.

The validation cases are introduced and the simulation results are compared to the outcome of the cavitation tests. The simulation results generally showed good correlation with the experiments. Sheet cavitation was observed in the tests on both the suction and pressure sides of the blades in the validation cases, which was also found in the simulations. The cavitating tip vortices were also found to be similar in the experiments and simulations. The propeller slipstream must be discretized with a high resolution grid in order to predict the cavitating tip vortices and the wakes of the blades with reasonable accuracy.

A verification and validation analysis was performed for the global propeller performance characteristics according to the methodology recommended by the ITTC. The influence of the empirical constants in the utilized mass transfer model on the cavitating tip vortices is studied.

Finally, explanations for the similarities and differences between the results of the experiments and the simulations are discussed. The main differences are found to be caused by laminar flow separation at the leading edge of the blades in the tests, and the limitations of the turbulence and cavitation models utilized in the present simulations.

Keywords Cavitation, CFD, hydrodynamics, propeller, RANS, simulation, tip vortex, turbulence

Kavitoivien potkurivirtausten RANS-analyysi

RANS analyses of cavitating propeller flows. **Tuomas Sipilä.** Espoo 2012. VTT Science 22. 136 s.

Tiivistelmä

Työssä on esitetty validointilaskentaa Reynolds-keskiarvoistettujen Navier-Stokes-yhtälöiden ratkaisijaan FINFLOhun implementoituun kavitaatiomalliin. Validointilaskennat liittyvät laivapotkurisovelluksiin sekä tasaisessa että epätasaisessa sisääntulovirtauksessa.

Kavitaatioon liittyvät tärkeimmät fysikaaliset ilmiöt on selitetty opinnäytteen alussa. Tämän jälkeen on esitetty laivasovelluksissa esiin tulevat kavitaatioilmiöt. Levy- ja kärkipyörrekavitaation fysiikka on selitetty tarkasti. Koska kavitaatio liittyy läheisesti virtauksen turbulenttisuuteen, on myös turbulenssin fysiikka ja sen simulointi- ja mallinnusmenetelmät kuvattu.

Kavitaation kokeelliseen tutkimukseen liittyvät edut ja epävarmuudet ovat myös esitetty. On tärkeää ymmärtää kokeelliseen toimintaan liittyvät epävarmuudet, kun verrataan kavitaation simulointituloksia koetuloksiin. Olemassa olevia erilaisia kavitaatiomalleja on lyhyesti kuvattu. Työssä käytetty kavitaatiomalli ja sen numeerinen implementointi on selitetty yksityiskohtaisesti.

Validointitapaukset on esitetty ja simulointituloksia on verrattu kavitaatiokokeiden tuloksiin. Simulointitulokset ovat yleisesti ottaen lähellä kokeellisia tuloksia. Kokeissa ja laskennassa levykavitaatiota havaittiin sekä imu- että painepuolilla lapaa eri validointitapauksissa. Kavitoiva kärkipyörre oli samankaltainen kokeissa ja simulointituloksissa. Jättövirtauksen diskretointi on tehtävä huolellisesti laskennoissa, jotta kavitoiva kärkipyörre sekä lavan vanavesi tulevat mallinnettua tarkoituksenmukaisella tarkkuudella.

Lasketuille potkurin toimintaa kuvaaville globaaleille suureille on tehty verifiointi- ja validointitarkastelu ITTC:n suosittelemalla tavalla. Käytetyssä massansiirtomallissa olevien empiiristen kertoimien vaikutusta kavitoivan kärkipyörteen laskentatuloksiin on myös tutkittu.

Työn lopussa on selitetty syitä kokeellisten ja laskennallisten tulosten vastaavuuksiin ja eroihin. Tärkeimmät syyt tulosten eroihin ovat levykavitaation synnyn viivästyminen kokeissa lavan johtoreunalla ilmenevän laminaarisen virtauksen johdosta sekä simuloinnissa käytettyjen turbulenssi- ja kavitaatiomallien rajoitukset.

Avainsanat Cavitation, CFD, hydrodynamics, propeller, RANS, simulation, tip vortex, turbulence

Preface

This thesis was prepared for Aalto University's Marine Technology research group, and the work described was carried out in the Ship Hydrodynamics team at the Vehicle Engineering knowledge centre of VTT Technical Research Centre of Finland. I wish to extend my gratitude to Professor Jerzy Matusiak, thesis supervisor and examiner, for his valuable input and comments. My sincere thanks also to the second examiner of my thesis, D.Sc. (Tech.) Patrik Rautaheimo, for the valuable comments that helped to improve this thesis.

I also wish to thank Professor Timo Siikonen, instructor of my thesis, for his support and guidance and for our fruitful co-operation over the last decade in the field of computational fluid dynamics.

I am deeply grateful to my VTT colleagues D.Sc. (Tech.) Jaakko Pylkkänen (retired) and D.Sc. (Tech.) Antonio Sánchez-Caja for introducing me to propeller hydrodynamics, for their enthusiasm for the subject and for their unwavering patience in guiding me through the world of ship propulsors.

My special thanks to Jussi Martio – our many discussions on and off topic helped me to persevere during the hard times. A huge thanks to all members of the Ship Hydrodynamics team for creating such a good working atmosphere.

I would also like to acknowledge my sincere gratitude to Esa Salminen and Juho Ilkko of FINFLO Ltd. for their valuable guidance in using FINFLO and its auxiliary programs and for solving the bugs in the codes. My deep thanks also to Tiina Järvilehto from Semantix Finland Ltd. for proofreading this thesis.

The financial support provided for the work of this thesis is gratefully acknowledged. The majority of the work was carried out under the EU's 6th Framework Programme project VIRTUE and the Tekes – the Finnish Funding Agency for Technology and Innovation – project VIRKOOT. These projects created fruitful environments and networks in which to study cavitation using numerical methods. I would like to thank Ilkka Saisto for his expert handling of the red tape related to these projects. The final part of this work was conducted under VTT's self-funded project CFDShip and FIMECC/EFFIMA/SEEE project UNNO.

The experimental validation material utilized in this thesis was provided by SVA Potsdam in Germany and CNR-INSEAN in Italy. These organizations are greatly acknowledged for releasing their experimental data for use by external organizations; good quality experimental validation material is crucial in developing numerical simulation methods of any physical phenomena.

Academic thesis

Supervisor

Professor Jerzy Matusiak
Aalto University
School of Engineering
Department of Applied Mechanics
Tietotie 1 A
P.O.Box 15300
FI-00076 Aalto
Finland

Reviewers

Professor Jerzy Matusiak
Aalto University
School of Engineering
Department of Applied Mechanics
Tietotie 1 A
P.O.Box 15300
FI-00076 Aalto
Finland

D.Sc. (Tech.) Patrik Rautaheimo
STX Finland Oy
P.O.Box 666
FI-20101 Turku
Finland

Contents

List of symbols

Latin symbols

a	Radius of the viscous core of a vortex
A	Area
$\tilde{A}$	Jacobian of a flux vector based on Roe's average
A_E	Expanded area ratio
A_P	Multiplier in the Rhie-Chow interpolation method
A_0	Propeller disk area
c	Speed of sound; chord length
c_p	Specific heat at a constant pressure; sectional pressure coefficient
c_μ	Coefficient in the k-ε model
c_1	Coefficient in the k-ε model
c_2	Coefficient in the k-ε model
C	Integral constant; constant to reduce dissipation in the Rhie-Chow interpolation; constant in the turbulence energy spectrum in the inertial subrange; constant in the Antoine equation
C_{dest}	Evaporation constant in the mass transfer model
CFL	Courant number, $u\Delta t/\Delta x$
C_G	Correction factor for error estimates related to grid convergence
C_i	Correction factor for error estimates
C_k	Coefficient in limiting k between iteration cycles
C_L	Lift coefficient, $\frac{L}{\frac{1}{2}\rho q^2 A}$
C_p	Pressure coefficient, $\frac{p-p_\infty}{\frac{1}{2}\rho q^2}$
C_{prod}	Condensation constant in the mass transfer model

C_S	Smagorinsky coefficient
C_ε	Coefficient in limiting ε between iteration cycles
d_h	Hub diameter
D	Propeller diameter; mass diffusion rate; function in the k-ε model; measured value of an integral variable
D_{ij}	Divergence term in the Reynolds stress model
err	Error between results calculated from different grid resolutions
E	Total internal energy; energy spectrum of turbulence; function in the k-ε model; error between measured and simulated value of an integral variable
E_C	Error between measured and corrected simulated integral value
f	Frequency; weighting function, $\rho_v + \left(\frac{\rho_v - \rho}{\rho_v - \rho_l}\right)^n (\rho_v - \rho_l)$
f_μ	Function in the k-ε model
f_1	Function in the k-ε model
f_2	Function in the k-ε model
F	Pressure function at infinity; inviscid flux vector in the x-direction in the RANS equations
$\vec{F}$	Force; flux
F_v	Viscous flux vector in the x-direction in the RANS equations
$\vec{g}$	Body force
G	Filter function; inviscid flux vector in the y-direction in the RANS equations
G_v	Viscous flux vector in the y-direction in the RANS equations
h	Pressure function; enthalpy; turbulence length scale
h_{DI}	Turbulence length scale at the border of the dissipation range and the inertial subrange
h_{EI}	Turbulence length scale at the border of the energy containing range and the inertial subrange
h_s	Smagorinsky length scale, $C_S \Delta$
h_0	Length scale of the largest visible turbulence eddies
H	Inviscid flux vector in the z-direction in the RANS equations
H_v	Viscous flux vector in the z-direction in the RANS equations
i	Individual cell; grid level
$\vec{\imath}$	Unit vector in the x-direction

$I_{h_{i+1}}^{h_i}$	Interpolation operator between two multigrid levels
$\vec{j}$	Unit vector in the *y*-direction
k	Kinetic energy of turbulence
$\vec{k}$	Unit vector in the *z*-direction
k_r	Residual kinetic energy of turbulence
K	Constant in the McCormick rule
K_g	Gas constant
l	Length
$\vec{l}$	Curvilinear path
L	Lift
$\dot{m}$	Mass flux
n	Rotational rate of the propeller; iteration cycle; constant in the weighting function f
$\vec{n}$	Unit normal vector
N	Number of cells
p	Local pressure; order of accuracy of a numerical simulation
p'	Pressure correction
p_{est}	Estimated order of accuracy
p_{dif}	Pressure difference
p_{eff}	Effective pressure, $p + \frac{2}{3}\rho k = p_{dif} + p_\infty + \frac{2}{3}\rho k$
p_v	Vapour pressure
p_∞	Pressure in undisturbed flow
P	Production of turbulence; forcing function in algebraic multigrid method; pitch
P_{ij}	Production term in the Reynolds stress model
Pr	Prandtl number, $\mu \frac{c_p}{\lambda}$
q	Reference velocity; heat
$\vec{q}$	Heat flux
Q	Source term vector in the RANS-equations
r	Radial distance; grid refinement ratio
$\vec{r}$	Radial vector; distance vector

r_i	Grid refinement ratio
R	Propeller radius; bubble radius; residual
R^c	Residual of the continuity equation
R^E	Residual of energy
R^h	Residual of enthalpy
R^k	Residual of turbulent kinetic energy
R^M	Residual of momentum
R^t	Transfer of the residual in the algebraic multigrid method
R^*	Recalculated residual in the algebraic multigrid method
Re	Reynolds number, $\frac{U_\infty l}{\nu}$
s	Distance between neighbouring cell centres
$\vec{s}$	Unit vector between neighbouring cell centres
S	Surface tension of a bubble; area in a vortex sheet; area of a cell face; simulated value of an integral variable
$\vec{S}$	Boundary
$\bar{S}$	Characteristic filtered rate of strain, $\left(2\bar{S}_{ij}\bar{S}_{ij}\right)^{1/2}$
$\bar{S}_{ij}$	Filtered rate-of-strain tensor, $\frac{1}{2}\left(\frac{\partial \bar{u}_i}{\partial x_j}+\frac{\partial \bar{u}_j}{\partial x_i}\right)$
Sc	Schmidt number, $\frac{\nu}{D}$; corrected simulated value of an integral variable
$S_{C,\phi}$	Extrapolated scalar value at an infinitely dense grid
St	Strouhal number, $\frac{fl}{U_\infty}$
t	Time
T	Temperature; arbitrary function
u	Velocity component in the x-direction
u'	Velocity correction; velocity fluctuation
u_τ	Wall velocity, $\sqrt{\tau_w/\rho}$
U	Variable vector in the RANS equations, $(\rho, \rho u, \rho v, \rho w, E, \rho k, \rho \varepsilon, \rho \phi)^{\mathrm{T}}$; uncertainty of an integral variable
U_D	Uncertainty in measurements
U_G	Uncertainty in grid convergence
U_i	Uncertainty of numerical error
U_I	Uncertainty related to iteration unsteadiness

U_{SN}	Numerical uncertainty in simulation
U^t	Transfer of the residual in the algebraic multigrid method
U_V	Validation error
U^+	Corrected variable after multigrid iteration
U_∞	Inflow speed
v	Velocity component in the y-direction
$\vec{v}$	Velocity in a fixed coordinate system
V	Volume
V_A	Advance speed of a propeller
$\vec{V}_r$	Velocity in a rotating coordinate system
w	Velocity component in the z-direction
x	Local coordinate direction; fluid quality
X	Global coordinate direction
y	Local coordinate direction
Y	Global coordinate direction
y^+	Wall distance, $y_n \frac{\rho u_\tau}{\mu}$
y_n	Normal distance from wall
z	Local coordinate direction
Z	Number of propeller blades; global coordinate direction

Greek symbols

α	Void fraction, $\frac{V_v}{V_w}$; dot product of a surface normal and a connection vector between neighbouring cell centres, $\vec{n}_{i+1/2} \cdot \vec{s}_{i+1/2}$; under-relaxation factor
β	Exponent variable in Burgers vortex equation, $\gamma/4\nu$
γ	Vorticity; Stretching; Exponent constant in the equation of an isentropic process
Γ	Circulation; mass transfer
δ_{ij}	Kronecker delta
$\delta^*_{i,1}$	Corrected error estimate at the infinitely dense grid
$\delta^*_{RE_{i,1}}$	Error estimate at the infinitely dense grid
Δ	Filter length

$\Delta\tilde{x}$	General measure of discretization, $\sqrt[3]{N}$
ε	Dissipation of turbulence; small constant
ε_{ij}	Dissipation term in the Reynolds stress model
$\vec{\zeta}$	Vorticity, $\nabla \times \vec{v}$
η	Kolmogorov length scale
κ	Wave length of a turbulent eddy, $2\pi/h$
λ	Thermal conductivity
μ	Dynamic viscosity, $\rho\nu$
μ_T	Turbulent viscosity
ν	Kinematic viscosity
ν_r	Residual eddy viscosity
Θ	Skew angle
ρ	Density of a fluid
σ	Cavitation number, $\frac{p_\infty - p_v}{\frac{1}{2}\rho q^2}$
σ_k	Coefficient in the k-ε model
τ_{ij}	Stress tensor
τ_{ij}^r	Anisotropic residual-tress tensor
τ_{ij}^R	Residual-stress tensor
τ_w	Wall shear stress
ϕ	Velocity potential; scalar variable
ϕ_{ij}	Pressure-strain term in the Reynolds stress model
ω	Turbulence frequency, ε/k
$\vec{\omega}$	Rotating velocity
$\vec{\Omega}$	Rotational rate

Subscripts

$_B$	Bubble
$_c$	Critical
$_C$	Corrected value
$_{dif}$	Difference

e	Equilibrium
eff	Effective
g	Gas
h_i	Grid level
h_1	Finest grid level
i	Inception; inner
j	Cell face
k	Kinetic energy of turbulence
max	Maximum
p	Pressure
r	Radial
RE	Richardson extrapolation
sat	Saturation
$surf$	Surface
t	Turbulent
tun	Cavitation tunnel
u	Velocity
v	Vapour phase; viscous component
w	Water phase
x	Axial
0	Initial condition
ε	Dissipation of turbulence
θ	Azimuthing
ϕ	Scalar
∞	Ambient condition

Abbreviations

ARSM	Algebraic Reynolds Stress Model
ASME	American Society of Mechanical Engineers
BEM	Boundary Element Method
CEIMM	Italian Navy cavitation facility
CFD	Computational Fluid Dynamics
CICSAM	Compressive Interface Capturing Scheme for Arbitrary Meshes
CNR	National Research Council of Italy
CPP	Controllable Pitch Propeller
CPU	Central Processing Unit
DES	Detached Eddy Simulation
DNS	Direct Numerical Simulation
EARSM	Explicit Algebraic Reynolds Stress Model
FPP	Fixed Pitch Propeller
fps	Frames per second
HUT	Helsinki University of Technology
INSEAN	Italian Ship Model Basin
ITTC	International Towing Tank Conference
LDV	Laser Doppler Velocimetry
LES	Large Eddy Simulation
PHV	Propeller-Hull Vortex
PIV	Particle Image Velocimetry
RANS	Reynolds-Averaged Navier-Stokes
rpm	Rounds per minute
RSM	Reynolds Stress Model
SGS	Subgrid Scale
SVA	Potsdam Model Basin
TEM	Transport Equation-based Method
URANS	Unsteady Reynolds-Averaged Navier-Stokes
VoF	Volume of Fluid
VTT	VTT Technical Research Centre of Finland

1. Introduction

Cavitation can occur in a wide range of technical applications involving fluid flow, such as ship propellers and hull appendages, pumps, diesel engine injection valves, and bearings. The phenomenon can also occur in human tissues. Often, the characteristic crack of a knee when bent suddenly is, in fact, the sound is emitted from a collapsing cavitation bubble. Cavitation is also used in medical science to break kidney stones, for example (Brujan, 2011). Cavitation is also utilized in under-water cleaning, in which the implosions from cavitation caused by the strong jets remove fouling from ship hulls.

The high pressure pulses emitted by collapsing cavitation bubbles cause several well-known, but not necessarily fully understood, phenomena. The collapsing cavitation bubbles emit broadband noise to the environment. In a case where the bubbles collapse in the vicinity of a solid surface, cavitation may cause damage to the material near nearby. Extensive dynamic cavitation can emit high pressure pulses from collapsing bubbles that may excite vibrations in neighbouring structures. Extensive cavitation also alters the main flow field. If the cavitation advances beyond a certain limit, hydrofoil lift is suddenly significantly reduced. Cavitation represents an interesting avenue of research due to the wide range of dynamic phenomena related to it.

This thesis focuses on the numerical simulation of cavitating flows on ship propellers. The contents of the thesis are as follows. The introduction given in Section 1 covers the main physical phenomena related to cavitation and its special aspects in the maritime field. The introduction also covers the methods of predicting turbulence in viscous flows. The methods and models used to study cavitation are also presented in the introduction. Section 2 introduces the utilized numerical models and their implementation in the FINFLO code. The validation cases are described in Section 3, and the results of the simulations are given in Section 4. The discussion of the quality of the simulation results is given in Section 5. Possible explanations for the similarities and differences between the simulation results and the experiments are also discussed. The conclusions and directions for future research are given in Section 6.

1.1 Cavitation physics

This chapter discusses the physics behind the phase transition between liquid and gaseous phases. Whereas the fluid dealt within this thesis is water, the same physical background holds also for other fluids.

1.1.1 Phase transition

Water, as any other pure substance, can exist in three phases: solid, liquid and gas. If the gas temperature of the substance is below its critical temperature, the gas phase is called vapour. Two or more phases can exist simultaneously in a volume. In such cases, the fluid is called a mixture. In phase transition from gas to liquid, from liquid to solid and from gas to solid, heat is released. In phase transition in the opposite direction, heat is absorbed.

Figure 1 shows a three-dimensional surface representation of the quasi-steady processes of a pure substance based on the p,V,T coordinates, where p is pressure, V is volume, and T is temperature. All possible phases and their mixtures are shown in the figure. The three phases are in equilibrium at the triple line between points A and B. In the small extension of the triple line to the left of point A, the vapor+solid and liquid+solid phase pairs are in equilibrium. The plane to the right of the isotherm is the gas phase. The vapour phase is present at temperatures below the critical temperature in the regions depicted by V. The "shoe tongue" shaped region on the surface contains both the liquid and vapour phases. To the left of the "shoe tongue" is the pure liquid phase, a mixture of liquid and solid phases, and the pure solid phase. Below the triple line is the equilibrium region of the solid and vapour phases. In all mixture regions the isotherms are parallel to the V axis, i.e. the pressure depends only on temperature.

Figure 1 also shows projections of the three-dimensional surface in the pT and pV planes. In the pT planes the mixture phase regions on the three-dimensional surface are reduced to lines at which equilibrium exists. The triple line is reduced to a singular point. The boiling line ends at the critical point above which only the gas phase exists. In the pV projection, the region of the mixture of liquid and vapour phases is delimited by the saturated liquid and saturated vapour curves (curves I and II, respectively), and by the triple line.

The phase transition from liquid to vapour is evaporation, and the transition from vapour to water is condensation. Figure 2 illustrates the difference between cavitation and boiling. If the phase transition from liquid to vapour is driven by temperature increase, the phenomenon is called boiling. In a case where evaporation is driven by a pressure decrease, the phenomenon is called cavitation. However, the delimitation between boiling and cavitation is not always clear; evaporation in heat exchangers may be influenced by both pressure and temperature variations. In the marine context, evaporation is driven by a local pressure decrease in water due to induced high velocities on the lifting surfaces.

As seen from Figure 1, the vapour pressure of a fluid varies as a function of temperature. Figure 2 shows the correlation between vapour pressure p_v and temperature T as recommended by the International Towing Tank Committee (ITTC, 2011).

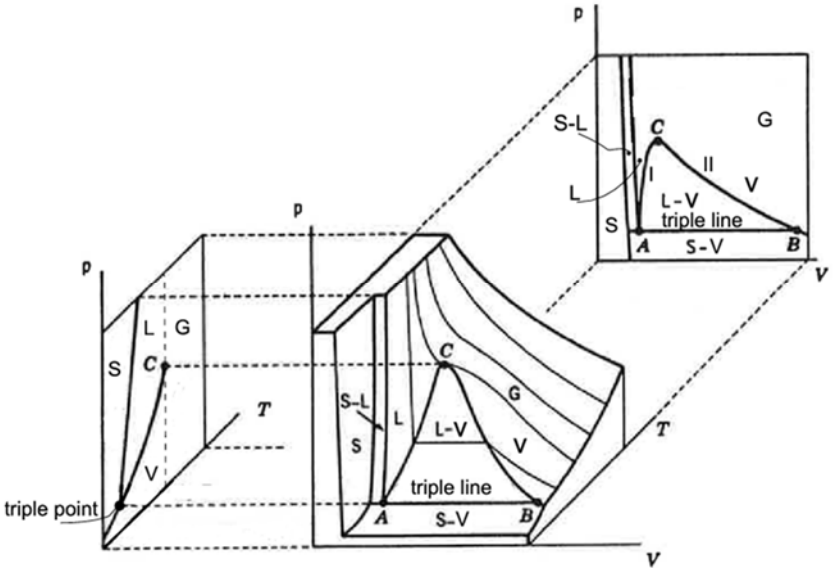

Figure 1. Pressure-Volume-Temperature surface representation of a pure substance. G, L, S and V depict the gas, liquid, solid and vapour phases of the substance, respectively. The critical point is depicted by C. Projections of the surface give the *p-T* diagram on the left and the *p-V* diagram to the rear. (Figure reproduced from Hemilä & Utriainen [1991].)

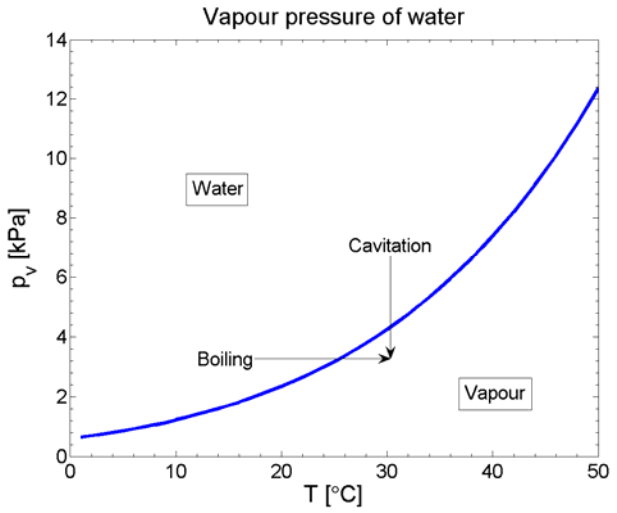

Figure 2. Correlation between vapour pressure and temperature of water as recommended by the ITTC. The delimitation between boiling and cavitation is also illustrated.

Cavitation is often related to a violent behaviour of fluids due to the very rapid processes involved in the evaporation and condensation of cavitating bubbles. The dynamics of cavitation are several magnitudes faster than those of the mean flow.

The growth and collapse of bubbles emit very high pressure peaks in the cavitation region. The cavitating flow structures can travel with the bulk flow to the high pressure regions where large numbers of cavitating bubbles collapse violently and simultaneously. The local velocity of the collapsing bubbles is high enough to exceed the speed of sound in the mixture and shock waves are generated in the fluid.

The speed of sound in a mixture of water and vapour is significantly lower than that in pure water or pure vapour. The speed of sound c is calculated as a function of the void fraction α_v as (Wallis, 1969):

$$\frac{1}{\rho c} = \frac{\alpha_v}{\rho_{v,sat}(T)c_v^2} + \frac{1-\alpha_v}{\rho_{l,sat}(T)c_l^2} \tag{1}$$

where $\rho_{v,sat}$ and $\rho_{l,sat}$ are the saturated densities of the vapour and liquid phases, respectively. The void fraction is the relation between volumes of vapour V_v and liquid V_l in a specific region, i.e. $\alpha_v = \frac{V_v}{V_l}$. At a 25 °C temperature the speed of sound is shown as a function of the void fraction in Figure 3. As the figure shows, the speed of sound is very low between the void fraction α_v = 0.05…0.95. The speed of sound in a mixture is at its lowest c_m = 4 m/s at α_v = 0.5. The speed of sound in pure water (α_v = 0) is c_l = 1542 m/s, and in pure vapour (α_v = 1) c_v = 420 m/s.

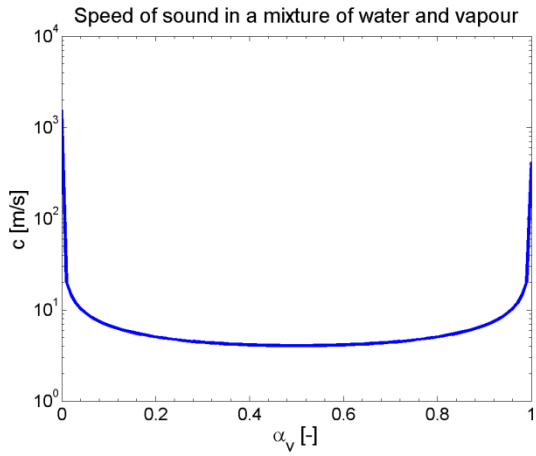

Figure 3. Speed of sound in a mixture of water and vapour as a function of void fraction.

1.1.2 Bubble dynamics

Cavitation does not incept in pure fluids. This is because pure water can sustain even tension (Brennen, 1995) due to the mutual attraction of the water molecules, i.e. cohesion.

The experiments conducted by Briggs (1950) showed that pure water can resist close to 260 bars of tension at 10 °C. However, pure water exists in virtually no practical engineering applications.

Cavitation bubbles are formed from cavitation nuclei, i.e. from tiny bubbles filled with vapour or gas or a combination of these. Water can also contain solid contaminants on which cavitation nuclei can attach. The number of small nuclei in a fluid is higher compared to larger nuclei. This is due to the more stable nature of small bubbles caused by their higher surface tension.

Water also contains dissolved air. Dissolved air has a minimal effect on the cohesive forces of water and thus, in turn, has only a limited effect on the cavitation inception properties of water.

Rayleigh (1917) derived a function for a single collapsing cavitation bubble containing pure vapour. Plesset (1949) later generalized this formulation to also include gas inside the bubble. This formulation is called the Rayleigh-Plesset equation and is referred to in numerous publications dealing with the dynamics of cavitation bubbles, such as Kuiper (1981), Matusiak (1992), Carlton (1994) and Hallander (2002), to mention a few. The derivation of the Rayleigh-Plesset equation below is done following Matusiak (1992).

For a flow with spherical symmetry, the continuity and momentum equations of the Navier-Stokes equations in the differential form are as follows:

$$\frac{\partial \rho_w}{\partial t} + \frac{1}{r^2}\frac{\partial (r^2 \rho_w v_r)}{\partial r} = 0 \tag{2}$$

and

$$\frac{dv_r}{dt} = -\frac{1}{\rho_w}\frac{\partial p}{\partial r} \tag{3}$$

where t is time, r is the radial distance, v_r is the radial velocity, and p is pressure. The fluid is irrotational due to the radial symmetry of the flow. The body forces are neglected.

By using the relation of the material derivative

$$\frac{d\vec{v}}{dt} = \frac{\partial \vec{v}}{\partial t} + \frac{\partial}{\partial r}\left(\frac{\vec{v}^2}{2}\right) \tag{4}$$

the momentum equation in Eq. (3) can be expressed as

$$\frac{\partial v_r}{\partial t} + \frac{\partial}{\partial r}\left(\frac{{v_r}^2}{2}\right) + \frac{1}{\rho_w}\frac{\partial p}{\partial r} = 0 \tag{5}$$

The velocity potential ϕ is defined so that

$$\vec{v} = \nabla\phi \tag{6}$$

By introducing also a pressure function $h(p)$

$$h(p) = \int_{p_\infty}^{p} \frac{dp}{\rho_w(p)} \tag{7}$$

one can present Eq. (5) in the form

$$\frac{\partial\phi}{\partial t} + \frac{1}{2}\left(\frac{\partial\phi}{\partial r}\right)^2 + h = F(t) \tag{8}$$

where $F(t) = \frac{p_\infty(t)}{\rho_{w,\infty}}$ and $h = \frac{p}{\rho_w(p)}$. The external pressure $p_\infty(t)$ far from the bubble is time-dependent. The external pressure consists of atmospheric, static, and dynamic pressures, of which the latter is time-dependent and induced by the motions of the body in the fluid domain.

In a case of an incompressible flow, the continuity equation and Eq. (8) simplify, respectively, to

$$\frac{\partial(r^2 v_r)}{\partial r} = 0 \tag{9}$$

and

$$\frac{\partial\phi}{\partial t} + \frac{1}{2}\left(\frac{\partial\phi}{\partial r}\right)^2 + \frac{p}{\rho_w} = F(t) \tag{10}$$

Integrating Eq. (9) gives the relation

$$v_r = \frac{C}{r^2} \tag{11}$$

here C is an integration constant determining the boundary conditions of the problem. At a spherical bubble wall $r = R$ the radial velocity is the same as the bubble wall velocity. This gives the boundary condition to define C as

$$C = R^2\dot{R} \tag{12}$$

and

$$v_r = \frac{R^2\dot{R}}{r^2} \tag{13}$$

By integrating the radial velocity, the velocity potential of the bubble becomes as follows:

$$\phi = \int \frac{R^2\dot{R}}{r^2} dr = -\frac{R^2\dot{R}}{r} + f(t) \tag{14}$$

where the integration function $f(t)$ is set to zero.

The pressure inside the bubble is calculated as a function of the radial extent of the bubble radius by Eq. (10):

$$p(r,t) = \rho_w \left(\frac{\dot{R}R^2 + 2R\dot{R}^2}{r} - \frac{1}{2}\frac{\dot{R}^2R^4}{r^4} + F(t) \right) \tag{15}$$

On the bubble surface r is equal to R and Eq. (15) becomes

$$R\ddot{R} + \frac{3}{2}\dot{R}^2 = \frac{p_{w,surf}}{\rho_w} - F(t) \tag{16}$$

where $p_{w,surf}$ is the pressure in the fluid at the bubble surface.

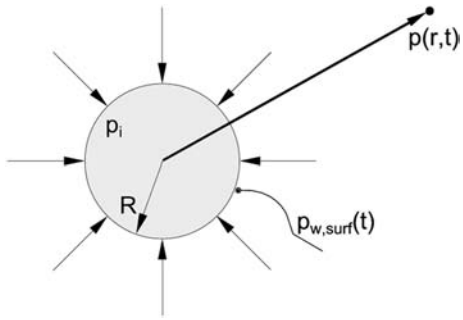

Figure 4. A spherical bubble in a fluid domain.

Figure 4 shows a sketch of a bubble in a fluid domain. In a case of an equilibrium condition the pressure inside the bubble is constant. The net force generated by the pressure difference inside the bubble and just outside the bubble is $F_p(t) = \left(p_i - p_{w,surf}(t)\right)\pi R(t)^2$. This must be compensated by the surface tension S integrated around the bubble circumference as $F_S(t) = 2\pi R(t)S(t)$. In equilibrium conditions, the following thus holds:

$$p_i - p_{w,surf}(t) = \frac{2S(t)}{R(t)} \tag{17}$$

The pressure inside the bubble forms from the vapour pressure and the partial gas pressure:

$$p_i = p_v + p_g \tag{18}$$

It is often acceptable to assume that the gas inside the bubble behaves like an ideal gas. Thus, the pressure changes as a function of volume as

$$p_g V^\gamma = p_{g,0} V_0^\gamma \tag{19}$$

where the initial condition is depicted by the subscript $_0$ and γ is the constant of the isentropic process. For an ideal gas $\gamma = 1.4$.

Now, the pressure on the bubble wall is written as

$$p_{w,surf}(t) = p_v + p_{g,0}\left(\frac{R_0}{R(t)}\right)^{3\gamma} - 2\frac{S(t)}{R(t)} \tag{20}$$

The bubble motion in an incompressible fluid in Eq. (16) is written in its final form as

$$R(t)\ddot{R}(t) + \frac{3}{2}\dot{R}(t)^2 + 2\frac{S(t)}{R(t)} = \frac{p_v - p(t)}{\rho_w} + \frac{p_{g,0}}{\rho_w}\left(\frac{R_0}{R(t)}\right)^{3\gamma} \tag{21}$$

The above equation is the Rayleigh-Plesset equation, from which the growth and collapse of a cavitation bubble can be determined. A more general form of the Rayleigh-Plesset equation including also the thermal and viscous terms of the liquid is found in Brennen (1995) and Hammit (1980), among others.

1.1.3 Bubble stability

The Rayleigh-Plesset equation given in Eq. (21) can also be used to determine the stability of an individual cavitation nucleus. Bubble stability is an essential factor regarding cavitation inception. As presented in Brennen (1995), for example, in a case of a small perturbation in bubble size from $R = R_e$ to $R = R_e(1+\varepsilon)$, where ε is a small constant $\varepsilon \ll 1$, the bubble faces two possible outcomes.

In the first outcome, the partial gas pressure remains the same in the bubble. The perturbation is generated over a long period of time and mass diffusion is allowed between the fluid and the bubble to maintain the partial gas pressure inside the bubble. This phenome-

non is not of key interest from the cavitation point of view, although it does affect the number and size of the cavitation nuclei in a fluid.

In the second case, the change in the bubble size is rapid so that the mass and temperature of the gas remain the same in the bubble. The gas term in the Rayleigh-Plesset equation then becomes $p_g = \frac{p_{g,e}}{\rho_w}\frac{R_e^{3\gamma}}{R^{3\gamma}}$. By substituting this with $R = R_e(1+\varepsilon)$ into the Rayleigh-Plesset equation one gets the following form of equation:

$$R(t)\ddot{R}(t) + \frac{3}{2}\dot{R}(t)^2 = \frac{\varepsilon}{\rho_w}\left[\frac{2S}{R_e} - 3\gamma p_{g,e}\right] \tag{22}$$

Here ε has the same sign as the term in the brackets in the case where

$$\frac{2S}{R_e} > 3\gamma p_{g,e}. \tag{23}$$

This means that the velocity and/or acceleration of the bubble radius has the same sign as the perturbation in the case that the inequality in Eq. (23) holds. The equilibrium is unstable, since the initial motion causes the bubble to grow further from $R = R_e$. In the opposite case, the equilibrium is stable.

In an equilibrium condition where the change in bubble size is fast enough for gas diffusion to be neglected, the stable equilibrium requires that

$$p_{g,e} = \frac{m_g T_B K_g}{\frac{4}{3}\pi R_e^3} > \frac{2S}{3\gamma R_e} \tag{24}$$

where T_B is the temperature in the bubble and K_g is the gas constant. The critical bubble size R_c for a given mass of the gas is now determined as

$$R_c = \sqrt{\frac{9\gamma m_g T_B K_g}{8\pi S}} \tag{25}$$

The bubbles of radius $R_e < R_c$ are stable, and the bubbles of radius $R_e > R_c$ are unstable. The critical size of the bubble can be reached by decreasing the ambient pressure in the fluid domain. The critical pressure $p_{\infty,c}$ is determined based on Eqs. (17) and (25) as follows:

$$p_{\infty,c} = p_v - \frac{4S}{3}\sqrt{\frac{8\pi S}{9\gamma m_g T_B K_g}} \tag{26}$$

This pressure is called the Blake threshold pressure. Figure 5 shows the isothermal equilibrium cases for various fixed masses in bubbles with a fixed surface tension. The maxima of the curves form the critical radii of the bubbles with different amount of gas in them. This line is depicted by the dashed line in the figure. It separates the stable and unstable

equilibriums. The equation of the dashed line is $p_v - p_\infty = \frac{4S}{3R_e}$. As the figure shows, at pressures below the critical pressure the bubble radius increases or decreases according to changes in the ambient pressure. At the critical pressure, the bubble radius increases regardless of changes in the ambient pressure.

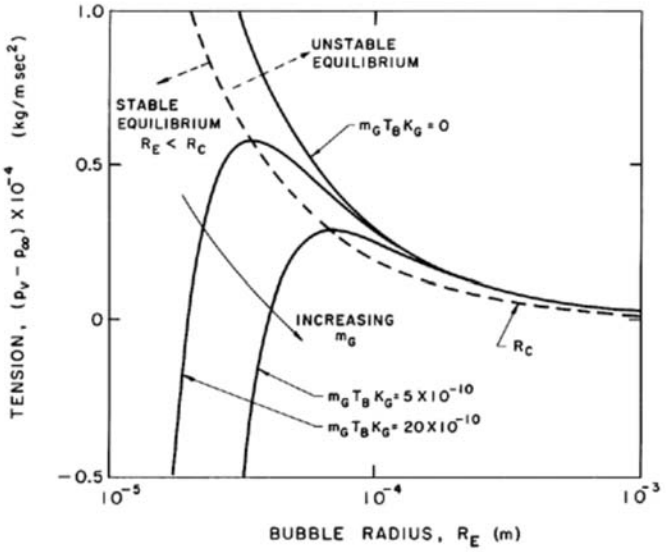

Figure 5. Radii of stable and unstable equilibriums as a function of the difference between vapour and ambient pressures for various masses of gas in a bubble. The stable and unstable equilibriums are separated by the dotted line. (Figure taken from Daily & Johnson [1956].)

In a case of turbulent flow, the bubbles are under the influence of pressure fluctuations. If the mean pressure is close to the critical pressure, the bubble radius can momentarily exceed the critical radius due to pressure oscillations. The bubble then continues to grow explosively without shrinking even if the pressure increases again above the critical pressure. For this reason, cavitation incepts earlier in turbulent flows compared to laminar flows.

1.1.4 Noise and erosion

The noise emitted from cavitation can be divided into the low- and high-frequency noise bands. The low-frequency noise is caused by the volume fluctuations of the glassy sheet and tip vortex cavitations. These volume fluctuations are mainly induced by changes in ambient pressure. The frequency of these pressure fluctuations is the blade passing frequency and its harmonics in the propeller application. The natural shedding of the sheet cavities also alters the size of the vaporized regions on the hydrofoils.

The final stage of collapse of the cavitation bubbles is violent and forms narrow and high pressure pulses in the surrounding medium. The collapses form a continuous noise spectrum that is dominant at the high-frequencies. Cavitation bubbles may form when the sheet cavity is cut off by the re-entrant jet and convected downstream with the bulk flow. The bubbles may also tear off at the trailing edge of the sheet cavity.

Cavitation bubbles play important role in noise emitted from vortex cavitation. Even though vortex cavitation seems to be glassy, there are bubbles at the outer edges of the cavitating vortex core causing high-frequency noise.

Matusiak (1992) models the high frequency noise emitted by a group of collapsing cavitation bubbles. In the Matusiak model, the cavity is disintegrated into a group of cavities using a model for the collapse of individual cavities, and the bubbles tear off from the trailing edge of the sheet cavity. The bubble sizes are statistically determined in the model. The volume rate of the forming bubbles is identical to the reduction in sheet cavitation volume. Hallander (2002) includes the interaction of the cavitation bubbles in his high-frequency noise model.

Cavitation erosion is related to the collapse of cavitation bubbles near a material surface. Van Terwisga et al. (2009) conducted a review of the physical mechanisms and models related to cavitation erosion, and it is this review that is mainly referred to below. Hammit (1963) postulated that cavitation erosion incepts when the potential energy of the shed cavity exceeds the damage threshold of a skin. The damage threshold is determined by the properties of the material exposed to cavitation collapse. The potential energy of the cavity turns into an accumulating kinetic energy which converts into acoustic energy at the final point of the bubble collapse. The shock waves then radiate into the material surface causing erosion. Figure 6 shows an example of propeller blade erosion caused by cavitation.

Figure 6. Cavitation erosion damage caused by root cavitation and cavitation cloud collapse near the trailing edge of a propeller blade.

The cavitation damage is proportional to the energy emitted by cavitation to the material. The cloud cavities that occur due to the break-up of the sheet cavitation are actually a mixture of cavitating vortices (Foeth, 2008). The vortices are of the ring-vortex type. As they convect close to a solid surface they turn into horseshoe vortices (Kawanami et al., 2002). The bubbles in the horseshoe vortices are concentrated to the material surface through the vorticity that is directed towards the surface. This leads to a concentration of the pressure pulses emitted from the collapsing cavitation bubbles near to the material surface and, potentially, erosion. Since the shedding of sheet cavitation is usually regular in time and space the erosion damage on a material surface can become serious over a long period of time.

Another source of cavitation erosion is related to tip vortex cavitation. In a case where the cavitating tip vortex breaks up close to a material surface, the vortex diverges into cloud and ring vortex cavitations. Near a material surface the ring vortices deform into horseshoe vortices and cavitation erosion may form in the same way as in the shedding of sheet cavitation. The tip vortices usually hit the material surface in a certain limited area. The cavitation erosion is thus focused on a relative small region over a long period of time, which makes cavitation erosion related to tip vortices potentially severe. It is generally assumed that stable tip vortex cavitation does not cause cavitation erosion, since there is no local concentration of potential energy of the cavity due to the absence of horse shoe vortices.

To mention some erosion risk models, those presented by Bark et al. (2004) and Fortes-Patella et al. (2004) are based on the transfer of energy from collapsing vapour clouds into acoustic energy emitted from the collapsing micro bubbles. Bark et al. (2004) identifies bubble rebound as an indicator of aggressive cavitation that may lead to erosion. The method introduced by Fortes-Patella et al. (2004) determines the damage rate based on the flow aggressiveness potential and the pressure wave power induced from macroscopic vapour cloud collapses. The most critical parameters in this model are the distance from the centre of the vapour cloud collapse to the material surface, and the hydrodynamic characteristics such as the reference velocity and cavitation number. The cavitation cloud extent, calculated from CFD calculations, can also be used as an input in the cavitation erosion models discussed above.

The cavitation erosion model of Kato et al. (1996) takes into account the cavity generation rate and the number and size of the bubbles in the cavity cloud. Only the bubble collapses that occur inside a specific effective layer are taken into account. The spatial distribution of the bubbles and the initial gas pressure inside the bubbles are disregarded. This model does not take into account that the bubbles gather in horseshoe vortices near the material surface.

1.2 Cavitation in marine applications

Cavitation was first discovered in the marine context in connection with the famous steam ship Turbinia. The vessel's inventor, Sir Charles Parsons, performed a revolutionary surprise demonstration of the vessel at the annual fleet review of the Royal Navy at Spithead, Great Britain, on June the 26th, 1897. In front of a prestigious audience of royal and naval

dignitaries, the experimental vessel, which had reached over 30 knots in sea trials, proved itself to be by far the fastest ship of its day by easily outmanoeuvring all other ships at the review.

Parsons faced the cavitation phenomenon in developing the propulsion for the Turbinia. The vessel was first equipped with a single propeller with a 1750 rpm rate of rotation. However, with this arrangement a maximum speed of only slightly below 20 knots could be achieved. Parsons altered the propeller geometry without success until he finally deduced that the poor performance of the ship might be caused by the formation of "vacuous cavities" behind the propeller blades. He increased the blade area to decrease the loading per propeller area ratio by introducing three shafts in the Turbinia and by installing three propellers on each shaft, giving a total of nine propellers sharing the power of the steam turbines. After tuning the propeller geometry, the vessel reached a world record speed of over 34 knots (Anonym, 1981).

Cavitation has ever since remained a focus of key interest and research in the maritime field. In addition to the propulsion devices, cavitation also incepts on other submerged appendages of the ships, such as fins and keels.

Cavitation is the cause of three key detrimental phenomena acting on ships and other marine structures. Firstly, cavitation is a source of underwater noise, which is emitted into the sea environment and to the interior of the ship. Cavitation noise has a detrimental impact on marine fauna as well as on passengers and crew on board. In the naval context, cavitation noise is utilized to detect enemy ships. Secondly, cavitation also induces vibration of ship structures, which can be disruptive to people on board and, in severe cases, can inhibit the task of the ship. The third detriment is cavitation erosion. If the dry-docking interval must be shortened due to erosion damage, considerable additional costs are incurred by the ship owner.

Despite its drawbacks, cavitation can sometimes be utilized in ship propulsion. In the highly loaded propellers, where cavitation inception cannot be avoided, the cavitation behaviour of the foil is designed so that sheet cavitation extends from the leading edge of the blade over the trailing edge. This is achieved by decreasing the propeller diameter and, thus, increasing its loading. By using special section profiles on the blades, fully cavitating conditions over the blade are ensured. The lift force in these supercavitating blades is provided by the vapour pressure on the suction side and the overpressure on the pressure side of the blade. Viscous drag is lower on supercavitating propellers compared to conventional propellers, but the benefit of drag reduction is lower than the detriment of losing lift force (Matusiak, 2000). Super cavitation helps to avoid large fluctuations in the volume of the cavitation region and related large pressure pulses, vibration excitations, and possible erosion problems.

1.2.1 Cavitation types on marine propellers

Cavitation in the marine context can be divided into five categories according to the ITTC (2002). The cavitation categories are listed and briefly described below in accordance with the ITTC descriptions.

Sheet cavitation or attached cavitation is usually thin, smooth and transparent. It initiates from the leading edge of a blade or hydrofoil as the local pressure reaches the critical pressure. The liquid flow separates at the blade and a region of vapour is formed between the water and the blade. Sheet cavitation is often foamy in appearance. It is generally suspected that sheet cavitation is erosive when occurring on the pressure side of a blade. The phenomenon is common with controllable pitch propellers (CPP) when using low pitch and a high rate of revolution.

Cloud cavitation occurs in regions with a large number of complex vortical structures of vapour bubbles. It is formed from the break-up of unsteady sheet cavitation. The detached sheet cavities convect downstream with the local flow field. If the cloud cavities collapse near a material surface they can be erosive.

Bubble cavitation forms on blades having so-called "new blade sections" that do not produce a low pressure peak at the leading edge of the blade. The bubbles appear as small, rapidly growing cavitation nuclei. Small bubbles are formed at a sectional Reynolds number of about $Re_{0.7R} > 10^6$ and large bubbles at about $Re_{0.7R} < 10^6$. The sectional Reynolds number is defined as

$$Re_{0.7R} = \frac{\sqrt{V_A^2 + (0.7\pi nD)^2}\, c_{0.7}}{\nu} \tag{27}$$

where V_A is the advance speed of the propeller, n is the propeller rate of revolution, D is the propeller diameter, $c_{0.7}$ is the chord length at radius $r/R = 0.7$, where R is the propeller diameter, and ν is the kinematic viscosity of water.

Streak cavitation is a form of bubble cavitation. Bubble cavitation forms first at isolated roughness spots on the leading edge of the blade or at imperfections on the blade surface, and develops then as isolated narrow streaks, often present in parallel on the blade.

Root cavitation is a thick three-dimensional cavity that incepts at the blade root. Root cavitation is potentially erosive. It is common on CPPs.

Vortex cavitation forms at the low-pressure core of vortices. The ITTC (2002) divides vortex cavitation into the following detailed categories:

- **Trailing tip vortex** cavitation incepts downstream from the blade tip.
- **Leading edge vortex** cavitation incepts along the leading edge due to high loading conditions at the leading edge.
- **Attached tip vortex** cavitation incepts very close to the blade tip and is often attached to the blade.
- **Propeller-Hull vortex** (PHV) forms at high loading conditions at low vessel speeds. The collapse of a cavitating PHV can excite severe vibrations in the ship hull.
- **Hub vortex** cavitation is developed at the trailing edge of a propeller hub. It can excite vibration and erosion of the rudder.
- **Ducted propeller tip gap leakage vortex** cavitation is present at the gap between the blade and the duct inner face. Cavitation can induce vibration and erosion of the duct. In severe cases, a hole can be eroded though the inner surface of the duct.

CPP blade bolt cavitation incepts on the blade bolts and in their holes in CPP applications.

Shear cavitation incepts in regions of high shear vorticity. The pressure drops below vapour pressure in rotational structures. Shear cavitation can be found in the separated flow regions that develop on blades with a high angle of attack and in the wakes of hydrofoils.

Figure 7 shows photographs of the different cavitation types on propeller models in cavitation tunnels. The top left photograph shows a few large cavitation bubbles convecting downstream on the propeller surface. The streak cavitation incepting at the leading edge of the blade forms sheet cavitation that is foamy at the rear part of the cavity. A strong root cavity is also present.

The top right photograph in Figure 7 shows streak cavitation forming at some distance from the blade leading edge and merging into sheet cavitation. The blade section is more heavily loaded at the mid-chord since the leading edge is free of cavitation. The sheet cavity spreads as bubble cavitation into the propeller wake field. The propeller tip is free of cavitation, which indicates that the tip of the blade is unloaded.

The photograph at the bottom left of Figure 7 shows glassy sheet cavitation at the mid radii of the blade leading edge. A leading edge vortex develops along the highly skewed leading edge and develops finally to a leading edge – tip vortex slightly below the blade tip. Close examination of the blade tip reveals that an attached tip vortex is also present. The attached tip vortex cavity extends to the propeller slipstream. Root cavitation is also present on the blade. The photograph at the bottom right shows a cavitating detached tip vortex and root cavitation.

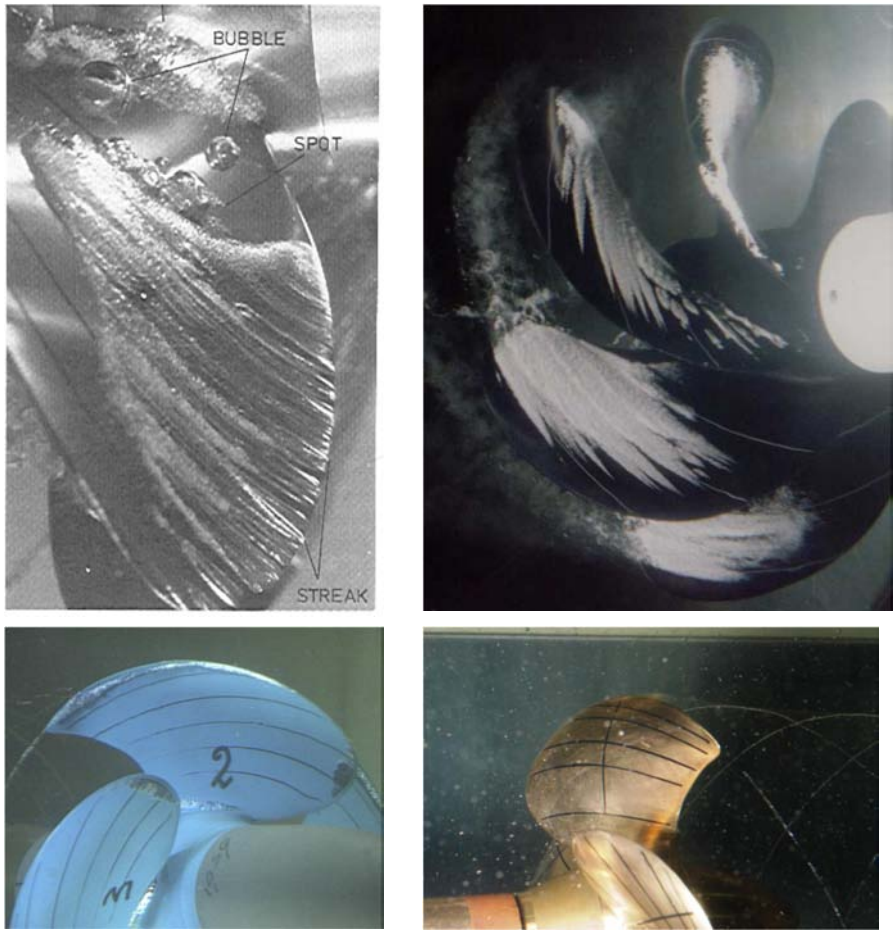

Figure 7. Top left: leading edge streak cavitation forming as sheet cavitation, large bubble cavitation, and root cavitation. Top right: streak cavitation and small bubble cavitation. Bottom left: leading edge sheet cavitation, leading edge vortex cavitation, leading edge – tip vortex cavitation, attached tip vortex cavitation, and root cavitation. Bottom right: detached tip vortex cavitation and root cavitation. (Photographs at the top and bottom left taken from the ITTC [2002]; photograph at bottom right taken from Heinke [2011].)

1.2.2 Dynamics of sheet cavitation

Arakeri (1975) used spheres, cylinders, and ogival bodies in his investigations of the inception of attached sheet cavitation. Arakeri found that the attached sheet cavity incepts after a small laminar separation bubble. The flow is laminar from the stagnation point to the laminar separation point. In the transcritical region the laminar flow mutates into turbulent flow just after the separation point. The turbulent flow reattaches to the body and a

small laminar separation bubble is formed between the separation and reattachment points. Sheet cavitation is known to incept at the trailing edge of the laminar separation bubble.

Water is at a metastable state between the low pressure peak and the laminar separation point. The laminar separation bubble detaches the streamlines from the body surface, enabling the cavity to remain attached to the surface. The attached sheet cavity would be washed away with the main flow if no laminar separation bubble was located in front of the cavity.

Frank and Michel (1985) made similar observations as Arakeri (1975) regarding sheet cavities on hydrofoils. Frank and Michel (1985) found that the inception of sheet cavitation follows the location of the transition region from laminar to turbulent flow on the hydrofoils. A sketch of a laminar separation bubble on a hydrofoil is shown in Figure 8. The location of the laminar separation point is independent of the Reynolds number.

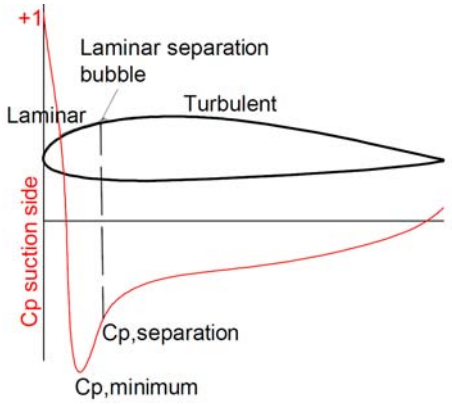

Figure 8. Pressure distribution on the suction side of a hydrofoil and laminar separation bubble dividing the flow regime into laminar and turbulent regions.

A laminar separation bubble in front of the sheet cavity is shown in Figure 9. The sheet cavity is very thin at its leading edge. The surface tension between the water and vapour forms a radius of curvature on the leading edge of the sheet cavity, as shown in Figure 9. The radius of curvature depends on the surface tension of water and vapour, and the location of the cavity leading edge. The passing streamlines on top of the separation bubble induce circulation inside the laminar separation bubble.

To form an attached sheet cavity, the cavitation nuclei must not activate between the low pressure peak and the laminar separation bubble. This requires the water to be deaerated. This is the case, for example, in cavitation tunnels if no nuclei seeding is performed. The nuclei are trapped by the laminar separation bubble. The nuclei grow slowly by diffusion of dissolved air in the laminar separation bubble (Franc & Michel, 2004). The cavitation bubbles then merge behind the laminar separation bubble and form an attached sheet cavity.

At higher Reynolds numbers and low angles of attack, the boundary layer turns from laminar to turbulent upstream of the possible laminar separation point. The flow remains

attached to the foil or separates at the turbulent separation point, which is located significantly downstream of the laminar separation point. In that case, cavitation appears as separate transient bubbles or as three-dimensional vapour structures attached to isolated roughness elements.

Kuiper (2011) explains that travelling cavitation bubbles can also induce attached cavitation. The cavitation bubbles start growing in the transition region. Depending on the pressure gradient, the cavitation bubbles can move with the flow or they can expand in the upstream and downstream directions and form an attached sheet cavity. The formed sheet cavity induces a laminar separation bubble in front of itself, which prevents the wetted flow from flushing away the cavity.

With ship propellers, the low pressure peak on the suction side of the blade is located close to the leading edge. The transition zone is very short due to the strong adverse pressure gradient close to the leading edge. Consequently, the cavitation inception can be assumed to take place very close to the low pressure peak at the blade leading edge. At the model scale, laminar separation can be considerable and modify the observed cavitation extension drastically.

The dynamics of sheet cavitation are determined by the re-entrant jet that penetrates inside the cavity along the foil surface from the trailing edge of the cavity. The pressure inside the cavity is the vapour pressure. Since the pressure in the liquid domain is higher than that inside the cavity, the streamlines tend to bend towards the cavity.

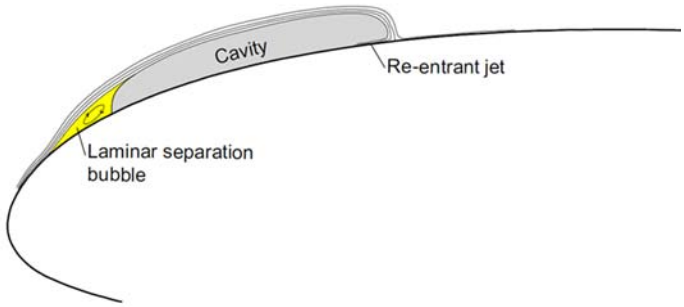

Figure 9. A two dimensional sheet cavity near the leading edge of a hydrofoil. The laminar separation bubble is also shown.

Figure 9 shows a sketch of a two-dimensional sheet cavity forming close to the leading edge of a hydrofoil. A dividing streamline travels over the vaporous region and forms a stagnation point behind the cavity. The streamlines travelling between the dividing streamline and the cavity bend upstream along the foil surface under the cavity and form a re-entrant jet. The thin layer of liquid travels upstream until it bends up and breaks off a part of the sheet cavity. In an extreme case, the re-entrant jet travels upstream to the leading edge of the cavity and detaches the entire sheet from the foil.

Le et al. (1993) and De Lange and de Bruin (1998), among others, have experimentally investigated the shedding mechanism of thick sheet cavitation on a two-dimensional hydrofoil. A schematic view of their observations is given in Figure 10. At the first stage, the

cavity starts to grow following the break-off of the sheet. After the cavity has extended to its ultimate length, a strong re-entrant jet develops at the closure of the cavity. The re-entrant jet penetrates the sheet cavitation some distance upstream from the cavity closure.

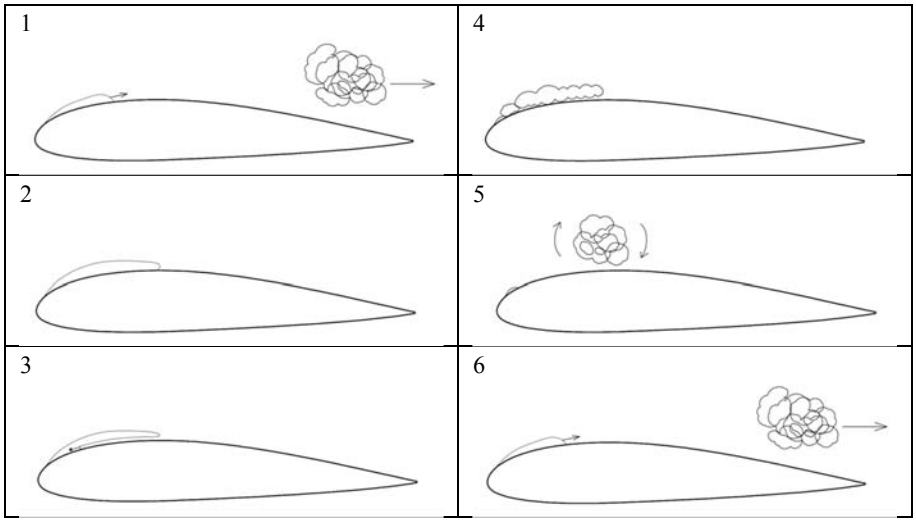

Figure 10. The shedding mechanism of sheet cavitation. The flow is from left to right. (Figure reproduced from De Lange & de Bruin [1998].)

Based on the potential flow theory, the velocity of the re-entrant jet is equal to the flow velocity on top of the cavity, i.e. $U_\infty\sqrt{1+\sigma_v}$, where U_∞ is the inflow velocity and the cavitation number σ_v is defined as:

$$\sigma_v = \frac{p_\infty - p_v}{\frac{1}{2}\rho U_\infty^2} \tag{28}$$

In practice, the velocity of the re-entrant jet is slightly smaller than that of the free-stream velocity (Kawanami et al. [1998] and Franc & Michel [2004]).

As the re-entrant jet breaks off from the sheet cavity, a cloudy cavity formed of bubbles develops from the rear part of the sheet. The momentum of the re-entrant jet causes the cloudy cavity to circulate in a direction opposite to the main flow. The cloud then advects downstream with the main flow to a high-pressure region where it collapses violently causing noise and, possibly, erosion. The shedding cycle starts after the re-entrant jet severs part of the sheet cavity. It is to be noted here that the shedding of the sheet cavitation occurs also in uniform inflow conditions.

If the sheet cavity is thick, the natural oscillations are periodic with relatively constant shedding frequency. In cases where the sheet cavity is thin, i.e. at low angles of attack, the re-entrant jet does not have enough momentum to penetrate far upstream from the closure of the cavity. The chordwise location of the break-off varies between shedding cycles due

to wavy disturbances in the re-entrant jet and the sheet cavity. The cloudy structures are, naturally, smaller in the case of thinner sheet cavities. At smaller Reynolds numbers, the viscous forces are higher and the momentum of the re-entrant jet is decreased.

Regular shedding of the sheet cavity is represented by the non-dimensional Strouhal number, *St*, defined as:

$$St = \frac{fl}{U_\infty} \tag{29}$$

where *f* is the frequency of shedding, *l* is the maximum length of the sheet cavity, and U_∞ is the main inflow velocity. The Strouhal number is constant at varying inflow speeds within reasonable limits. The Strouhal number for natural shedding of sheet cavities is *St* = 0.25 … 0.35. One of the reasons for the large deviation in the observed Strouhal numbers is the difficulty in determining the maximum length of the cavity.

The effect of the three-dimensionality of the re-entrant jet is discussed in a number of papers, for example Duttweiler and Brennen (1998), De Lange and de Bruin (1998), Laberteaux and Ceccio (2001a and 2001b), Foeth and van Terwisga (2006), and Huuva (2008). De Lange and de Bruin (1998) predicted that the re-entrant jet simply reflects from the cavity closure line. This prediction was based on the assumption that the pressure gradient at the cavity closure line is zero. As a consequence, the tangential component of the velocity along the closure line remains the same. The reflection of the re-entrant jet at the normal and inclined cavity closure lines is shown in Figure 11. Dular et al. (2007) verified the assumption of the reflection of the re-entrant jet both experimentally and numerically.

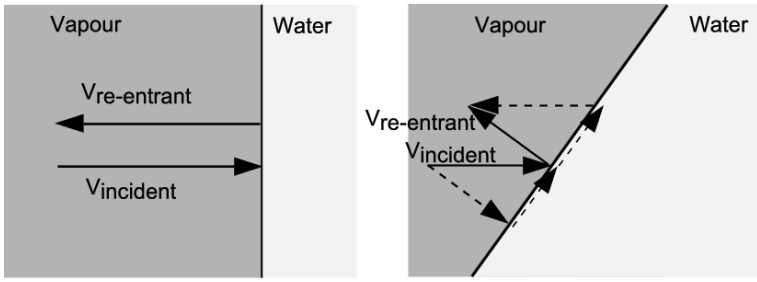

Figure 11. Behaviour of the re-entrant jet at the cavity closure line at the normal incidence (left) and oblique (right) incidence angles. (Figure reproduced from de Lange & de Bruin [1998].)

The cavity closure line on the ship propellers is practically always inclined due to the skewed leading edge and the varying pitch of the blade. Also, the non-uniform inflow to the propeller affects the incidence angle of the re-entrant jet. As a consequence, the re-entrant jets are not parallel on the propeller blades and they collide under the sheet cavity. At the collision point, the re-entrant jets are directed upwards and an additional complex shedding phenomenon, called secondary shedding, is introduced into the main shedding

cycle. The shedding of the cavity sheet has been investigated intensively in recent years. References of note for further reading include the doctoral theses of Aït-Bouziad (2006), Foeth (2008), Huuva (2008), and Koop (2008), which focus on the numerical and experimental investigation of sheet cavity shedding mechanisms.

1.2.3 Dynamics of tip vortex cavitation

Tip vortices are developed in the slipstream of lifting surfaces. In the ship context, typical lifting surfaces are propellers, rudders, fins, and skegs. Tip vortices develop due to the pressure difference between the pressure and suction sides of the lifting surfaces. At the tips of the lifting surfaces the pressure difference forces the flow to rotate from the pressure side to the suction side of the foil, thus forming the tip vortices.

The generation of tip vortices can be explained according to the potential flow theory in the following manner. Kelvin's theorem states that the circulation Γ around any closed material curve is constant in time, i.e.:

$$\Gamma = \oint_{\gamma(t)} \vec{v} \cdot d\vec{l} \tag{30}$$

where $\gamma(t)$ is the vorticity, and $\mathrm{d}\vec{l}$ is a length element in a curvilinear path $\vec{l}$. According to the Stokes theorem, the circulation can also be expressed as the spread vorticity $\vec{\zeta}$ on a material surface S:

$$\Gamma = \iint_S \vec{\zeta} \cdot \vec{n} dS \tag{31}$$

where $\vec{n}$ is a unit normal vector. The vorticity is defined as

$$\vec{\zeta} = \nabla \times \vec{v} \tag{32}$$

Since the circulation is constant also the vorticity flux must be constant.

The Helmholtz theorem states that a vortex line is a material line. The same holds also for a vortex sheet, which is a surface comprising all vortex lines passing through a closed curve $\gamma(t)$. Regarding the conservation of mass and the circulation in an element of length δl and area δS, it holds that in a vortex sheet $\rho\, \delta l\, \delta S = \text{constant}$ and $\vec{\zeta}\, \delta S = \text{constant}$. Thus the ratio $\frac{\vec{\zeta}}{\delta l}$ remains constant. If the vortex sheet is stretched, the cross-section is decreased and the vorticity increases in this section.

Vorticity can be divided into bound and free vorticity. Bound vorticity carries the load on the hydrofoil. Free vorticity does not carry load but is responsible for the induced drag of the flow field.

A three-dimensional flow around an elliptical hydrofoil has its maximum circulation Γ_{max} at the mid-span. The circulation decreases gradually towards the tips of the foil where

the circulation is zero, see for example Sánchez-Caja (2010). The circulation on a high-aspect ratio wing can be presented using the horseshoe vortices of semi-infinite length as shown in Figure 12. The free vortices of the hydrofoil roll up forming two tip vortices in the slipstream of the foil. The roll-up process is driven by the self-induced velocities of the free vortices in the slip stream. The circulation in the tip vortices is progressively increased in the slip stream as the roll-up process develops. Far downstream from the hydrofoil the circulation in the tip vortices reaches its maximum $\Gamma=\Gamma_{max}$.

The tangential velocity inside a two-dimensional vortex is calculated by the formula:

$$\vec{\zeta} v_\theta(r) = \frac{\Gamma}{2\pi r}. \tag{33}$$

However, this formula gives unrealistically high velocities close to the core of the vortex and a singularity at the origin of the vortex. In real flows, viscosity has a major role in the dynamics near the origin of the vortex. The vortex can be divided into two zones. In the inner zone the vorticity is approximately uniform and the viscous forces are dominant. In the outer zone the vorticity is small and the fluid can be considered inviscid.

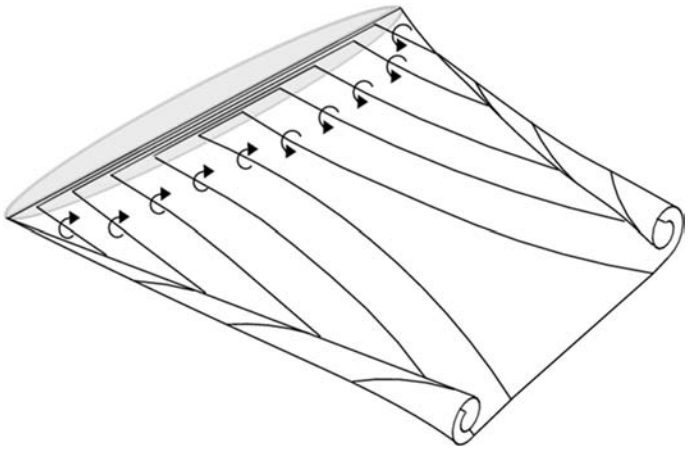

Figure 12. A schematic view of the wake roll-up into the tip vortices of an elliptical planform. The direction of free vorticity of the horseshoe vortices is also shown.

The Rankine vortex model (Rankine, 1869) treats the viscous inner core as a solid body. The tangential velocity inside the viscous core is determined as

$$v_\theta(r) = \frac{\Gamma}{2\pi a^2} r. \tag{34}$$

where a is the radius of the viscous core of the vortex. At the radii outside the viscous core the velocities are calculated with Eq. (33). The tangential velocity has its maximum in the core at the radius $r = a$.

Another model for predicting the behaviour of a turbulent vortex was presented by Burgers (Burgers, 1948). This model takes into account the diffusion of the vorticity in the fluid and also the stretching of the vortex, i.e. the axial velocity in the vortex depends on the axial position in it. The steady equations of the Burgers model for the axial, tangential, and radial velocity components are given as follows (e.g., Wu et al., 2006):

$$v_x(x) = \gamma x,. \tag{35}$$

$$v_\theta(r) = \frac{\Gamma}{2\pi r}\left(1 - e^{-\beta\left(\frac{r}{a}\right)^2}\right) \tag{36}$$

$$v_r(r) = -\frac{\gamma}{2} r \tag{37}$$

where $\beta = \frac{\gamma}{4\nu}$. The stretching γ can be a constant or a variable.

The Oseen-Lamb vortex model (Oseen, 1912 and Lamb, 1932) does not take into account the vortex stretching. The dissipation of the vorticity is, however, involved in this model. The tangential velocity component is calculated as (e.g. Wu et al., 2006):

$$v_\theta(r) = \frac{\Gamma}{2\pi r}\left(1 - e^{-\left(\frac{r}{a}\right)^2}\right) \tag{38}$$

where the viscous core radius a is calculated by the formula:

$$a = \sqrt{4\nu t} \tag{39}$$

The Oseen-Lamb vortex has the same solution as the Burgers vortex if the time is frozen at $t = 1/\gamma$. At that moment the radial flow brings the far-field vorticity to the vortex core at a rate that compensates the diffusion of the vorticity at the core of the Burgers vortex.

By choosing the factor $\beta = 1.256$ in the Burgers vortex model the velocity maximum is located at the same position as in the Rankine vortex. The differences in the velocity distributions between the Rankine and Burgers models are compared in Figure 13. The velocity distribution of a potential vortex is also given for comparison in the figure.

As the figure shows, the maximum velocity distribution induced by the Burgers vortex is about 0.715 times that induced by the Rankine vortex. The velocity distribution in the Burgers vortex is close to that in the Rankine vortex near the rotational core and at radii

$r/a > 2.0$. The velocity distributions of the Rankine and Burgers vortices are close to the potential vortex solution at radii $r/a > 2.0$. The velocity distribution of the Rankine vortex has a singularity point at the outer side of the rotational core.

The Rankine vortex must fulfil the Bernoulli's equation at the outer irrotational core:

$$p + \frac{1}{2}\rho v_\theta^2 = p + \frac{1}{2}\rho\left(\frac{\Gamma}{2\pi r}\right)^2 = const. \tag{40}$$

By taking the conditions far from the vortex core as reference the following formula is derived:

$$p_\infty + \frac{1}{2}\rho\left(\frac{\Gamma}{2\pi r}\right)^2_{r\to\infty} = p + \frac{1}{2}\rho\left(\frac{\Gamma}{2\pi r}\right)^2 \tag{41}$$

and further

$$p - p_\infty = -\frac{\rho}{2}\frac{\Gamma^2}{4\pi^2 r^2} \tag{42}$$

It is seen that the pressure is an inverse of the distance from the core squared.

The Euler equations give in the rotational core at a steady state:

$$\frac{1}{\rho}\frac{\partial p}{\partial r} = \frac{v_\theta^2}{r} \tag{43}$$

The velocity equation in the inner zone of the Rankine vortex is now substituted in the above equation:

$$\frac{\partial p}{\partial r} = \rho\frac{\left(\frac{\Gamma}{2\pi a^2}r\right)^2}{r} = \frac{\rho r\Gamma^2}{4\pi^2 a^4} \tag{44}$$

Integrating this with respect to r yields:

$$p = \frac{\rho}{2}\frac{\Gamma^2}{4\pi^2 a^4}\left(\frac{r}{a}\right)^2 + C \tag{45}$$

where C is an integral constant. The pressure rises in the rotational core by the square of the radius. The integral constant C is determined based on the fact that the pressure must be continuous at the outer radius of the rotational core $r = a$, as follows:

$$C = p_\infty - \frac{\rho\Gamma^2}{4\pi^2 a^2} \tag{46}$$

The complete equation for the pressure inside the rotational core is then:

$$p - p_\infty = \frac{\rho}{2}\left(\frac{\Gamma}{2\pi a}\right)^2 \left[\left(\frac{r}{a}\right)^2 - 2\right]. \tag{47}$$

The determination of the pressure distribution inside a two-dimensional Burgers vortex follows the same principles as those utilized for the Rankine vortex. The tangential velocity distribution inside the vortex is substituted in Eq. (43). The integral constant is determined by using the far-field pressure p_∞ as the reference pressure. The final equation for the pressure distribution inside the Burgers vortex is therefore:

$$p - p_\infty = -\rho\left(\frac{\Gamma}{2\pi}\right)^2 \int_x^\infty \frac{\left(1 - e^{-\beta\left(\frac{r}{a}\right)^2}\right)^2}{\left(\frac{r}{a}\right)^3} \mathrm{d}r \tag{48}$$

The equation above can be solved numerically. Rott (1958) conducted a detailed analysis of the pressure equation of the Burgers vortex. The solutions for pressure distribution in the Rankine and Burgers vortices are shown in Figure 14. The pressure distribution in a potential vortex is also shown for comparison in the figure.

As the figure shows, the minimum pressure in the Burgers vortex is about 0.8706 times that of the Rankine vortex. The pressure in the potential vortex drops to the negative infinity at the origin. The pressure distribution in the Burgers vortex meets the potential vortex at an approximate radius of $r/R = 2.0$. This is the same radius at which the induced velocity profile of the Burgers model meets the velocity profile induced by the potential vortex. The pressure distribution of the Rankine vortex differs from the potential vortex solution at the rotational core of the vortex.

The Burgers vortex model assumes that the vortex is rotationally symmetric. This assumption is, however, not wholly correct in the case of propeller tip vortices, especially close to the blade tip. Nevertheless, the Burgers model agrees closely with the experiments. Fruman et al. (1992) compared the measured tangential velocity distribution of a tip vortex to the Burgers model. They calculated the vortex strength based on the angular momentum outside the rotational core of the vortex and compared the measured and calculated velocity distributions inside the vortex. The agreement was found to be good.

Fruman et al. (1992) also observed that the rotational core of the vortex is at its smallest at about 10% of the chord length downstream from the tip of the hydrofoil. This indicates that the pressure inside the tip vortex is at its minimum in this region. The cavitation tests show that the cavitation of the tip vortex incepts some distance downstream from the blade.

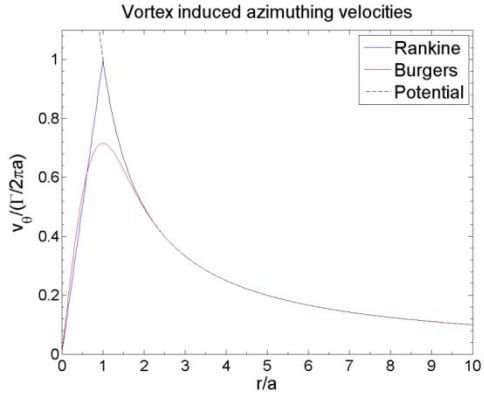

Figure 13. The azimuthing velocities induced by the Rankine, Burgers, and potential vortices.

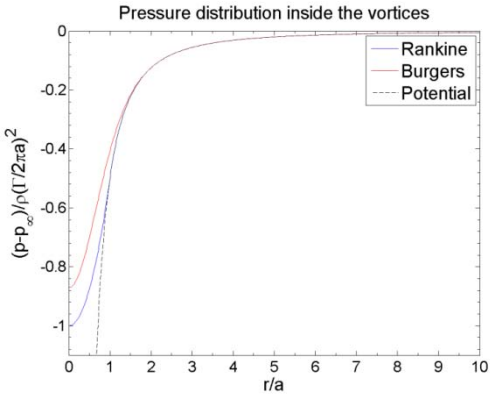

Figure 14. The non-dimensional pressure distributions in the Rankine, Burgers, and potential vortices.

McCormick (1962) studied the disagreement in the size of the viscous tip vortex core predicted by the potential flow theories and the observations made in cavitation tests. The size of the vortex core in the observations was calculated from the minimum pressure inside the vortex core, see Eqs. (47) and (48). The minimum pressure was determined from the cavitation inception in the tip vortex.

McCormick made the assumption that the rotational boundary layer on the pressure side of the foil convects into the tip vortex and thus enlarges the size of the rotational core. Since the boundary layer on the hydrofoil is dependent on the Reynolds number, McCormick found the following scaling law between the Reynolds number and the cavitation inception point σ_{vi}:

$$\sigma_{vi} = KC_L^2 Re^{\xi} \tag{49}$$

where K and ξ are constants and C_L is the lift coefficient calculated as:

$$C_L = \frac{2\Gamma_{max}}{U_\infty c_{max}} \tag{50}$$

where c_{max} is the maximum chord.

Based on the experiments McCormick determined the value $\xi = 0.35$ for the constant in the power of the Reynolds number. Later on, slightly different scaling factors have also been suggested. Fruman et al. (1992) proposed the value $\xi = 0.40$. The coefficient K is dependent on the cross-section of the foil. It should be noted that the scaling law in Eq. (49) holds only for small and moderate values of the lift coefficient.

As stressed by Franc and Michel. (2004), cavitation affects the dynamics of the tip vortex significantly. The diameter of the vortex core during cavitation inception is typically one millimetre. Due to the conservation of mass, it holds that the ratio between the diameters of the wetted and cavitating vortex cores must be:

$$\frac{d_w}{d_v} = \sqrt{\frac{\rho_v}{\rho_w}} \tag{51}$$

The water particles that lie at the outer border of the incepting cavitating vortex core, that is at a radius of 0.5 mm, were at a radius of about 4 μm from the vortex core before the inception. Since the phase transition occurs within a very short period of time, in the order of tens or hundreds of micro seconds, the radial velocity of the water particles in the vortex core is significant (Franc & Michel, 2004).

Cavitation also affects the pressure distribution in the tip vortices, since the pressure cannot fall below the vapour pressure. In addition, cavitation also has an influence on vorticity stretching in the tip vortices. The rotational rate of a wetted vortex increases when it is stretched. This is contrary to cavitating vortices. The angular momentum in cavitating vortices remains the same as in pure liquid vortices, but the inertia is changed.

Cavitating tip vortices are subject to changes in length and ambient pressure. If the ambient pressure is kept constant, vortex stretching increases the rotational velocity of the vortex, thus increasing the size of the vaporous core of the vortex. If the vortex length is constant and the ambient pressure varies, a twofold phenomenon develops. An increase in ambient pressure decreases the size of the vortex. This consequently increases the rate of rotation which, in turn, increases the size of the cavitating core of the vortex. The latter secondary effect raises the natural oscillations of the isolated vortices (Franc & Michel, 2004).

Cavitation affects the behaviour of the vortices significantly through the multiple phenomena discussed above. Consequently, cavitating vortices cannot be used as a visual indicator of the behaviour of fully wetted vortices. At best, the very first cavitation events

can be used as a qualitative indication of the rotational structures present in the vortices in wetted conditions.

If the sheet cavity attaches to the tip vortex, practically all vapour can escape from the hydrofoil blade through the cavitating tip vortex. This is true especially when the leading edge of the blade or a foil is skewed so that the re-entrant jet reflects towards the tip of the blade or the foil. In these cases, sheet cavitation may be predominantly steady. Photographs of sheet cavitation attached to tip vortex cavitation on skewed propellers and hydrofoils can be seen, for example, in Pereira et al. (2004a, 2004b), Foeth (2008), and Heinke (2011).

1.3 Turbulence investigation

The fluid flows can be divided into laminar and turbulent flows. In turbulent flows the velocity fluctuates randomly around its average value. The average value can be steady or it can change slowly compared to the turbulent fluctuations. In the laminar flows the randomly fluctuating nature of the flow is absent.

The presence of laminar or turbulent flows is characterized by the Reynolds number of the flow. The Reynolds number is a ratio between the inertia and viscous forces in the flow field. If the viscous forces are large, the flow remains laminar. In the opposite case, the flow becomes turbulent. There is no exact Reynolds value that indicates whether or not the flow is turbulent. Furthermore, the transition from laminar to turbulent flow is precipitated by an adverse pressure gradient or by wall roughness, for example.

Turbulence has a major effect on flows. Compared to laminar flows, turbulent flows have significantly higher capability to transport and mix different fluids and reactants. This plays an important role in combustion devices, for example.

Turbulence also effectively mixes the momentum of fluids. As a result, the wall shear stress increases in the turbulent flows, which also increases viscous drag. On the other hand, turbulent flows do not separate readily from a body, thus decreasing the pressure drag.

As mentioned earlier, the inception of sheet cavitation on propeller blades requires a turbulent flow field due to the favourable effect of pressure fluctuation on cavitation inception. Another hypothesis is that the cavitation nuclei are advected by turbulence closer to the blade surface into the boundary layer where the flow velocities are lower (Kuiper, 2011). There, the nuclei have more time to grow above the critical size threshold and form a sheet cavity.

In the naval context, practically all flows are turbulent at the full scale. However, at the model scale, the flow can remain laminar over a significant proportion of the model-sized hull or propeller. For this reason, turbulence stimulators are used at the bow of the model in hull model tests, and propeller model tests are performed using as high a rate of revolution as possible to increase the Reynolds number and to decrease the laminar flow region on the propeller. Empirical corrections are still needed to adjust the model test results to the full scale.

1.3.1 Trubulence scales

The well-known Navier-Stokes (N-S) equations for an incompressible Newtonian fluid are as follows:

$$\nabla \cdot \vec{v} = 0 \tag{52}$$

and

$$\rho \frac{\mathrm{D}\vec{v}}{\mathrm{D}t} = -\nabla p + \nabla \cdot \tau_{ij} + \rho \vec{g} \tag{53}$$

where $\vec{g}$ represents a body force. The shear stress tensor τ_{ij} is defined as:

$$\tau_{ij} = \mu \left(\frac{\partial u_i}{\partial x_j} + \frac{\partial u_j}{\partial x_i} \right) - \frac{2}{3} \mu \frac{\partial u_l}{\partial x_l} \delta_{ij} \tag{54}$$

where δ_{ij} is the Kronecker delta. Eq. (52) represents the continuity equation and Eq. (53) the momentum equation.

In turbulent flows the velocity fluctuates randomly around its average value. The velocity can be split into average and fluctuating components $\bar{u}$ and u', respectively:

$$u_i(t) = \bar{u}_i + u_i'(t) \tag{55}$$

The fluctuating nature of the turbulent flows is caused by the eddies that have multiple scales in a flow field. The length scale of the turbulent eddies can be divided into an energy-containing range and a universal equilibrium range (Pope, 2000). Furthermore, the universal equilibrium range is split into an inertial subrange and a dissipation range. The largest visible turbulent eddies with a length scale of h_0 belong to the energy-containing range.

In the energy-containing range the bulk of the energy is contained in the large eddies. The energy-containing range covers eddies within a length scale, h, of between $h_{EI} = 1/6h_0 < h < 6h_0$, where h_{EI} is the dividing scale between the energy-containing range and the inertial subrange. The turbulent flow motions in the energy-containing range are strongly influenced by the geometry of the flow. In the energy-containing range eddies control processes such as transport and mixing (Pope, 2000).

According to Kolmogorov's hypothesis of local isotropy, eddies with a length scale $h > h_{EI}$ are anisotropic, whereas eddies with a length scale $h < h_{EI}$ are isotropic (Pope, 2000). The production of turbulence occurs in the energy-containing range. The energy-containing range is also called the integral scale of turbulence.

The energy in turbulent eddies is transferred to successively smaller eddies in the inertial subrange, which is also called the (intermediate) Taylor scale. The energy spectrum in the inertial subrange is:

$$E(\kappa) = C\varepsilon^{2/3}\kappa^{-5/3} \tag{56}$$

where C=1.5 is a universal constant, ε is the dissipation rate of the turbulence, and $\kappa=2\pi/h$ is the wave number of the eddies. The equation above is generally known as the Kolmogorov spectrum. It states that the energy content of eddies in the inertial subrange decreases with decreasing eddy size. The inertial subrange is located between the dissipation range and the energy-containing range at the length scales $h_{DI} < h < h_{EI}$, where h_{DI} depicts the upper limit of the dissipation range.

The turbulent eddies are transformed into smaller eddies by inviscid processes until they reach the size at which viscous effects become important. The dissipation range covers this part of the eddy length scales. The eddy length scale in the dissipation range is below the limit $h < 60\eta$, where η is the Kolmogorov length scale:

$$\eta = (\nu^3/\varepsilon)^{1/4} \tag{57}$$

The motions in the dissipation range are responsible for all essential dissipation in a flow field.

1.3.2 Direct numerical simulation

In direct numerical simulation (DNS) all turbulence scales, from the energy-containing range down to the Kolmogorov scales, are simulated. In order to also resolve the smallest eddies, the grid must be extremely dense and the time-step extremely small. These requirements make the calculation extremely expensive and time consuming, even at moderate Reynolds numbers, and limit the practical use of DNS in engineering. On the other hand, the results of DNS are extremely accurate and DNS is an excellent tool for turbulence research at relatively low Reynolds numbers. The results of DNS also provide valuable validation data for turbulence modelling.

1.3.3 Large eddy and detached eddy simulation

In large eddy simulation (LES), the large-scale eddies of the turbulence spectrum are simulated and the smaller eddies are modelled. This allows the use of significantly larger cell sizes and longer time steps in LES than in DNS, which makes LES calculations clearly less expensive than those performed by DNS.

The large anisotropic turbulent eddies containing most of the energy in the turbulence spectrum are simulated in LES. The smaller isotropic eddies are modelled using so-called

subgrid-scale models (SGS). This methodology improves the accuracy of the calculations. In practice, the velocities are filtered in space in LES and the filtered velocities are solved by the Navier-Stokes equation. The filtering operation can be written formally as follows (Pope, 2000):

$$\bar{\vec{v}}(\vec{x},t) = \int G(\vec{r},\vec{x})\vec{v}(\vec{x}-\vec{r},t)d\vec{r} \tag{58}$$

where G represents a filter function and $\vec{r}$ the distance from the origin of the filtering operation. The integration is taken over the whole computational domain. The filter function must satisfy the condition:

$$\int G(\vec{r},\vec{x})d\vec{r} = 1 \tag{59}$$

The filter can be homogeneous in the simplest case, i.e. it is independent of $\vec{x}$. In the practical calculations the filter must have a finite length Δ. The residual field is defined as:

$$\vec{v}'(\vec{x},t) = \vec{v}(\vec{x},t) - \bar{\vec{v}}(\vec{x},t) \tag{60}$$

so that the velocity can be decomposed to:

$$\vec{v}(\vec{x},t) = \bar{\vec{v}}(\vec{x},t) + \vec{v}'(\vec{x},t) \tag{61}$$

The filtered N-S equations can be written in the form (Pope, 2000):

$$\frac{\partial \bar{u}_i}{\partial x_i} = 0 \tag{62}$$

$$\rho\frac{\partial \bar{u}_i}{\partial t} + \rho\frac{\partial \bar{u}_i\bar{u}_j}{\partial x_j} = -\frac{\partial \bar{p}}{\partial x_i} + \frac{\partial}{\partial x_j}\left[\mu\left(\frac{\partial \bar{u}_i}{\partial x_j} + \frac{\partial \bar{u}_j}{\partial x_{ij}} - \frac{2}{3}\delta_{ij}\frac{\partial u_l}{\partial x_l}\right)\right] - \frac{\partial \tau_{ij}^r}{\partial x_j} + \rho g_i \tag{63}$$

where τ_{ij}^r represents the anisotropic residual-stress tensor defined as:

$$\tau_{ij}^r = \tau_{ij}^R - \frac{2}{3}k_r\delta_{ij} \tag{64}$$

with $\tau_{ij}^R = \overline{u_i u_j} - \bar{u}_i\bar{u}_j$ being the residual-stress tensor analogous to the Reynolds-stress tensor and $k_r = \frac{1}{2}\tau_{ii}^R$ representing the residual kinetic energy of turbulence. The anisotropic part of the residual-stress tensor has to be modelled in LES using a sub-grid model.

There are several ways to model τ_{ij}^r. The simplest way is to use an eddy viscosity model. Smagorinsky's model (Smagorinsky, 1963) belongs to the eddy viscosity models and is one of the most widely used models in the field of LES (Pope, 2000). The anisotropic part of the residual-stress tensor is modelled as:

$$\tau_{ij}^r = -2\nu_r \bar{S} \tag{65}$$

where ν_r is the eddy viscosity of the residual motions and $\bar{S}$ is the characteristic filtered rate of strain $\bar{S} = \left(2\bar{S}_{ij}\bar{S}_{ij}\right)^{1/2}$ with $\bar{S}_{ij}$ being the filtered rate-of-strain tensor:

$$\bar{S}_{ij} = \frac{1}{2}\left(\frac{\partial \overline{u}_i}{\partial x_j} + \frac{\partial \overline{u}_j}{\partial x_i}\right) \tag{66}$$

The residual eddy viscosity is calculated as:

$$\nu_r = h_s^2 \bar{S} = (C_S \Delta)^2 \bar{S}, \tag{67}$$

where h_s is the Smagorinsky length scale defined through the Smagorinsky coefficient C_S. For a more detailed description of the model, see for example Pope (2000).

Close to a solid wall the eddies are very small. The grid should have a very high resolution in all directions to simulate an appropriate amount of the turbulent energy spectrum in the near wall regions. This can be avoided by using some functions of the law-of-the-wall that take into account the viscous effects of solid boundaries, see for example Fureby and Grinstein (2002).

Another method to solve the problem of the wall effects is to use detached-eddy simulation (DES), which is a combination of the LES and Reynolds-averaged Navier-Stokes (RANS) equations. In the DES approach the whole turbulence spectrum is modelled near the solid surfaces. In the other parts of the domain the flow field is solved by means of LES. This enables the use of reasonable size grids with good accuracy also in the near-wall regions.

1.3.4 Reynolds-averaged Navier-Stokes simulation

In Reynolds-averaged Navier-Stokes simulations the whole turbulence spectrum is modelled. In cases where the boundary conditions are steady, a steady-state solution for the flow field can be found since the effect of turbulence is modelled as an average over time. In unsteady RANS (URANS) simulations the largest eddies in the energy-containing range of the turbulence spectrum are simulated. The rest of the turbulence spectrum is modelled.

The RANS equations can be written in the form:

$$\frac{\partial \bar{u}_i}{\partial x_i} = 0 \tag{68}$$

$$\rho \frac{\partial \bar{u}_i}{\partial t} + \rho \frac{\partial \bar{u}_i \bar{u}_j}{\partial x_j} = -\frac{\partial \bar{p}}{\partial x_i} + \frac{\partial}{\partial x_j}\left[\mu\left(\frac{\partial \bar{u}_i}{\partial x_j} + \frac{\partial \bar{u}_j}{\partial x_{ij}} - \frac{2}{3}\delta_{ij}\frac{\partial u_l}{\partial x_l}\right)\right] + \rho \frac{\partial}{\partial x_j}\left(-\overline{u_i' u_j'}\right) + \rho g_i \tag{69}$$

where the velocity and pressure terms are time-averaged. The Reynolds stress component $-\overline{u_i' u_j'}$ is modeled in the RANS approach. The Reynolds stresses can be solved by an eddy viscosity approach or by modelling the Reynolds stresses.

In the eddy viscosity approach the Reynolds stresses are calculated using the Boussinesq hypothesis:

$$-\rho\overline{u_i' u_j'} = \mu_t\left(\frac{\partial \bar{u}_i}{\partial x_j} + \frac{\partial \bar{u}_j}{\partial x_{ij}}\right) - \frac{2}{3}\delta_{ij}\left(\rho k + \mu_t \frac{\partial u_l}{\partial x_l}\right) \tag{70}$$

here the eddy viscosity is depicted by μ_t and the kinetic energy of turbulence by k. The two-equation turbulence models are most widely used in practical engineering problems. In these models, turbulence is modelled with the help of two equations; one for the kinetic energy of turbulence and one for the dissipation of turbulence. A widely used two-equation turbulence model is the k-ε model, which is also used in the simulations presented in this thesis and is described in more detail in Chapter 2.2.2. Another widely used two-equation turbulence model belongs to the k-ω models. In these models an equation for turbulence frequency $\omega = \varepsilon/k$ is applied instead of ε. It is generally known that the k-ω models produce less eddy viscosity than the k-ε models. A widely used k-ω model is the one presented by Menter (1994).

The two-equation models are isotropic, i.e. μ_t is the same in all directions. The Reynolds stress models (RSM), on the other hand, are anisotropic. They attempt to model the components of the Reynolds stresses using differential momentum equations. The Reynolds stress models are complex, but have the potential to describe the effects of turbulence more precisely than the eddy viscosity models. The Reynolds stresses can be written in the form (Hellsten, 2004):

$$\rho \frac{\partial \overline{u_i' u_j'}}{\partial t} + \rho \frac{\partial\left(\bar{u}_k \overline{u_i' u_j'}\right)}{\partial x_k} = P_{ij} - \varepsilon_{ij} + \phi_{ij} + D_{ij} \tag{71}$$

where $P_{ij}, \varepsilon_{ij}, \phi_{ij}$, and D_{ij} depict the production term, the dissipation term, the pressure-strain term, and the divergence term, respectively. The terms are calculated as follows:

$$P_{ij} = -\rho\overline{u_j' u_k'}\frac{\partial \bar{u}_i}{\partial x_k} - \rho\overline{u_i' u_k'}\frac{\partial \bar{u}_j}{\partial x_k}, \tag{72}$$

$$\varepsilon_{ij} = 2\mu \overline{\frac{\partial u_i'}{\partial x_k}\frac{\partial u_j'}{\partial x_k}} \tag{73}$$

$$\phi_{ij} = \frac{1}{\rho}\overline{p'\left(\frac{\partial u_i'}{\partial x_j} + \frac{\partial u_j'}{\partial x_i}\right)} \tag{74}$$

$$D_{ij} = \frac{\partial}{\partial x_k}\rho\left(-\overline{u_i' u_j' u_k'} - \frac{1}{\rho}\left(\delta_{ij}\overline{p' u_j'} + \delta_{jk}\overline{p' u_i'}\right) + \nu\frac{\partial \overline{u_i' u_j'}}{\partial x_k}\right) \tag{75}$$

Due to its complexity, the RSM equations are generally used as research tools and not in engineering applications.

Algebraic Reynolds stress turbulence models (ARSM) are simplified alternatives to RSMs that use simplified transport terms. The ARSM model can also be closed explicitly, giving an explicit algebraic Reynolds stress model (EARSM). In such a case, the ratio P/ε is calculated by a two-equation turbulence model and the Reynolds stress tensor is produced by means of ARSM. The ARSM and EARSM turbulence models are anisotropic. A comprehensive overview of the alternative approaches to simulate turbulence in RANS is given, for example, by Hellsten (2004).

In the RANS approach, the flow equations can be solved to the wall by using a heavy clustering of computational cells towards the viscous walls. This allows accurate modelling of the boundary layer flows also in the presence of high pressure gradients that may lead, for instance, to separation of the flow. The accuracy of the calculation is, naturally, limited by the accuracy of the turbulence model.

An alternative means of calculating the flow equations to the viscous walls is to use wall functions. These are designed to take into account the viscous effects inside the logarithmic layer of the boundary layer. The benefit of this approach is that the calculations can be performed with a significantly lower number of cells, since no heavy clustering of cells is needed in the boundary layer. The drawback is that the wall functions do not always work well in the presence of high pressure gradients.

1.4 Cavitation investigations

Cavitation tests performed in cavitation tunnels have been used for decades to investigate the phenomena related to cavitation and to validate the design of ship propellers and other turbo pumps. Recently, CFD-based methods have been introduced to model cavitation. Evaporation and condensation of water and vapour are modelled by introducing a mass transfer term into the Navier-Stokes equations. The main aspects related to the experimental and CFD-based numerical methods are discussed in this chapter. The cavitation models based on the potential-flow assumption are not included in the scope of this thesis and are only briefly discussed here.

1.4.1 Relevant results of the cavitation investigations

Vapour pressure is usually representative of the pressure inside cavities in marine applications. The gas pressure in cavitation bubbles is neglected. Thus, the cavitation number σ can be expressed as follows (ITTC, 2011):

$$\sigma_i = \frac{p_\infty - p_v}{\frac{1}{2}\rho q^2} + \frac{p_c - p_v}{\frac{1}{2}\rho q^2} = \sigma_v + \Delta\sigma \tag{76}$$

where q is the reference velocity and $\Delta\sigma$ is the difference in cavitation number due to the pressure increase in the critical pressure compared to the vapour pressure. The reference velocity can be determined in a number of ways. The ITTC (2011) lists the following alternatives for the reference velocity: U_∞, V_A, nD, ωR, and $\sqrt{V_A^2 + (\omega R)^2}$, where $\omega = 2\pi n$ is the angular velocity of the propeller.

If the critical pressure is close to the vapour pressure, cavitation incepts when the local pressure in the flow domain drops slightly below the vapour pressure. The difference between the pressure in an undisturbed flow and the local pressure in the flow field are non-dimensionalized in the same way as the cavitation number:

$$C_p = \frac{p - p_\infty}{\frac{1}{2}\rho q^2} \tag{77}$$

This gives the following relation to cavitation inception:

$$C_p = -\sigma_i \tag{78}$$

The ITTC recommends that the inception of tip vortex cavitation is Reynolds number scaled according to Eq. (49). The scaling of other cavitation types is not recommended unless reliable scaling data is available.

Cavitation inception on a propeller is usually plotted as the cavitation inception number versus the thrust coefficient K_T or propeller advance coefficient J. The different cavitation types are determined in the diagram. An example cavitation inception diagram is given in Figure 15. The operation region inside the innermost curves is free of cavitation. This region is called the cavitation bucket.

In reporting the cavitation behaviour of propellers, still figures or sketches of the cavitation patterns should also be included at the relevant operation points and at the different blade positions, and the fluctuations and unsteadiness of the cavity patterns should be discussed. Special types of cavitation, such as root or induced rudder cavitation, should be highlighted. Video recordings give a clear visual presentation of cavitation dynamics. It is also important to discuss the level of accuracy of the cavitation investigations.

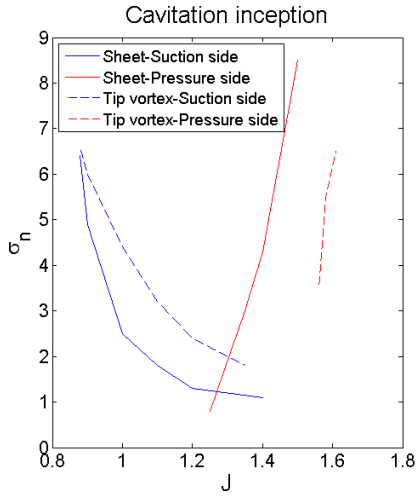

Figure 15. A cavitation inception diagram for a propeller.

The pressure fluctuations induced from a cavitating propeller are interesting from the ship design point of view. The pressure fluctuations should be determined from the rear hull with an appropriate resolution in space around the propeller. Low-frequency pressure fluctuations are presented as pressure pulse spectra in which the frequency is presented as multiples of the blade pass frequency. If the higher harmonics are of interest the spectra can be presented as a 1/3 octave band plot. The peaks in the pressure pulse spectra should then be connected to the cavitation phenomena around the propeller.

When observing cavitation noise, it should be noted that the environment has a significant influence on the noise behaviour. Acoustic waves reflect from the hull, the free surface, and the bottom of the sea. In addition, in test facilities the tunnel walls also reflect the acoustic waves. These factors must be taken into account when determining the noise emitted from the propeller or ship. The classification societies have detailed procedures for measuring the noise emitted from vessels.

1.4.2 Experimental methods

Experimental cavitation investigations are performed in cavitation tunnels or depressurized towing tanks, where the static pressure of the facility can be adjusted. The goal is to match the cavitation numbers applied in the tests to those relevant in full-scale applications.

A sketch of a cavitation tunnel is shown in Figure 16. The main parts of the cavitation tunnel are the propeller test section, honeycomb, impeller, propeller motor, vacuum pump and the instrumentation for measuring propeller thrust and torque. The propeller model and possible hull model are installed in the test section.

The test section is equipped with windows to enable visual observation. In many cases the propellers in cavitation tunnels are driven from the upstream of the test section. This

allows the inclusion of a rudder in the test configuration. The size of the test section is often limited. The wake to the propeller is generated by foreshortened models, wire frames, or plate arrays. An inclined shaft configuration can be considered in cases where the wake is weak at the propeller plane and variations in the angle of attack on the blades are caused mainly by oblique inflow to the propeller.

The flow in the cavitation tunnels is driven by an impeller, and a vacuum pump is used to adjust the pressure inside the tunnel. A honeycomb is located in front of the test section to straighten the flow field. Both the dissolved air and the air bubble concentration can be controlled by a dedicated device installed in the tunnel. The water quality should be monitored regularly throughout the cavitation tests to ensure steady and repeatable conditions. In depressurized towing tanks, the nuclei can be created by electrolysis in front of the propeller.

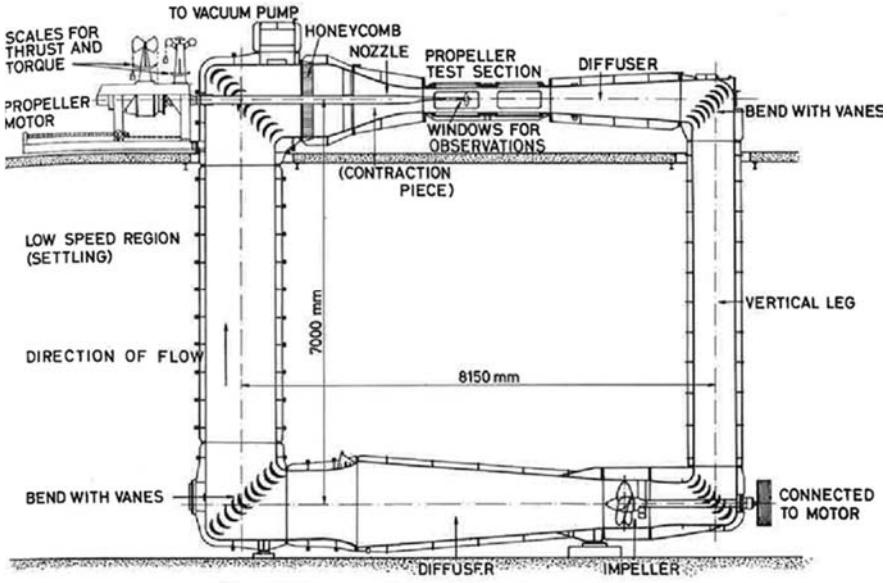

Figure 16. A sketch of a cavitation tunnel. (Figure taken from Harvald [1983].)

The main uncertainties in the model-scale cavitation tests are related to Reynolds number scaling and the size and distribution of the cavitation nuclei. At the full scale, the cavitation inception pressure is close to the vapour pressure. Keeping the difference between the vapour pressure and inception pressure the same at the model scale as at the full scale would cause the size of the cavitation nuclei to become visible and thus distort the observation of cavitation inception (Kuiper, 2011). Fortunately, the bubble size versus tension slope is not steep near the boundary of the stable and unstable equilibrium, as seen in Figure 5. This means that bubble size is not that critical from the cavitation inception point of view.

The density of the largest nuclei is smaller at the model scale than the full scale. If the nuclei density is insufficient, cavitation inception can be delayed significantly and inception can be intermittent. On the other hand, the largest nuclei can grow by gas diffusion, in which case the observed cavitation would be due to gaseous cavitation, not vapour cavitation. For this reason, it is recommended to measure the inception at a set interval, such as 1 or 10 seconds between events (ITTC, 2008).

The transition from laminar to turbulent flow can be enhanced by gluing roughness particles to the leading edge of the blade. The particles destabilize the boundary layer causing the transition to occur earlier. Local low pressure peaks also form around the roughness particles and tiny spots of cavitation occur even when the pressure outside the boundary layer is above the vapour pressure. The spots of cavitation grow suddenly as the pressure outside the boundary layer reaches the vapour pressure. The roughness elements also produce cavitation nuclei on the boundary layer. This improves the correlation of the bubble cavitation inception and the cavitation behaviour between the model scale and full scale (Kuiper, 2011).

Cavitation observations are traditionally conducted using still photographs, standard video recordings using a stroboscopic light, and high-speed video recordings. The stroboscopic light helps to give an impression of the cavitation extent at different blade positions in the wake field and of the deviation of the cavities between propeller revolutions. It must be noted that the dynamics of the cavities cannot be observed with a stroboscopic light.

The dynamics of cavitation is studied by high-speed video recordings. Bark et al. (2004) recommend that the frame rate in the high-speed video recordings should be between 3,000 and 10,000 frames per second in commercial testing. At lower frame rates blurring becomes significant, and with higher frame rates light levels become problematic. A recording time of one to two seconds has been found to be sufficient. Detailed examination of bubble collapse and rebound requires more than 100,000 frames per second (Bark et al., 2004).

The paint method is a commonly used method of investigating cavitation erosion. In this method, the propeller is painted with a soft paint and run for an appropriate time in a cavitation tunnel. The paint wears off at the locations where the cavitation bubbles collapse, thus indicating regions of potential cavitation erosion in full-scale applications.

Observation of cavities and related dynamics are traditionally limited to the cavity surfaces. However, Foeth (2008) applied particle image velocimetry (PIV) to study the dynamics of sheet cavitation also inside the vaporized structures. Foeth concluded that the use of PIV for cavitating flows requires the reflecting particles to be fluorescent in laser light. Image pre-processing is needed to reduce errors related to light reflection at the vapour–water phase transition boundary.

As regards full-scale cavitation analysis, vibration measurement signals, pressure pulses and noise are linked to visual observations of cavitation phenomena around the propeller and at the rear of the ship. Typically, a small hole is drilled in the bottom of the rear of the ship. A borescope is penetrated through the hull and the observations are recorded by a standard or high-speed video camera. Sunlight may provide adequate lighting for the recordings, although light enhancement is usually needed to ensure sufficient illumination. Clear water is required. The viewing angle of a borescope is 360 degrees. The borescope can be installed while in harbour, thus reducing investigation costs significantly.

1.4.3 Numerical models

The cavitation models used in codes based on lifting surface and boundary element methods (BEM) are usually capable of predicting sheet and tip vortex cavitation. The sheet cavitation extent is not known a priori and is determined iteratively so that the pressure in the cavity is uniform and equals the vapour pressure. The potential flow based methods cannot predict pressure side sheet cavitation in many cases.

Geurst (1961) developed a linearized, two-dimensional, and quasi-steady model based on the potential flow theory. Geurst's model predicts the cavity length and cross-section area over an infinitely thin camber line. Separate models are derived for partial and fully cavitating foils and the models are connected by a cubic spline fit in the transitional zone. Matusiak (1992) combined Geurst's cavitation model with a lifting surface theory of propellers. In the Matusiak model, the propeller is split into chordwise strips and the instantaneous cavitation extent is calculated from the angle of attack and the unsteady portion of the sectional load of each strip.

In the lifting surface methods the detachment point is located either at the leading edge of the foil or at the low pressure peak near the leading edge. Kinnas et al. (1998) developed an iterative method to predict the detachment point based on boundary layer separation. The cavity thickness is assumed to be zero at the closure of the sheet cavity. The linear cavitation theory predicts that the extent and volume of cavitation increase with increasing blade thickness. This is contrary to the results from experiments and non-linear cavitation methods. Kerwin et al. (1986) generalized the leading edge correction for cavitating propellers that was developed for cavitating hydrofoils by Kinnas (1985). The predicted cavitation extent was improved compared to predictions made with the panel code by decreasing the cavitation extent. The prediction of tip vortex cavitation inception is based on simplified vortex models, such as the Rankine vortex model, and on empirical data.

The BEM methods, also known as the panel methods, take more accurately into account the complex geometry of the propeller. In particular, the pressure peak at the leading edge of a blade is more accurately determined. The sheet cavitation inception point is predicted with the same assumptions as with the lifting surface method. The cavity surface is represented by a free streamline with a constant pressure.

The closure of the sheet cavity can be modelled in several ways. In the closed models the streamlines touch the foil behind the cavity and there form a stagnation point. This contradicts the assumption of constant pressure along the streamlines. Some improvements to the closed model can be made by introducing a near wake model at the trailing edge of the cavity. The near wake models remove the stagnation point at the closure of the cavity, but some empirical tuning of the models is needed, see, for example, Lemonier and Rowe (1988).

In the open models, the streamlines do not hit the foil surface. The rear thickness of the cavity can be imposed or it can be determined as function of the flow conditions. De Lange et al. (1996) calculated unsteady sheet cavitation with a BEM code by applying kinematic and dynamic boundary conditions on the foil and cavity surfaces. They succeeded in modelling the cavity growth, the re-entrant jet, and the break-off of the sheet cavity. The calculation stopped as the re-entrant jet touched the upper cavity interface.

Lee and Kinnas (2004) showed that coupling the modelling of sheet and tip vortex cavitation improves the correlation between the observed and calculated sheet cavitation near the tip of a propeller blade. If the modelling of the tip vortex cavitation was not utilized, the predicted sheet cavitation extent was too large at the tip region.

The methods based on potential flow theory have the clear drawback that they either neglect the effect of viscosity, or viscous drag is added by an empirical method. Including viscosity in the models also improves prediction of the dynamics related to the natural shedding of the sheet and tip vortex cavities. Friction can be included in the cavitation models by solving the Navier-Stokes equations. The evaporation and condensation of the liquid and vapour phases are modelled by a mass transfer term.

Two-phase modelling brings additional complexity in solving the Navier-Stokes equations. The water phase is nearly incompressible, whereas the vapour phase is highly compressible. The flow regimes of the two phases cannot always be distinguished clearly. The individual cavitation bubbles are too small and their number is too large to be modelled separately. The grid resolution has to be high in order to accurately model the dynamics related to the cavitating structures and to keep the numerical diffusion of the mixture within reasonable limits.

The Euler and Navier-Stokes equations, coupled with a transport equation for the void fraction or with two-phase flow equations or other cavitation closure model equations, were developed in the 1990s. The ITTC (1999) has categorized the cavitation models into four groups: interface tracking methods, volume of fluid methods, discrete bubble methods, and two-phase flow methods. The same categories are referred to in the studies by Koop (2008) and Lu (2010). The groups are described in brief below. The two-phase flow methods are given more attention as the cavitation model used in the present work belongs to this group. An extensive list of references of the different cavitation model groups has been presented by the ITTC (1999) and Koop (2008). The descriptions of the cavitation models given below refer primarily to these sources.

Interface tracking methods track the interface between the liquid and vapour phases. The level set, marker particles, and surface piercing methods belong to this group of Lagrangian methods. Cavitation is assumed to have a constant pressure equal to the vapour pressure, and the cavity is determined on a distinct streamline. As with the potential flow based methods, the fore body of the cavitation is generally well defined. The closure of the sheet cavity must be modelled with a wake model due to the natural unsteadiness of the cavity closure regime. These methods are limited to predicting the extent of the sheet cavity. They cannot predict the re-entrant jet or shedding of the cavity.

The **volume of fluid method** (VoF) was first introduced by Hirt and Nichols (1981). The method is traditionally used for free surfaces without a phase transition, such as air bubbles or surface waves. The method includes a transport equation for the void fraction that has a value of one or zero. The interface between the two mediums must be kept sharply defined. One alternative is to use a combination of upwind and downwind weighting to calculate the convective fluxes. One such method is the Compressive Interface Capturing Scheme for Arbitrary Meshes (CICSAM) developed by Ubbink (1997). To calculate cavitating flows, a mass transfer term must be included in the volume of fluid methods. Dieval et al. (1998) developed such a method with which they could predict the re-entrant jet and the natural shedding of a sheet cavity over a two-dimensional venturi

duct and a sharp step in geometry of an industrial component. Yuan et al. (2001) also combined a model for bubble dynamics with the VoF method.

The **discrete bubbles method** models the dynamics of a single bubble or a group of bubbles travelling through a pressure field. The applications also cover the collapse of a bubble cloud and the interaction of the bubbles and the bubble clouds with shock waves. Plesset and Prosperetti (1977) were the first to analytically describe the collapse and growth of individual vapour bubbles. Since then, intense research has been carried out to numerically investigate the dynamics of single and multiple cavitation bubbles.

Two-phase flow methods can be split into two main categories. The first is the **multi-component method** (or **multiple species method**), in which a full set of equations is used to describe the vapour and liquid phases. These include continuity, momentum, and energy conservation equations. Sometimes, the inert gas phase is modelled with its own set of equations. Such models can be used to study the behaviour of explosives, for example. The multi-component methods enable mechanical and thermal non-equilibrium to be taken into account. The two-phase flow modelling considerations are used to derive appropriate transfer relations in order to couple the different phases. These methods are assumed to be more general since they include more physics, but they are also computationally more expensive. To mention some references, Baer and Nunziato (1986) developed such a method for detonation waves in granular explosives; and Saurel and Lemetayer. (2001) proposed a compressible method that is hyperbolic, which they validated for various applications such as the interfaces between compressible materials, shock waves in condensed multiphase mixtures, homogenous two-phase flows (bubbly and droplet flows) and cavitation in liquids.

Homogeneous-mixture methods form the second main category of two-phase flow methods. These methods average the properties of a fluid containing multiple phases or components. The density and viscosity of the homogeneous mixture, for example, vary greatly in the fluid domain. It can be split into three subcategories: transport equation-based models (TEM), barotropic-flow methods, and homogeneous-equilibrium methods.

Transport equation based methods model the transport equation between the vapour and liquid phases for the volume or mass fractions. These methods assume that the pressure, velocity, and temperature of the phases are equal. This refers to the homogeneous mixture assumption. The source terms in the transport equations model the transition from one phase to the other. The methods take into account the physical rate of the processes through empirical laws for the source terms. A wide variety of proposed relationships exists in the literature. The transport equation models can be divided into bubble two-phase transport models and mass transfer rate models.

Bubble two-phase transport models were first introduced by Kubota et al. (1992). The density of the mixture was related to the motion of the bubbles and the related dynamics in the flow. The bulk flow contains cavitation nuclei that grow and collapse according to the Rayleigh or Rayleigh-Plesset equations in the surrounding conditions, such as pressure and temperature. Among many others, Aït-Bouziad (2006), Yuan et al. (2001) and Sauer and Schnerr (2000) have adopted this method. Singhal et al. (2002) and Zwart et al. (2004) have implemented empirical parameters in their models in order to model the production and destruction of vapour.

The **mass transfer rate model**, based on pressure-driven evaporation and condensation, was developed by Merkle et al. (1998). The evaporation and condensation source terms take into account the mass transfer rate between the vapour and liquid phases. The model has been used in modified and extended forms by several authors. Neaves and Edwards (2006) used the method with Euler equations, Huuva (2008) applied it to large eddy simulations, and Kuntz et al. (2000), Senocak and Shyy (2004a and 2004b), Saito et al. (2007), and many others to RANS equations.

The transport equation based methods can be considered as non-equilibrium methods. These methods are based on thermodynamic considerations of the source terms, as shown by Iben et al. (2002) and Berg et al. (2005). The methods presented in those papers include a full set of equations for the continuity, momentum, and energy conservation of liquid and vapour. An equation of state for the pure phases and the mixture must be added to enclose the system of equations.

Barotropic flow models couple the density of a mixture to pressure by means of a barotropic law $\rho = \rho(p)$ ranging from liquid density through a transitional zone to vapour density. The production of vorticity is an important aspect of the cavitating flows, especially in the closure region of the sheet cavity. Senocak et al. (2004a) noted that the vorticity production is a consequence of the baroclinic generation term $\nabla\frac{1}{\rho}\times\nabla p$. If an arbitrary barotropic equation is used, then the density gradients are parallel and the baroclinic torque is zero. This suggests that the physical models that utilize a barotropic equation fail to capture an experimentally observed characteristic of the cavitating flows. However, in the TEM approaches density is a function of the transport process. As such, the gradients of density and pressure are not necessarily parallel. TEM can therefore produce the baroclinic vorticity. The barotropic models have been used, among others, by Reboud and Delannoy (1994), Arndt et al. (2000), and Coutier-Delgosha (2007).

Homogeneous equilibrium models treat the pure water and pure vapour phases with suitable equations of state so that the equations are hyperbolic in space and time. The two-phase flow regime is forced to be in thermodynamic and mechanical equilibrium. A full set of continuity, momentum, and energy conservation equations are needed to model the equilibrium, as shown, for example, by Schmidt et al. (2006). The model returns the bulk density of the mixture based on the implemented temperature-related saturation-state relations. The phase transition, condensation shocks, and other multi-phase features can be captured with this method, although non-equilibrium effects cannot be captured. Two-phase wave propagation can, however, be studied by this method. The models are independent of empirical parameters other than the equations of state for the pure phases.

2. Numerical methodology

The numerical methodology used in the cavitating ship propeller calculations are explained in this section. The content of this section refers to the FINFLO User Guide (FINFLO, 2012) and Siikonen (2011), unless otherwise stated. A short general description of the code is given first. Then a more detailed explanation is given of the solution algorithm of the single- and multi-phase flows.

2.1 FINFLO code

The calculations presented in this thesis were performed with FINFLO, a general-purpose CFD code. The code development started in the late 1980s at the Helsinki University of Technology (HUT) (Siikonen et al., 1990). The code has been extensively validated and utilized also for propeller flows (Pylkkänen et al., 1998, Sánchez-Caja et al. 2006a, 2006b, and Martio et al., 2011, among others). The code also includes a method for calculating free-surface flows (Mikkola, 2000 and Li et al., 2001). The development work for the code still continues, and the Fluid Dynamics Unit of Aalto University recently implemented a cavitation model in FINFLO. The validation calculations of the cavitation model for ship propeller flows were performed at VTT and published by Sipilä and Martio (2008), Sipilä et al. (2009, 2011), and Sipilä and Siikonen (2012).

The flow simulations presented in this thesis are based on the solutions of the RANS equations using the pressure correction method. The volume of fluid method is applied to determine the cavitating regions in the calculation domain. The method belongs to the homogeneous mixture models, and the mass transfer rate model of Merkle et al. (1998) is implemented in the code to model the phase transitions. An equation of state has also been introduced in the code to determine the saturation pressure as a function of flow temperature ($p_{sat} = p(T)$). The cavitation model assumes that the flow is incompressible.

2.2 Single-phase flow

2.2.1 Flow equations

The RANS equations, the equations for turbulent kinetic energy k and dissipation of turbulence ε, and the scalar transport equation can be written as follows:

$$\frac{\partial U}{\partial t}+\frac{\partial (F-F_v)}{\partial x}+\frac{\partial (G-G_v)}{\partial y}+\frac{\partial (H-H_v)}{\partial z}=Q \tag{79}$$

where $U=(\rho,\rho u,\rho v,\rho w,E,\rho k,\rho\varepsilon,\rho\phi\ )^{\mathrm{T}}$. F, G, and H represent the inviscid fluxes and F_v, G_v, and H_v the viscous fluxes. The inviscid fluxes are written as follows:

$$F=\begin{pmatrix}\rho u\\ \rho u^2+p+\frac{2}{3}\rho k\\ \rho vu\\ \rho wu\\ \left(E+p+\frac{2}{3}\rho k\right)u\\ \rho uk\\ \rho u\varepsilon\\ \rho u\phi\end{pmatrix}$$

$$G=\begin{pmatrix}\rho v\\ \rho uv\\ \rho v^2+p+\frac{2}{3}\rho k\\ \rho wv\\ \left(E+p+\frac{2}{3}\rho k\right)v\\ \rho vk\\ \rho v\varepsilon\\ \rho v\phi\end{pmatrix} \tag{80}$$

$$H=\begin{pmatrix}\rho w\\ \rho uw\\ \rho vw\\ \rho w^2+p+\frac{2}{3}\rho k\\ \left(E+p+\frac{2}{3}\rho k\right)w\\ \rho wk\\ \rho w\varepsilon\\ \rho w\phi\end{pmatrix}$$

The velocity is $\vec{v} = u\vec{\imath} + v\vec{\jmath} + w\vec{k}$ with $\vec{\imath}, \vec{\jmath}$ and $\vec{k}$ representing the unit vectors in the *x*-, *y*-, and *z*-directions, respectively. The scalar variable is depicted by ϕ. The total internal energy *E* is defined as

$$E = \rho e + \frac{\rho \vec{v} \cdot \vec{v}}{2} + \rho k \tag{81}$$

where *e* is the specific internal energy. The source term *Q* has non-zero components for the equations of turbulence and possibly for the scalar equation. The viscous fluxes are written as follows:

$$F_v = \begin{pmatrix} 0 \\ \tau_{xx} \\ \tau_{xy} \\ \tau_{xz} \\ u\tau_{xx} + v\tau_{xy} + w\tau_{xz} - q_x \\ \mu_k(\partial k/\partial x) \\ \mu_\varepsilon(\partial \varepsilon/\partial x) \\ \mu_\phi(\partial \phi/\partial x) \end{pmatrix}$$

$$G_v = \begin{pmatrix} 0 \\ \tau_{xy} \\ \tau_{yy} \\ \tau_{yz} \\ u\tau_{xy} + v\tau_{yy} + w\tau_{yz} - q_y \\ \mu_k(\partial k/\partial y) \\ \mu_\varepsilon(\partial \varepsilon/\partial y) \\ \mu_\phi(\partial \phi/\partial y) \end{pmatrix} \tag{82}$$

$$H_v = \begin{pmatrix} 0 \\ \tau_{xz} \\ \tau_{yz} \\ \tau_{zz} \\ u\tau_{xz} + v\tau_{yz} + w\tau_{zz} - q_z \\ \mu_k(\partial k/\partial z) \\ \mu_\varepsilon(\partial \varepsilon/\partial z) \\ \mu_\phi(\partial \phi/\partial z) \end{pmatrix}$$

The viscous stress tensor involves both laminar and turbulent components. As the fluid is assumed to be Newtonian, the laminar stresses are modelled using the Stokes hypothesis. The Reynolds stresses $\rho u_i'' u_j''$ are included in the stress tensor τ_{ij} as follows:

$$\tau_{ij} = \mu\left[\frac{\partial u_j}{\partial x_i} + \frac{\partial u_i}{\partial x_j} - \frac{2}{3}(\nabla \cdot \vec{v})\delta_{ij}\right] - \overline{\rho u_i'' u_j''} + \frac{2}{3}\rho k \delta_{ij}. \tag{83}$$

The last term in the brackets is zero for incompressible flow. The calculation of Reynolds stresses is performed with a turbulence model in the RANS approach.

The turbulent kinetic energy $\frac{2}{3}\rho k \delta_{ij}$ and the pressure are connected and appear in the inviscid part of the momentum and energy fluxes. The diffusive part is connected with the viscous fluxes. The heat flux can also be written with laminar and turbulent parts as:

$$\vec{q} = -(\lambda + \lambda_t)\nabla T = -\left(\mu \frac{c_p}{Pr} + \mu_T \frac{c_p}{Pr_t}\right)\nabla T \tag{84}$$

where λ and λ_t are the molecular and turbulent thermal conductivity, respectively. The viscosity and Prandtl numbers are given as μ, μ_t, Pr, and Pr_t for the laminar and the turbulent parts, respectively. The specific heat at a constant pressure is given as c_p. The Prandtl numbers are defined as (White, 1991):

$$Pr = \mu \frac{c_p}{\lambda} \tag{85}$$

$$Pr_T = \mu_T \frac{c_p}{\lambda_t} \tag{86}$$

The diffusion of the turbulent and scalar variables are modelled as:

$$\mu_k \nabla k = \left(\mu + \frac{\mu_T}{Sc_k}\right)\nabla k \tag{87}$$

$$\mu_\varepsilon \nabla \varepsilon = \left(\mu + \frac{\mu_T}{Sc_\varepsilon}\right)\nabla \varepsilon \mu_T \frac{c_p}{\lambda_t} \tag{88}$$

$$\mu_\phi \nabla \phi = \left(\mu + \frac{\mu_T}{Sc_\phi}\right)\nabla \phi \tag{89}$$

where σ_k, σ_ε, and σ_ϕ are the appropriate Schmidt's numbers. The turbulent Schmidt number is the ratio between the turbulent viscous diffusion rate and the turbulent mass diffusion rate, i.e.:

$$Sc_t = \frac{\nu_t}{D_t}. \tag{90}$$

An equation of state is needed to close the equation system in a case where the energy equation is included. The pressure, velocity and temperature are solved. The density is calculated from $\rho = \rho(p,T)$ and the specific internal energy from $e = e(p,T)$. Viscosity and heat conductivity are assumed to be functions of temperature.

The pressure correction approach for incompressible flows is used to solve the RANS equations. The presentation of pressure in Eq. (80) is clumsy with respect to the pressure correction method. Instead, an effective pressure can be introduced:

$$p_{eff} = p + \frac{2}{3}\rho k = p_{dif} + p_\infty + \frac{2}{3}\rho k \tag{91}$$

where p_{dif} refers to the difference between the local pressure and the pressure in an undisturbed flow. A buoyancy term can be added to the above pressure equation if necessary.

2.2.2 Turbulence modelling

The turbulence model used in the present work is Chien's low Reynolds number k-ε turbulence model (Chien, 1982). The model has been traditionally used in propeller analyses performed at VTT. The correlation between the calculations and the model test results has been good, at least when comparing the global performance characteristics of the propellers.

The source term Q is given for Chien's model near a viscous surface as follows:

$$Q = \begin{pmatrix} P - \rho\varepsilon - 2\mu\dfrac{k}{y_n^2} \\ c_1\dfrac{\varepsilon}{k}P - c_2\dfrac{\rho\varepsilon^2}{k} - 2\mu\dfrac{\varepsilon}{y_n^2}e^{-y^+/2} \end{pmatrix} \tag{92}$$

where y_n is the normal distance from the wall and y^+ is the non-dimensional wall distance, defined as:

$$y^+ = y_n\frac{\rho u_\tau}{\mu} = y_n\frac{\sqrt{\rho\tau_w}}{\mu} = y_n\sqrt{\frac{\rho|\nabla\times\vec{V}|}{\mu}} \tag{93}$$

the so called wall velocity is depicted by $u_\tau = \sqrt{\tau_w/\rho}$ and τ_w is the shear stress on the wall. The production term of the turbulent kinetic energy is modelled as:

$$P = -\overline{\rho u_i'' u_j''}\frac{\partial u_i}{\partial x_j} = \left[\mu_t\left(\frac{\partial u_i}{\partial x_j}+\frac{\partial u_j}{\partial x_i}-\frac{2}{3}\delta_{ij}\frac{\partial u_k}{\partial x_k}\right)-\frac{2}{3}\delta_{ij}\rho k\right]\frac{\partial u_i}{\partial x_j}, \tag{94}$$

where the Boussinesq approximation is used for the Reynolds stresses. The eddy viscosity is calculated in the *k-ε* model from:

$$\mu_t = c_\mu \frac{\rho k^2}{\varepsilon} \tag{95}$$

The production of turbulence is limited as:

$$P = \min(P, 10\varepsilon) \tag{96}$$

This prevents unphysical growth of eddy viscosity near the stagnation point, but does not affect the flow in the well-behaving regions of the flow field.

The equations for k and ε in the small Reynolds number *k-ε* model can be presented in two-dimensions as (FINFLO User Guide, 2012):

$$\frac{\partial \rho k}{\partial t}+\frac{\partial \rho u_i k}{\partial x_i} = \frac{\partial}{\partial x_i}\left[\left(\mu+\frac{\mu_t}{\sigma_k}\right)\frac{\partial k}{\partial x_i}\right] + P - \rho\varepsilon \tag{97}$$

$$\begin{aligned}\frac{\partial \rho \tilde{\varepsilon}}{\partial t}+\frac{\partial \rho u_i \tilde{\varepsilon}}{\partial x_i} = {} & \frac{\partial}{\partial x_i}\left(\mu+\frac{\mu_t}{\sigma_\varepsilon}\right)\frac{\partial \tilde{\varepsilon}}{\partial x_i} + c_1 f_1 \frac{\tilde{\varepsilon}}{k}P - c_2 f_2 \varepsilon \frac{\rho\tilde{\varepsilon}^2}{k} + \\ & + c_3 c_\mu \frac{k^2}{\varepsilon}\frac{\partial k}{\partial x_i}\frac{\partial}{\partial x_i}\left(\frac{\tilde{\varepsilon}}{k}\right) + E\end{aligned} \tag{98}$$

where $\varepsilon = \tilde{\varepsilon} + D$, $P = \nu_t\left(\frac{\partial u_i}{\partial x_j}\right)^2$, $\nu_t = c_\mu f_\mu \frac{k^2}{\varepsilon}$, $c_1 = 1.44$, $c_2 = 1.92$, $c_3 = 0.0$, and $c_\mu = 0.09$. Furthermore, the additional functions are defined for Chien's low Reynolds number model as $f_\mu = 1 - e^{-0.0115y^+}$, $f_1 = 1$, $f_2 = 1 - \frac{2}{9}e^{-\left(\frac{Re_t}{6}\right)^2}$ $D = -2\frac{\nu k}{y_n^2}$, and $E = -2\frac{\mu\tilde{\varepsilon}}{y_n^2}e^{-0.5y^+}$.

2.2.3 Spatial discretization

The code uses a finite volume technique. The flow equations are presented in an integral form as:

$$\frac{d}{dt}\int_V UdV + \int_S \vec{F}(U)\cdot d\vec{S} = \int_V Q(U)dV \tag{99}$$

for an arbitrary fixed region V with a boundary S. The flux is calculated in the normal direction of the boundary, i.e. $\mathrm{d}\vec{S} = \mathrm{d}S\vec{n}$, where $\vec{n}$ is a unit normal vector of the face. The integration for an individual cell, i, becomes:

$$V_i\frac{dU_i}{dt} = \sum_{faces} -S\hat{F} + V_iQ_i \tag{100}$$

where the sum is taken over all faces of the cell. The flux through a face is calculated as:

$$\hat{F} = n_xF + n_yG + n_zH \tag{101}$$

2.2.4 Flux calculations

The viscous fluxes present in F_v, G_v, and H_v include derivatives on the cell surfaces. The derivatives are defined as follows:

$$\nabla T_{i+1/2} \approx \nabla T_{i+1/2} - \left(\overline{\nabla T}_{i+1/2}\cdot\vec{s} - \frac{\partial T}{\partial s}\right)\vec{s} \tag{102}$$

where the lower index $(i+1/2)$ refers to the face between the nodes (i) and (i+1),

$$\overline{\nabla T}_{i+1/2} = \frac{1}{2}(\nabla T_i + \nabla T_{i+1}) \tag{103}$$

and $\vec{s}$ is a unit vector along a line connecting the two neighbouring cells. The derivative $\partial T/\partial s$ is calculated using the distance Δs between the two cells. By using the finite volume and the tensor forms, the calculation of the derivatives on a cell surface (i+1/2) can be written as:

$$\vec{n}_{i+1/2}\cdot(\nabla T)_{i+1/2} \approx \alpha\frac{T_{i+1}-T_i}{\Delta s} + \overline{\nabla T}_{i+1/2}\cdot\left(\vec{n}_{i+1/2} - \alpha\vec{s}_{i+1/2}\right), \tag{104}$$

where $\alpha = \vec{n}_{i+1/2} \cdot \vec{s}_{i+1/2}$. The derivatives at the cell centroids are calculated utilizing the Gauss theorem. With an orthogonal grid $\vec{n}_{i+1/2} \equiv \vec{s}_{i+1/2}$ and $\alpha = 1$. The equation above simplifies then to the form:

$$\vec{n}_{i+1/2} \cdot (\nabla T)_{i+1/2} \approx \frac{T_{i+1} - T_i}{\Delta s} \tag{105}$$

The discretization of the convective fluxes differs between the compressible and incompressible solutions. Approximate Riemann solvers contain intrinsic dissipation owing to the upwind interpolation methods. In the case of Roe's method (Siikonen, 1995) the convective fluxes are calculated as:

$$F_{i+1/2} = \frac{1}{2}(F_{i+1} + F_i) - \frac{1}{2}\left|\tilde{A}\right|(U_{i+1} - U_i), \tag{106}$$

where F is the flux vector in the x-direction and $\tilde{A}$ is the Jacobian of the flux vector based on the Roe's average. The equation above takes of the coupling of the solution between the neighbouring points. For the solution, Eq. (24) is applied in the direction of the surface normal of the cell. A second-order accuracy is obtained by replacing the cell values with the extrapolated values U^l and U^r on both sides of the cell face. Eq. (106) is fairly complicated, but it takes of the coupling of the solution between the neighbouring points. The amount of dissipation depends on the interpolation method; with central differencing the dissipation term drops out.

In the case of an incompressible flow, additional dissipation is added to the solution to prevent a checkerboard solution in the collocated grids. A Rhie and Chow type method has been implemented in the code in the simplified form presented by Johanssen and Davidson (1995). The dissipation is added to the cell-face mass flux by approximating the pressure derivatives along the grid coordinate directions:

$$\bar{u}_{i+1/2} = \frac{1}{2}(\bar{u}_{i+1} + \bar{u}_i) - C\frac{S_{i+1/2}}{4A_{P,i+1/2}}(p_{i+2} - 3p_{i+1} + 3p_i - p_{i-1}) \tag{107}$$

where $\bar{u}$ is the convective velocity $\bar{u} = \vec{n} \cdot \vec{v}$ that is based on the normal vector on the cell surface $i + 1/2$. The constant C is used to reduce the dissipation, and the multiplier A_P comes from the original Rhie and Chow interpolation (Rhie & Chow, 1983). The factor of 4 can be combined with the constant C. The dissipation term is of fourth order and the truncation error of second order. The multiplier A_P is calculated as $A_P = S\rho U_\infty$ for a one-dimensional case. The original calculation of A_p included a dependence on the time step Δt. The time derivative is simply left out in some implementations. The constant C has a value $C < 0.1$. Sometimes a larger value is utilized. The absolute pressure present in Eq. (107) is replaced by the pressure difference compared to a reference pressure.

2.2.5 Pressure correction method

The pressure correction method is applied at the implicit stage. The method implemented belongs to the coupled pressure correction methods. The continuity and momentum equations are coupled and the residuals are calculated simultaneously. In the traditional segregated approach the equations are solved in series and the Poisson equation is solved for the pressure corrections or the pressure. The residuals are calculated at different stages of the algorithm.

The flow equations must be presented in a linearized form. The *x*-momentum equation is linearized as:

$$V_i \frac{\delta(\rho_i u_i)}{\Delta t} = -\sum_j \dot{m}_j^{n+1} u_i^{n+1} - \sum_j S_j n_{x,j} p_j^n + \sum_j S_j \left(\vec{n}_j \cdot \tau_{ij}\right)_{x,j}^{n+1} \tag{108}$$

where *j* refers to the surfaces of a computational cell and *n* refers to the iteration cycle. The continuity equation is linearized as:

$$V_i \frac{\delta\rho}{\Delta t} = -\sum_{\mathrm{j}} \dot{m}_j^n - \sum_j \delta\dot{m}_j = R_i^c - \sum_{\mathrm{j}} \delta\dot{m}_j \tag{109}$$

where R^c is the residual of the continuity equation from the *n*:th iteration cycle. In an incompressible case $\delta\rho$ is the imbalance in mass flows at the time step *n*. The momentum flux is linearized as $\dot{m}_j^{n+1} u_j^{n+1} \approx \dot{m}_j^n u_j^n + \dot{m}_j^n \delta u_i + u_i \delta\dot{m}_j$. The friction term is linearized using the approximation of Eq. (105). Linearizing the *x*-momentum equation and taking into account the linearized continuity equation can be done by dropping out the term $\sum_j (u_i - u_j)\delta\dot{m}_j$ as follows:

$$V_i \rho_i \frac{\delta u_i}{\Delta t} + R_i^c \delta u_i = R_i^{M_x} - u_i R_i^c - \sum_{\mathrm{j}} \dot{m}_j \delta u_j + \sum_j \frac{S_j \mu_j}{\Delta s_j} \left(\delta u_j - \delta u_i\right) \tag{110}$$

where R^{M_x} is the residual of the *u*-momentum equation from the *n*:th iteration cycle. Further simplification is achieved by using a first-order upwind method for the linearized convection term and dividing the mass flows into groups in and out of the computational cell. By applying the definition of the mass imbalance $R_i^c + \sum_{out} \dot{m}_j = -\sum_{in} \dot{m}_j$, the final form of the linearized *x*-momentum equation is obtained:

$$\left(\frac{V_i \rho_i}{\Delta t} - \sum_j \dot{m}_j + \sum_j \frac{S_j \mu}{\Delta s_j}\right) \delta u_i + \sum_{in} \dot{m}_j \delta u_j - \sum_{\mathrm{j}} \frac{S_j \mu_j}{\Delta s_j} \delta u_j = R_i^{M_x} - u_i R_i^c. \tag{111}$$

The viscosity μ is replaced by $(\mu + \mu_T)$ for the turbulent flows. The term δu_j contains the unknown velocities from the neighbouring cells behind the cell-surface j. The resulting equation has a recalculated residual on the right-hand side. In a traditional pressure correction method the residual of the continuity equation is zero. The effect of the mass imbalance of the present method is filtered away by the modified residual in the above equation.

Compass directions offer a convenient means of representing the implicit stage. For a three-dimensional structured grid the following matrix components can be written:

$$\begin{aligned}
a_{i,i-1} &\equiv A_{W,i} = -\max(\dot{m}_{i-1/2}, 0) - \left[\frac{S\mu}{\Delta s}\right]_{i-1/2} \\
a_{i,i+1} &\equiv A_{E,i} = -\max(-\dot{m}_{i+1/2}, 0) - \left[\frac{S\mu}{\Delta s}\right]_{i+1/2} \\
a_{i,i-imax} &\equiv A_{S,i} = -\max(\dot{m}_{j+1/2}, 0) - \left[\frac{S\mu}{\Delta s}\right]_{j-1/2} \\
a_{i,i+imax} &\equiv A_{N,i} = -\max(-\dot{m}_{j+1/2}, 0) - \left[\frac{S\mu}{\Delta s}\right]_{j+1/2} \\
a_{i,i-imax\times jmax} &\equiv A_{T,i} = -\max(-\dot{m}_{k+1/2}, 0) - \left[\frac{S\mu}{\Delta s}\right]_{k+1/2} \\
a_{i,i+imax\times jmax} &\quad A_{B,i} = -\max(-\dot{m}_{k+1/2}, 0) - \left[\frac{S\mu}{\Delta s}\right]_{k+1/2} \\
a_{i,i} &\equiv A_{P,i} = \frac{V_i \rho_i}{\Delta t} - A_{W,i} - A_{E,i} - A_{S,i} - A_{N,i} + \\
&\qquad\qquad -A_{T,i} - A_{B,i} + A_{q,i}
\end{aligned} \tag{112}$$

where a possible contribution of a source term linearization $A_{q,i}$ is added to the diagonal term $A_{P,i}$. Similar equations are obtained for the other momentum equations. After solving the equations above, the intermediate velocities are obtained from $u^* = u^n + \delta u$. Eq. (111) and the other corresponding equations are solved by an algebraic multigrid method. The equations are normalized so that the diagonal term $A_P = 1$ to improve the convergence. The scalar equations become similar to Eq. (111) after linearization.

There is also an option to calculate the energy equations in the code. However, as heat transfer is not significant in propeller applications the energy equations are not utilized in the present work.

The pressure correction method is based on the SIMPLE approach. The velocity corrections are calculated as:

$$u'_{i+1/2} = -\frac{S_{i+1/2} n_{x,i+1/2}}{\bar{A}_{P,i+1/2}} (p'_{i+1} - p'_i) \tag{113}$$

where n_x is the x-component of the surface normal. The corrections for the other velocity components are calculated similarly. The coefficient $\bar{A}_{P,i+1/2}$ is calculated as:

$$\frac{1}{\bar{A}_{P,i+1/2}} = \frac{1}{2}\left(\frac{1}{\bar{A}_{P,i+1}} + \frac{1}{\bar{A}_{P.i}}\right) \tag{114}$$

As the pressure corrections are computed the pressures are updated with:

$$p^{n+1} = p^n + \alpha_p p', \tag{115}$$

where α_p is an under-relaxation coefficient. The needed under-relaxation is high, typically $\alpha_p < 0.05$. This is due to the flat cells related to the low Reynolds number approach utilized to solve the boundary layer flow. The convergence is, however, more dependent on the local time-step size, which is calculated from the Courant number $CFL = u\Delta t/\Delta x$. The velocity corrections are finally made for the cell centres and obtained in the *x*-directions as follows:

$$u_i' = -\frac{1}{\bar{A}_{P,i}} \sum_j S_j n_{x,j} p_j', \tag{116}$$

where the pressure at the cell surfaces is calculated as the average of the neighbouring cells. The corrections for the other velocity components are calculated similarly. The velocities are updated finally as:

$$u^{n+1} = u^n + \alpha_u u' \tag{117}$$

where the under-relaxation factor for the velocity is of the order of $\alpha_u = 0.5$. The velocities do not fulfil the continuity equations exactly but the mass balance converges with the other balances during the simulation.

2.2.6 Turbulence equations

The turbulence equations were solved similarly to the other scalar equations. The source terms are non-linear and thus require special consideration. The turbulence equations give the eddy viscosity, which affects the whole solution.

The negative source terms were linearized only to improve the stability of the calculations. The terms related to the wall distances were not linearized. The dissipation term in the *k*-ε turbulence model is written in the *k*-equation as:

$$-\rho\varepsilon = -\frac{c_\mu}{\mu_T}(\rho k)^2 \tag{118}$$

The production term is positive and cannot be linearized. There is a strong coupling between the flow field, turbulent viscosity, and the production term P. Consequently, to reduce the stiffness of the equation set, the following was introduced:

$$\frac{\partial P}{\partial U} = -\frac{\partial P}{|\Delta U_{max}|} \tag{119}$$

The maximum change in U caused by P is then limited to $|\Delta U_{max}|$. The resulting Jacobian of the source term then becomes:

$$\frac{\partial Q}{\partial U} = \begin{pmatrix} -\frac{|P|}{|(\Delta k)_{max}|} - 2\frac{\rho\varepsilon}{k} & 0 \\ 0 & -\frac{|P|}{|(\Delta\varepsilon)_{max}|} - 2c_2\frac{\rho\varepsilon}{k} \end{pmatrix} \tag{120}$$

where the maximum changes are evaluated using the present values of k and ε as:

$$|(\Delta k)_{max}| = \frac{k}{C_k} \quad |(\Delta\varepsilon)_{max}| = \frac{\varepsilon}{C_\varepsilon} \tag{121}$$

The constants are set to $C_\varepsilon = 5$ and $C_k = 2C_\varepsilon$. The turbulent kinetic energy may grow faster than its dissipation, resulting in unphysical high values of turbulent viscosity. This can especially take place close to the stagnation point. To prevent unphysical growth of turbulent viscosity, a maximum value was set for μ_T.

2.2.7 Multigrid methods

The multigrid method implemented in the code follows the principles of Jameson and Yoon (1986) with a simple V-cycle method. With the structured grids the coarser grid levels were obtained by taking into account every second grid point in each direction compared to the finer level grid. The steps in the multigrid method are described below. The grid level is depicted by h_i with h_1 being the finest grid level.

1. Calculate the residual vector R_{h_1} of all equations to be solved on the finest grid level.
2. Perform the implicit phase and update the solution.

The previous steps do not differ from the procedure performed with a single grid. The following steps are repeated until the coarsest grid level is reached.

3. Recalculate the residual $R_{h_{i-1}}$ on the previous grid level.
4. Calculate a new residual using the forcing function $P_{h_{i-1}}$ as:

$$R^*_{h_{i-1}} = R_{h_{i-1}} + P_{h_{i-1}} \tag{122}$$

There is no forcing function on the second grid level. The residual is then $R^*_{h_{i-1}} = R_{h_{i-1}}$

5. Transfer the residual $R^*_{h_{i-1}}$ and the variables from grid h_{i-1} to the next coarser grid h_i. Transfer of the variables and the residuals is performed as:

$$U^t_{h_i} = \sum \left(V_{h_{i-1}} U_{h_{i-1}} / V_h \right) \tag{123}$$

and

$$R^t_{h_i} = \sum R^*_{h_{i-1}} \tag{124}$$

The sum is taken over the cells that approximately cover the cell on the coarse grid.

6. alculate the residual R_{h_i} on the new grid level using the transferred values of $U^t_{h_i}$.kjlö
7. Calculate the forcing function from:

$$P_{h_i} = R^t_{h_i} - R_{h_i} \tag{125}$$

8. Recalculate the residual from:

$$R^*_{h_i} = R_{h_i} + P_{h_i} \tag{126}$$

9. Perform the implicit phase using $R^*_{h_i}$ as a residual and update the solution U_{h_i} on grid h_i.

After the coarsest grid level is reached, the corrections are transferred back to the finer levels. Let $U^+_{h_{i+1}}$ be the final value of $U_{h_{i+1}}$ resulting from the correction calculated on grid

h_{i+1} and the correction transferred from grid h_{i+2}. The final value $U_{h_i}^+$ at grid level h_i is then calculated as:

$$U_{h_i}^+ = U_{h_i} + I_{h_{i+1}}^{h_i}\left(U_{h_{i+1}}^+ - U_{h_{i+1}}^t\right) \tag{127}$$

where $I_{h_{i+1}}^{h_i}$ is the interpolation operation that transfers the difference $U_{h_{i+1}}^+ - U_{h_{i+1}}^t$ from the coarse grid level to the appropriate fine grid. The calculation on the coarse grid levels is performed similarly to the fine grid level, except the first-order discretization is applied on the coarse grid levels. The solutions on the coarse grid levels are based on the residuals of the first grid level. The first-order discretization in the coarser grid levels does not affect the accuracy of the solution. The low-level discretization on the coarse grid levels improves the stability of the calculation and decreases the computational effort. It also allows the use of larger time steps at the coarser grid levels, which accelerates the convergence of the solution.

Regarding the turbulence calculations, some modifications were made to the multigrid methodology to increase the stability of the convergence. The solution of the turbulence equations is more non-linear than that of the laminar flow. The k- and ε-corrections between the grid levels are limited in the multigrid method. The turbulent viscosity was calculated only at the finest grid level due to its non-linear dependence on the turbulence quantities and the shape of the boundary layer.

In the case of multi-phase flows, the modifications to the multigrid methodology are similar to those in the turbulent flows. The transfer of the mass transfer term from the coarser grid levels is limited. The multigrid method has, however, been shown to be unstable in the multi-phase simulations. For this reason, the algebraic multigrid method was not utilized in the present cavitation simulations.

The code also includes the so-called full multigrid method. In this method, the simulations are performed first at the coarser grid levels. The result of the simulation at the coarser grid level is then interpolated to the finer grid level and used as the initial guess for the simulation. This accelerates the convergence at the finer grid levels significantly. An additional benefit of the full multigrid method is that the quality of the results at the coarser grid levels can be estimated before performing the heavy calculations at the finest grid levels.

2.2.8 Rotating reference frame

A quasi-steady solution can be found for the flows in a rotating motion in cases where the geometry of the problem is symmetric in a rotating coordinate system (or a rotating reference frame). An example of such a problem would be a ship propeller in a uniform axial inflow. The flow equations must be transported to the rotating coordinate system if a quasi-steady solution is preferred.

The velocity components can be presented in a fixed inertial coordinate system even if the coordinate system is rotating. The rotating velocity of the coordinate system (or the grid) is $\vec{\omega} = \vec{\Omega} \times \vec{r}$. The connection between the velocity in a rotating coordinate system $\vec{v}_r$ and in a fixed coordinate system $\vec{v}$ is expressed as:

$$\vec{v}_r = \vec{v} - \vec{\Omega} \times \vec{r} \tag{128}$$

The left-hand side of the momentum equations can be written as (Siikonen & Pan, 1992; Siikonen, 2006):

$$\frac{\partial}{\partial t}(\rho\vec{v}) + \nabla \cdot (\rho\vec{v}_r\vec{v}) + \vec{\Omega} \times \vec{v}, \tag{129}$$

The only change in the momentum equation in a rotating and a fixed coordinate system is that the convective velocity $\vec{v}$ is replaced by $\vec{v}_r$ and a centrifugal force term $\vec{\Omega} \times \vec{v}$ is added to the equation. The convective velocity must be changed also in other flow equations. The inviscid flux term in the x-direction becomes then:

$$F_r = \begin{pmatrix} \rho v_{rx} \\ \rho u v_{rx} + p + \frac{2}{3}\rho k \\ \rho v v_{rx} \\ \rho w v_{rx} \\ \left(E + \frac{2}{3}\rho k\right) v_{rx} + pu \\ \rho v_{rx} k \\ \rho v_{rx} \varepsilon \\ \rho v_{rx} \phi \end{pmatrix} \tag{130}$$

where v_{rx} refers to the x-component of v_r. Similar modifications hold also for the other velocity components. It is to be noted that pressure in the energy equation is not a convective quantity but only the total internal energy.

The other equations remain the same in a rotating coordinate system as in a fixed coordinate system. The rotating coordinate system does not affect the viscous fluxes or the pressure gradient.

2.3 Multi-phase flow

Many of the procedures used to calculate a single-phase flow are valid also for multi-phase flow calculations. Some modifications to the calculation procedure are nevertheless needed, as discussed in the following.

2.3.1 Flux calculation

The momentum flux can be calculated in a similar manner in the present homogeneous multi-phase flow model as in the case of a single-phase flow. The implementation is done for the liquid and gas phases separately. The mixture equations are obtained as a sum of the individual phase balances.

The mixture density is calculated as:

$$\rho = \alpha_v \rho_v + (1 - \alpha_v)\rho_l, \tag{131}$$

The void fraction α_v is used in the flux calculation instead of the fluid quality x, which is significantly smaller compared to α as seen from the relation $\alpha\rho_v = x\rho$ due to the fact that the vapour density is very small. The MUSCL formula is applied to calculate the void fraction for the mass flux. The nodal average values of the void fraction are used for the pressure gradient, heat flux, and viscous terms. The pressure is also calculated as an average in the momentum and energy equations.

The convective velocity is calculated similarly to the single-phase flow. The mass fluxes are calculated separately for the individual phases as $\dot{m}_k = \alpha_k \rho_k \bar{u}$, where $k = v$ or l and α_k is MUSCL-interpolated. The mass fluxes are then applied in the calculation of the momentum and energy fluxes. The homogeneous mixture of the phases is used to solve the momentum equations and the calculation procedure is the same as in the case of a single-phase flow.

2.3.2 Cavitation model

The cavitation model implemented in the code is based on two continuity equations and on the momentum and turbulence equations for the mixture, see also Siikonen (1987). The model is homogeneous and the pressure difference compared to the saturation pressure drives the mass transfer. The flow is assumed to be incompressible so the shock waves related to the collapse of the cavitation structures cannot be well predicted by the implemented model.

The continuity equations for the two phases contain source terms for the mass transfer, i.e. for evaporation and condensation. Since the pressure difference to the saturation pressure drives the mass-transfer, the pressure in the vaporised regions remains close to the saturation pressure. In the evaporating regions the local pressure is slightly below the

saturation pressure and in the condensating regions slightly over the saturation pressure. In the present simulations, the local pressure difference is maximum few dozen Pascals below the saturation pressure in evaporating regions. The absolute difference between the local pressure and the saturation pressure is lower in condensating regions. In reality, pressure and temperature rise very rapidly inside collapsing cavitation bubbles. These phenomena cannot be predicted with the implemented cavitation model.

The vapour properties in the code are evaluated by curve fits to the experimental data. The saturation pressure and the saturation temperature are fitted with the semi-empirical Antoine equation:

$$\log(p_{sat}) = A - \frac{B}{C + T_{sat}} \tag{132}$$

where A, B, and C are empirical constants. Typical values for the parameters are A = 5.40221 bar, B = 1838.675 bar°C, and C = -31.737°C (NIST Chemistry Webbook). The density of vapour is a function of both temperature and pressure. The density is determined from a linear combination of isobaric density curves as a function of temperature (Siikonen et al., 2008):

$$\rho_v = \sum_{i=1}^{n} \rho_v(T)_i \, f_i(p) \tag{133}$$

where the weighting function f_i is determined as:

$$f_i(p) = \max\left[0, \min\left(\frac{p - p_{i-1}}{p_i - p_{i-1}}, \frac{p_{i+1} - p}{p_{i+1} - p_i}\right)\right] \tag{134}$$

where p_i are the constant pressures at which the gas densities are determined. A second order polynomial fit is applied to the gas densities at constant pressure and varying temperature:

$$\rho(T)|_p = a_0 + a_1 T + a_2 T^2 \tag{135}$$

The formulation above allows direct calculation of $\partial\rho/\partial T|_p$. For an isothermal density change discontinuities are present. The following approximation gives accurate results for a wide range of pressure and temperature:

$$\frac{\partial \rho}{\partial p}|_T = \frac{\rho}{p}. \tag{136}$$

The gas continuity is written in terms of the mass quality (fraction) $x_g = x$ which leads to a simple implicit stage. The coefficients are the same as in Eq. (112). In calculating the mass flux, the mass quality is stored and used in the implicit solution. The gas quality equation does not have a diffusion term. Instead, an under-relaxation term is added on the diagonal of the solution matrix:

$$\frac{V_i|\Gamma_i|}{\Delta x_{max}}. \tag{137}$$

where the maximum change of quality is determined by:

$$\Delta x_{max} = C_x \max(x, 1-x) + \varepsilon_x \tag{138}$$

with $C_x = 0.05$ and $\varepsilon_x = 1 \times 10^{-6}$ being empirical constants. The value of ε_x is determined based on numerical tests. The limiter above suppresses the maximum change in the gas quality to 5%. Due to the high difference in vapour and liquid water densities, the mass quality x = 0.5 refers to a void fraction of α_v > 0.999 at the atmospheric pressure. For higher void fractions more under-relaxation is given so that the void fraction can never exceed unity.

The pressure correction equation for the multi-phase flow is derived from the continuity equations. To fulfil the continuity equation for the individual phases, the following linearized form for the continuity equation of the multi-phase flow is applied:

$$\begin{aligned}&\left[\frac{V_i\rho_{k,i}}{\Delta t} + \sum_{\text{out}} S_j \rho_{k,i} \bar{u}_j\right]\Delta\alpha_{k,i} + \left[\frac{V_i\alpha_{k,i}}{\Delta t} + \sum_{\text{out}} S_j \alpha_{k,i} \bar{u}_j\right]\frac{\partial \rho_{k,i}}{\partial p} p_i' + \\ &+\left[\frac{V_i\alpha_{k,i}}{\Delta t} + \sum_{\text{out}} S_j \alpha_{k,i} \bar{u}_j\right]\frac{\partial \rho_{k,i}}{\partial h_k}\Delta h_{k,i} + \sum_j S_j \alpha_{k,j} \rho_{k,j} \bar{u}_j' = \Delta \dot{m}_{k,i}\end{aligned} \tag{139}$$

This equation is simplified significantly by dropping out the enthalpy term and the $\sum_{\text{out}}$ −sums. The change in the void fraction is eliminated by the fact that $\Delta\alpha_v$ = -$\Delta\alpha_l$. The equation above simplifies then to the form:

$$\frac{V_i}{\rho_i c_i^2 \Delta t} p_i' + \frac{1}{\rho_{k,i}} \sum_{k,j} S_j \alpha_{k,j} \rho_{k,j} \bar{u}_j' = -\sum_k \frac{\Delta \dot{m}_{k,i}}{\rho_{k,i}} \tag{140}$$

where c is the speed of sound in a two-phase mixture. The speed of sound is determined as $1/c^2 \approx \partial\rho/\partial p$. In a mixture speed of sound is calculated using Eq. (1). The final form of the pressure correction equation can be written in the form:

$$\left[\frac{mV_i}{\rho_i c_i^2 \Delta t} + \frac{V_i |\Gamma_i|}{\Delta p_{max}} \left(\frac{1}{\rho_{v,i}} - \frac{1}{\rho_{l,i}}\right)\right] p_i' + \sum_{k,j} \frac{S_j^2}{\bar{A}_{P,j}} (p_{j+}' - p_i') = -\sum_k \frac{\Delta \dot{m}_{k,i}}{\rho_{k,i}} \tag{141}$$

where p_{j+}' is the pressure change in the cell on the other side of the face j, and m is the grid level applied in the multigrid algorithm. Pseudo-linearization is applied to the mass transfer term. The maximum change in pressure caused by Γ is limited to:

$$\Delta p_{max} = |p - p_{sat}| + \varepsilon_p \tag{142}$$

where the empirical constant $\varepsilon_p = 0.01$ Pa is used. An under-relaxation factor of 0.5 is applied to the change in the mass transfer term.

The mass transfer model utilized in the present simulations is similar to that of Merkle et al. (1998). The mass transfer is modelled as:

$$\Gamma_l = \frac{C_{dest} \rho_l \alpha_l \min[0, p - p_{sat}]}{{}^1\!/_2 \rho_\infty V_\infty^2 (L_{ref}/V_{ref})} + \frac{C_{prod} \rho_v \alpha_v \max[0, p - p_{sat}]}{{}^1\!/_2 \rho_\infty V_\infty^2 (L_{ref}/V_{ref})} \tag{143}$$

The empirical parameters C_{dest} and C_{prod} are utilized to tune the simulations. In most of the present simulations the parameters are set to $C_{dest} = C_{prod} = 350$. The influence of the empirical parameters on the cavitating tip vortex is studied by systematically varying C_{dest} and C_{prod}.

The implemented cavitation model also calculates heat transfer. However, in cavitating ship propeller flows heat transfer is not an important phenomenon and can be neglected. Thus, in the present calculations the energy residuals are calculated but are set explicitly to zero.

3. Validation cases

The cavitation model was validated for propeller flows in a uniform inflow and in a wake field. The cavitation tests for the uniform inflow case were performed in Potsdam Model Basin (SVA) in Germany. The model tests were performed for the Workshop on Cavitation and Propeller Performance held together with the Second International Symposium on Marine Propulsors (smp'11). The results of the full test programme for the analysed propeller are presented by Barkmann (2011), Mach (2011), and Heinke (2011).

The cavitation tests for the propeller working in a wake field were performed by the Italian Ship Model Basin CNR-INSEAN at the Italian Navy Cavitation Tunnel (CEIMM). The results of the cavitation tests were used as validation material also in the EU project VIRTUE under the 6th Framework Programme. The results of the extensive test programme utilized for the analysed propeller have been presented by Pereira et al. (2004a and 2004b).

3.1 Propeller in a uniform inflow

The propeller investigated in uniform inflow conditions is the Potsdam Propeller Test Case (PPTC) propeller of SVA Potsdam. The propeller is a model-size controllable pitch propeller with a diameter of 0.250 m. The five-bladed propeller has a right-handed direction of rotation. The skew of the propeller is moderate. Table 1 summarizes the main geometrical parameters of the PPTC propeller. A photograph of the propeller is shown in Figure 17.

Table 1. Main geometric parameters of the PPTC propeller.

Diameter	D	[m]	0.250
Pitch ratio at r/R= 0.7	$P_{0.7}/D$	[-]	1.635
Expanded area ratio	A_E/A_0	[-]	0.779
Chord length at r/R=0.7	$c_{0.7}/D$	[-]	0.417
Skew	Θ	[°]	18.837
Hub ratio	d_h/D	[-]	0.300
Number of blades	Z	[-]	5
Direction of rotation		[-]	Right handed
Type		[-]	CPP

The test procedure for the PPTC propeller included the determination of global performance curves in open water conditions. The tests were performed in a towing tank using the traditional approach in which the propeller is driven in a downstream configuration.

The test programme also included further tests in the cavitation tunnel. Laser Doppler Velocimetry (LDV) measurements were performed in the slipstream of the propeller to determine the location and strength of the propeller tip vortex and blade wake. The LDV measurements were performed in non-cavitating conditions. Furthermore, cavitation tests at varying propeller loads and cavitation numbers were performed, and the cavitation extent and global performance characteristics were recorded.

The propeller was driven in an upstream configuration in the cavitation tunnel. The cavitation tunnel has a square cross section with rounded edges. The test section width and height are both 0.600 m.

Figure 17. A photograph of the PPTC propeller. (Figure taken from Barkmann [2011].)

The propeller open water curves were calculated to validate the global performance predictions of the propeller. The global performance was calculated between the advance numbers $J = 0.6 \ldots 1.4$ with a step size $\Delta J = 0.2$.

The calculated propeller wake field was compared to a measured wake field in wetted conditions at a given loading point. The comparison was made at the planes normal to the axial direction located at $x/D = 0.1$ and 0.2 downstream from the propeller plane.

Finally, the simulated cavitation patterns at three operation points were compared to the observations. The velocity field behind the propeller was not measured in the cavitating conditions. The effect of cavitation on the velocities in the propeller tip vortices was investigated by comparing the numerical results in the wetted and cavitating conditions. The tests comprised three cavitation conditions: in the first case sheet cavitation together with a

strong tip vortex was observed; in the second case a detached tip vortex incepted; in the third case pressure side sheet cavitation existed.

The simulations of propeller wake field velocities and cavitation behaviour predictions were performed according to the thrust identity in the wetted conditions. Small discrepancies between the measured and predicted thrust and torque existed in the equal kinematic conditions. For this reason, the inflow velocity to the propeller was adjusted iteratively in the calculations to reach the thrust identity between the simulations and the measurements. Table 2 summarizes the flow conditions and the investigated phenomena of the tests.

Table 2. Flow conditions of the undisturbed inflow. Calculations performed in the cavitation tunnel (#2 and #3) according to the thrust identity.

	Test Description	J	$K_{T,wetted}$	n [rps]	σ_n
#1	Global performance in open water	0.6…1.4	–	15	–
#2	Velocities in the slipstream	(1.253)	0.250	23	–
#3.1	Cavitation patterns (suction side sheet and tip vortex cavitation)	(1.019)	0.387	25	2.024
#3.2	Cavitation patterns (tip vortex cavitation)	(1.269)	0.245	25	1.424
#3.3	Cavitation patterns (pressure side sheet cavitation)	(1.408)	0.167	25	2.000

3.2 Propeller in a wake field

The INSEAN E779A propeller was used for non-uniform inflow tests. The propeller is a model-sized fixed pitch propeller (FPP) with a diameter of 0.227 m. The four-bladed propeller has a right-handed direction of rotation and light skew. Table 3 summarizes the main geometrical parameters of the propeller.

An extensive test programme was conducted on the INSEAN E779A propeller, but only the wake field results are utilized here to validate the cavitation simulations in unsteady conditions. The wake field in the tests is created by mounting an artificial wake generator in front of the propeller as shown in Figure 18.The wake generator consists of five plates that are assembled parallel to the flow direction and joined together with 60 cylindrical bars. The width and the length of the plate array are 86 mm and 300 mm, respectively, and there is a 14 mm gap between the plates. The wake generator is mounted from the roof of the tunnel. The spacing between the bottom of the wake generator and the drive shaft is 2.5 mm. The wake generator is located so that the trailing edge of the wake generator is at x/R = -0.89 in front of the propeller plane. The wake from the plate array mimics that of a single-propeller vessel. The propeller is driven in an upstream configuration in the cavita-

tion tunnel. The cavitation tunnel has a square cross section with rounded edges in the observation region. The width and height of the test section are 0.600 m.

Table 3. Main geometric parameters of the INSEAN E779A propeller.

Diameter	D	[m]	0.227
Pitch ratio at r/R= 0.7	$P_{0.7}/D$	[-]	1.117
Expanded area ratio	A_E/A_0	[-]	0.689
Chord length at r/R=0.7	$c_{0.7}/D$	[-]	0.104
Skew	Θ	[°]	4.480
Hub ratio	d_h/D	[-]	0.200
Number of blades	Z	[-]	4
Direction of rotation		[-]	Right handed
Type		[-]	FPP

The propeller is tested in the wake field at a fixed inflow speed and propeller rate of rotation. The tunnel pressure is varied in the tests. One pressure level is adjusted in the numerical simulations. Table 4 shows the flow conditions used in the simulations.

The wake in the simulations was created by modelling the geometry of the wake generator in the calculation domain. The calculated total wake was compared to the measured wake between the propeller and the wake generator at x/R = -0.52.

Figure 18. The INSEAN E779A propeller and the wake generator mounted in the cavitation tunnel of CEIMM. (Photograph is courtesy of CNR-INSEAN.)

Table 4. Flow conditions for the propeller working in a wake field used for numerical simulations.

	Test description	V_∞ [m/s]	n [rps]	σ_n
#1	Cavitation patterns in the wake field	6.22	30.5	4.455

3.3 Computational meshes and boundary conditions

The local coordinate system (x,y,z) is the same in all calculations. The origin is located on the shaft line in the propeller plane. The x-axis is parallel to the axial direction pointing downstream; the z-axis is parallel to the blade generator line along the increasing radial direction; and the y-axis forms a right-handed coordinate system with the other axes. The local coordinate system rotates with the propeller. The tangential velocity is thus negative in the propeller rotational direction Θ_{prop}.

A fixed global coordinate system (X,Y,Z) is introduced in the analyses of the propeller working in a wake field. The origin is located at the same point as that of the local coordinate system. The X-axis is also the same as with the local coordinate system; the Z-axis points to the roof of the cavitation tunnel; and the Y-axis forms a right-handed coordinate system with the other axes.

3.3.1 Propeller in a uniform inflow

The PPTC propeller geometry is provided by SVA Potsdam in the Initial Graphics Exchange Specification (IGES) format and is available online (http://www.sva-potsdam.de/pptc.html). The surface grid of the blades, hub, cap, and shaft are modelled according to the geometry IGES file.

The calculation domain in the open water calculations is one fifth of a full cylinder in the circumferential direction due to the symmetry of the five-bladed propeller. The inlet is located five propeller diameters upstream from the propeller plane. The outlet is located ten propeller diameters downstream from the propeller plane. The domain extends four propeller diameters in the radial direction. The size of the calculation domain is large so that the effects of the domain boundaries are negligible.

The blades, hub and cap are modelled as no-slip rotating surfaces. The axis is modelled as a no-slip stationary surface. A velocity boundary condition is applied at the inlet, and a pressure boundary condition is used at the outlet. The outer side of the domain has a free stream velocity boundary condition. At the longitudinal sides of the domain a cyclic boundary condition is applied.

In the analyses performed inside the cavitation tunnel the propeller is driven in an upstream configuration. The grid near the propeller is the same in the open water and tunnel analyses. The geometry of the cap and the shaft in the tunnel analyses are done according to the IGES-geometry file.

The square tunnel cross section is simplified to be circular in the analyses. The circular cross section allows the use of a quasi-steady approach due to the symmetry of the prob-

lem. The tunnel radius is R_{tun} = 0.3385 m, which gives the same cross-sectional area as the actual tunnel.

The distances of the inlet and the outlet from the propeller plane are the same in the simulations performed in the tunnel as in the open water simulations. The same boundary conditions are also used, but the tunnel roof is modelled as a slip solid surface. Figure 19 shows the computational domain of the simulations performed in the cavitation tunnel. The calculations are performed at three grid levels in wetted and cavitating conditions.

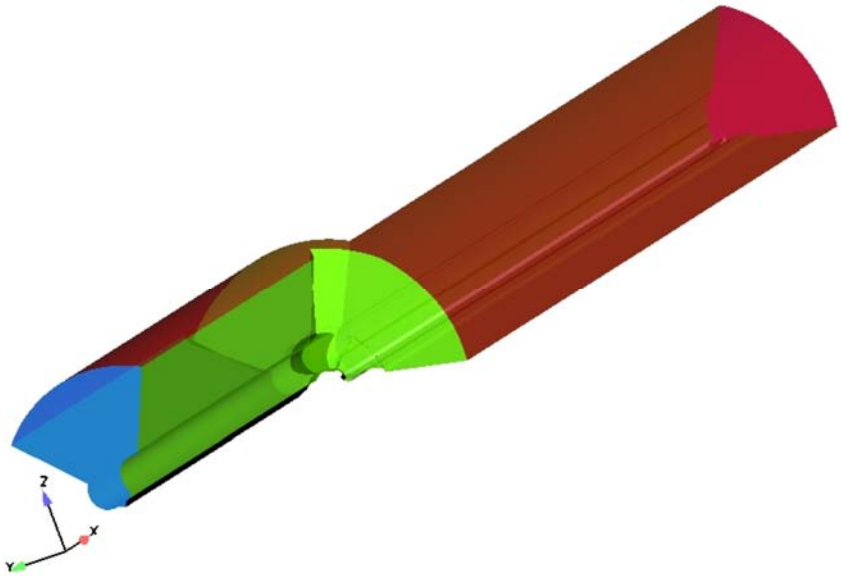

Figure 19. Calculation domain for the PPTC propeller analyses in the cavitation tunnel. The propeller and shaft are shown as black surfaces. The inlet is the blue face on the left and the outlet is the purple face on the right. The cyclic sides of the domain are green. The idealized cylindrical wall of the tunnel is the red face on top of the domain.

The grid has an O-O topology around the propeller blades. The blocks in the exterior of the propeller have an H-H topology. A butterfly-type topology is applied behind the cap to prevent a singularity in the grid. The finest grid level consists of a total of 4.3 million cells in 18 blocks. The second and the third level grids consist of 534,000 and 67,000 cells, respectively. On the blade surface the finest grid level consists of 144 cells in the chord-wise direction and 104 cells in the spanwise direction.

The grid resolution around the blade leading edge is high. A strong pressure peak is present at the leading edge of the blade and a high resolution grid is needed to solve the peak pressure reasonably. At the finest grid level there are about 30 cells around the blade's leading edge radius. Due to the O-O topology, the same resolution is applied also around the blade tip and the trailing edge. The grid is heavily clustered towards the viscous surfaces. The non-dimensional wall distance y^+ is close to unity at the finest grid level. Table 5 gives a summary of the grid size details for the three grid levels. Figure 20 shows

the grid at three grid levels on the blade surface and around the leading edge of the blade at a constant grid index at a radius of about $r/R = 0.7$.

The dissipation of the velocity and pressure gradients in the slipstream of the propeller presents an additional challenge for the simulations. The grid resolution must be high in the regions of the tip vortices and the wakes from the blade. Heavy numerical dissipation ruins the solution of the flow details if a proper grid density is not present in the regions of interest. The accuracy of the tip vortex and blade wake modelling has only a marginal effect on the propeller global performance predictions. Consequently, the propeller wake field does not need to be accurately modelled if information on propeller global performance characteristics is only needed.

At present it is not possible to fill the whole slipstream of the propeller with a very dense grid due to computing power limitations. The cells must be focused at the tip vortex and blade wake regions. The exact locations and shapes of the tip vortices and the blade wakes are not known before the calculations are started. For this reason, the grid must be created iteratively in the slipstream. The location of the tip vortex and the blade wake is searched from the initial grid. The grid in the slipstream is then adjusted to follow the pitch and contraction of the propeller wake.

The topology of the structured grid in the slipstream becomes helical as shown in Figure 22. The grid resolution in the cross-section of the tip vortex is about 20 x 20 cells at the finest grid level. The grid resolution at three levels around the tip vortex is shown in Figure 21. At the cross section of the blade wake the number of cells is about ten at the finest grid level.

Table 5. Summary of grid size details at the three grid levels for the propeller in a uniform inflow case. The numbers of the surface cells are given on one side of the blade.

	Fine grid	Medium grid	Coarse grid
Total number of cells	4 269 568	533 696	66 712
Surface cells in the chordwise direction	144	72	36
Surface cells in the spanwise direction	104	52	26
Cells around the blade leading edge radius	30	15	8
Cells in the cross-section of the tip vortex	20 × 20	10 × 10	5 × 5
Cells across the blade wake	10	5	3

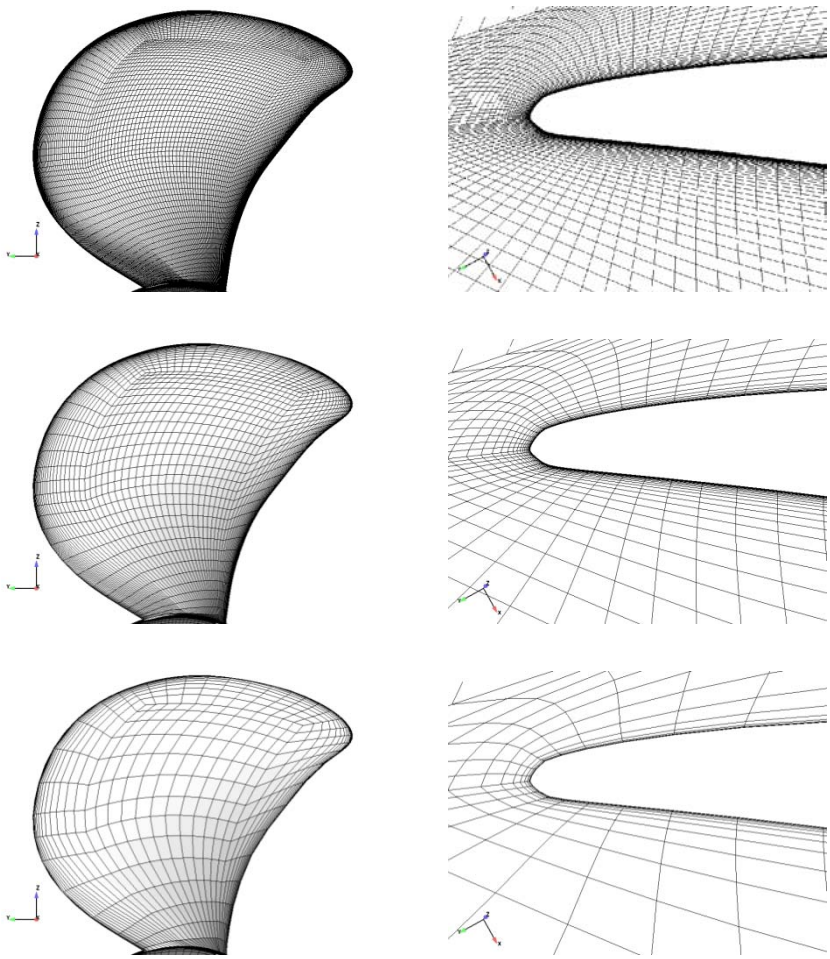

Figure 20. Grid resolution at three grid levels. In the left column: the surface grid on the blade. In the right column: the grid near the leading edge of the blade at a constant grid index at a radius of $r/R = 0.7$. From top to bottom: first-level fine grid, second-level medium grid, and third-level coarse grid.

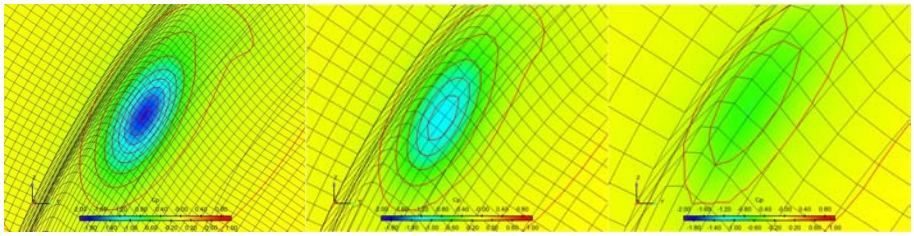

Figure 21. Grid resolution at the tip vortex location at x/D = 0.2 in a wetted flow. From left to right: fine, medium, and coarse grids. The background colour is the pressure distribution in Case 2 conditions.

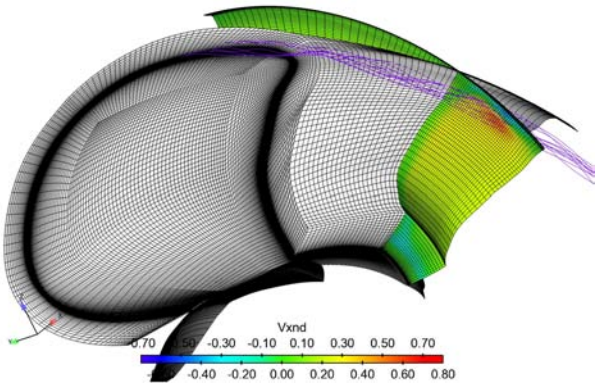

Figure 22. Surface grid on the blade and a slice of the grid in the slipstream, which has been adjusted to follow the wake of the blade. The colour on the axial grid slice is the axial velocity. The streamlines in the tip vortex are also shown.

3.3.2 Propeller in a wake field

The geometry of the INSEAN E779A propeller is provided by CNR-INSEAN as a traditional propeller drawing and also in IGES format. The surface grid of the blades, hub, cap and shaft are modelled according to the geometry in the IGES file. The geometry of the cavitation tunnel in the simulations mimics that of the test section in the CEIMM cavitation tunnel. The geometry of the wake generator is created according to the technical drawing provided by CNR-INSEAN.

The blades, hub and cap are modelled as no-slip rotating surfaces. The axis is modelled as a no-slip stationary surface. The plates and bars of the wake generator are modelled as no-slip surfaces. The walls of the tunnel are slip solid surfaces to reduce the total number of cells in the domain. A velocity boundary condition is applied at the inlet, and a pressure boundary condition is used at the outlet.

The computational domain has the same size and shape as the test section of the cavitation tunnel. The length of the domain is 2.6 m and the height and width of the domain are 0.6 m. The propeller is located in the middle of the tunnel. As the problem is not symmetrical, the complete tunnel must be modelled. The solution is unsteady and solved using the time-accurate approach.

A part of the domain rotates at the rotational speed of the propeller. The upstream location of the rotating domain is in the middle of the trailing edge of the wake generator and the propeller plane. The rotating domain extends to the outlet in the axial direction. In the radial direction the rotating domain extends to about the half way between the propeller tip and the tunnel roof. The rest of the domain is stationary. The sliding mesh boundary condition is applied at the interface of the rotating and stationary domains. Figure 23 shows the calculation domain used in the simulation.

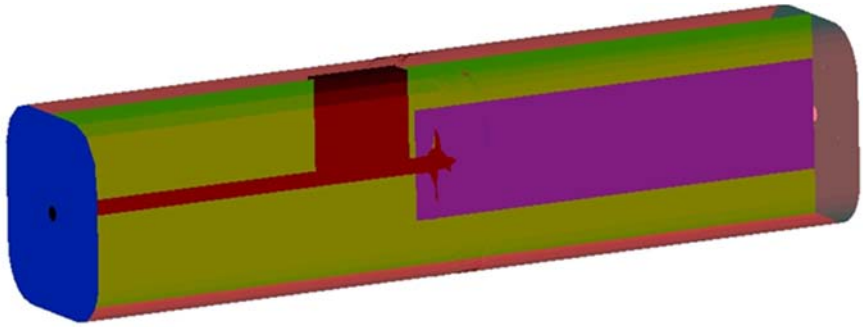

Figure 23. The computational domain of the INSEAN E779A propeller behind the wake generator in the cavitation tunnel. The propeller, shaft and wake generator are visualized in black. The inlet is depicted by the blue colour on the left. The outlet is the grey surface on the right. The green and purple colours show the stationary and rotating parts of the domain, respectively.

The grid has an O-O topology around the propeller blades and the wake generator. The blocks in the exterior of the propeller have an H-H topology. A butterfly-type topology is applied behind the cap of the propeller axis. At the finest level grid the total number of cells is about 10.6 million in 132 blocks. At the second level medium grid the number of cells is 1.3 million. The wake generator itself consists of about 2.3 million cells at the finest grid level in 90 blocks.

The grid resolution on the blades is similar to that of the PPTC propeller. The number of cells in the finest grid level on one side of the blade in the chordwise direction is 144 and in the spanwise direction 104. The leading edge radius is covered by 20 cells at the finest grid level. The grid is made dense towards the viscous surfaces so that the non-dimensional distance y^+ is close to unity at the finest grid level. Table 6 summarises the grid size details. Due to the very high computational costs of the time-accurate method, the calculations are performed only in the second level medium grid.

Accurate modelling of the tip vortex and the blade wake was of less interest in this case. The dynamic behaviour of the sheet cavity in altering inflow conditions was given

more focus. The propeller wake region is modelled with a coarser grid compared to that used in the PPTC propeller case. Figure 24 shows the surface grid on the propeller and the wake generator at the finest level grid. Figure 25 shows the grid on a developed cylindrical surface near the propeller plane and the wake generator's trailing edge at a radius of r/R =0.53. It can be seen that the grid follows the wakes of the blades some distance downstream from the propeller. Then the topology turns to the axial direction. The sliding mesh interface is also shown in the figure.

Table 6. Summary of the grid size details of the two grid levels of the propeller in a wake field case. The numbers of the surface cells are given at one side of the blade.

	Fine grid	Medium grid
Total number of cells	10 635 072	1 329 384
Surface cells on a blade in the chordwise direction	144	72
Surface cells on a blade in the spanwise direction	104	52
Cells around the blade leading edge radius	20	10

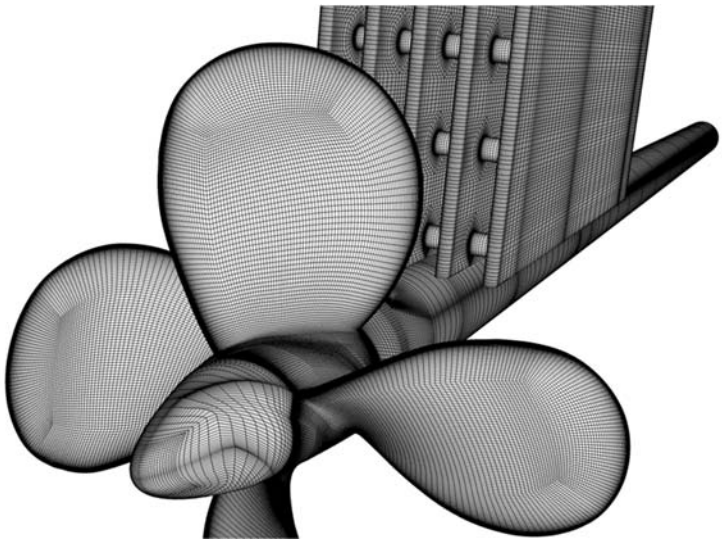

Figure 24. Surface grid at the finest grid level on the propeller, shaft, and wake generator. The inflow to the propeller comes through the wake generator.

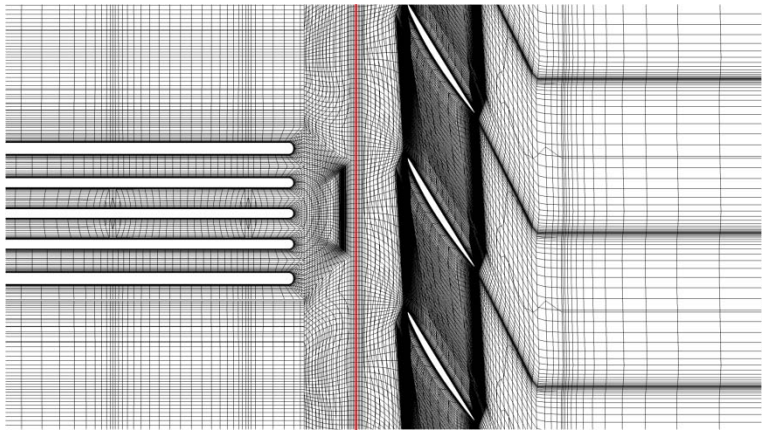

Figure 25. The grid on a developed cylindrical surface of radius r/R = 0.53. The view is focused near the trailing edge of the wake generator and the propeller plane. The sliding mesh interface is highlighted in red. The flow is from left to right. The whole circumference of the grid is not shown.

3.4 Computer programs and computational arrangements

Pre-processing of the present simulations was performed by VTT's in-house program Plot3d. To visualize the created grids, the commercial IGG program was used. The RANS equations were solved with the FINFLO code. The convergence histories were investigated using the Guiconvergence program delivered with FINFLO. Post-processing was performed by the commercial program Ensight.

The CFD calculations were performed using two Intel Xeon X5650 2.66 GHz six-core processors in parallel. The computer system used was a Dell Precision T5500 64-bit with Windows 7 operating system.

The wall clock time for the quasi-steady calculations of the propeller in the uniform inflow was about 48 hours per case. The time-accurate calculations for the propeller working in the wake field were about five days at the second-level medium grid. An estimated wall-clock time for the calculations in the first-level fine grid is about one month with the same computational arrangement.

4. Results

The same non-dimensional quantities were applied to both the uniform inflow case and the propeller in wake field case. The propeller advance number J was defined as:

$$J = \frac{V_A}{nD} \tag{144}$$

The propeller thrust T and torque Q were non-dimensionalized as is usual in the propeller field as:

$$K_T = \frac{T}{\rho n^2 D^4} \tag{145}$$

and

$$K_Q = \frac{Q}{\rho n^2 D^5} \tag{146}$$

The propeller open water efficiency is calculated from

$$\eta_O = \frac{J}{2\pi}\frac{K_T}{K_Q} \tag{147}$$

The pressure coefficient was determined here by using the rotational speed of the propeller as:

$$C_p = \frac{p - p_\infty}{\frac{1}{2}\rho_w (nD)^2} \tag{148}$$

where ρ_w refers to the density of water. The cavitation number is defined in a similar fashion:

$$\sigma_n = \frac{p_\infty - p_v}{\frac{1}{2}\rho_w (nD)^2} \tag{149}$$

The sectional pressure distribution is non-dimensionalized as:

$$c_p = \frac{p - p_\infty}{\frac{1}{2}\rho_w (V_A^2 + (2\pi nr)^2)} \tag{150}$$

The velocities are non-dimensionalized by the inflow velocity and the turbulent viscosity by the dynamic viscosity.

4.1 Propeller in uniform inflow

The results of the propeller in the uniform inflow conditions consists the numerical predictions of the global performance characteristics of the propeller, the velocity fields in the propeller slipstream in the wetted and cavitating conditions, and the cavitation patterns around the propeller. The convergences of the calculations are investigated and the results are validated against the model test result.

4.1.1 Convergence

All simulations performed in the uniform inflow conditions were calculated with the same numerical methods and parameters. The Courant number in the simulations was *CFL* = 0.25. The under-relaxation factor for the pressure was α_p = 0.01 and for the velocity α_u = 0.5. A third-order upwind-biased scheme was utilized for the discretization of the convection terms, while a second-order central-difference scheme was used for discretization of the diffusion terms. All simulations were performed with Chien's low Reynolds number *k-ε* turbulence model.

The convergence histories of the L_2-norms of the pressure correction and *x*-momentum residuals, and the total drag of the wetted and cavitating flow calculations are shown in

Figure 26. The convergence histories are given in Case 3.1. The flow conditions in Case 3.1 are described in Table 2. The convergence histories at the three investigated grid levels are also presented. The convergence histories for the other cases are similar to the presented cases.

In the cavitating flow simulations no algebraic multigrid methods were used. In the wetted flow solutions the algebraic multigrid was used at the medium grid level and at the finest grid level in the first 5,000 iterations. Thereafter the multigrid was no longer used. In the cavitating condition, where the multigrid method is not used, the residuals are higher at the coarser grid levels. In the wetted flow simulation the residuals at the medium grid level are higher than at the coarsest grid level due to the multigrid method.

The calculation of wetted flow converged faster at the coarse grid level than the cavitating flow simulation. The wetted flow converged after about 10,000 iterations at the coarsest grid level, whereas the cavitating flow converged after 20,000 iterations. The calculations were continued for 30,000 iterations at the coarse grid level to ensure convergence. At the second-level grid, the wetted flow converged after about 2,000 iterations, while the cavitating flow converged after about 15,000 iterations. The calculations were continued for 20,000 iterations at the medium grid level. At the finest grid level the wetted flow converged after about 2,000 iterations. When the multigrid method was switched off at 5,000 iterations, the convergence was re-attained at 30,000 iterations with an order of magnitude lower residual level. The multigrid method also has minimal influence on the total drag. The cavitating flow simulation converged after about 10,000 iterations at the finest grid level. The calculations were continued for 30,000 iterations at the finest grid level.

The L_2-norm of the residuals of the pressure correction is two orders of magnitude lower in the wetted flow calculations than in the cavitating flow calculations. The pressure correction residuals were nevertheless at a low level also in the cavitating flow calculations. The L_2-norm of the x-momentum residuals was about the same in the wetted and cavitating flow calculations. The drag convergence history was smooth in the wetted and cavitating flow simulations.

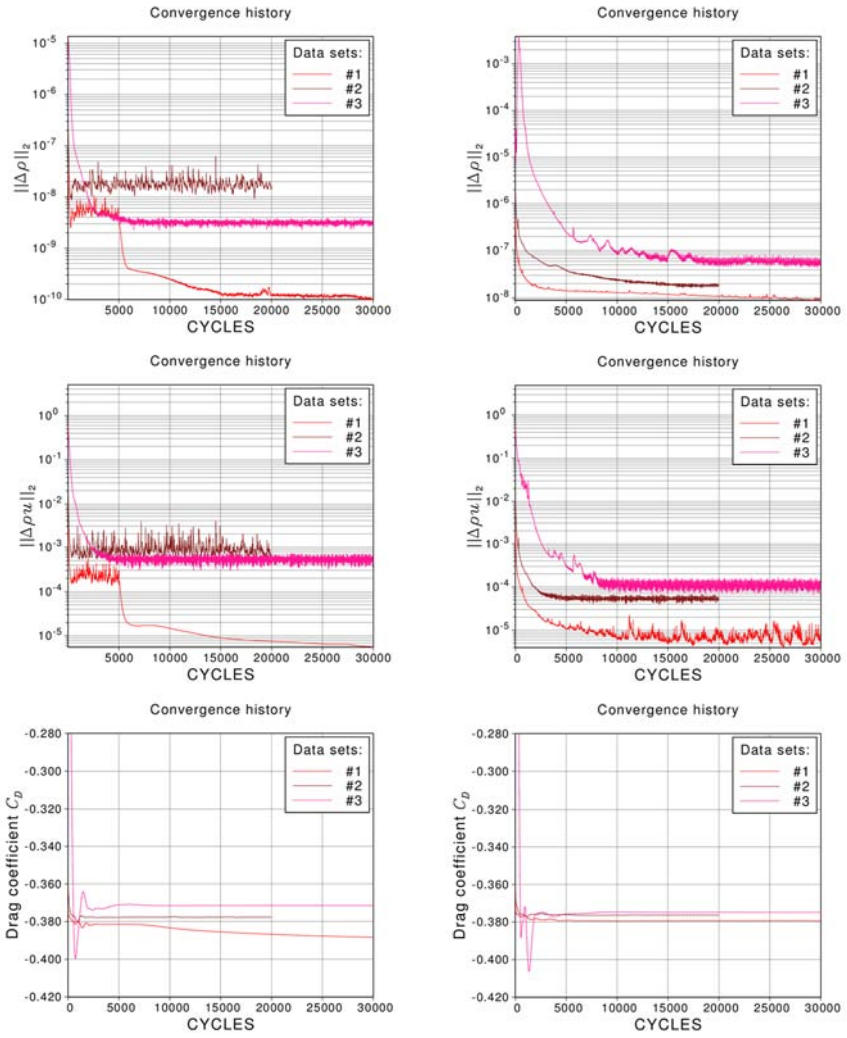

Figure 26. Convergence histories of the L_2-norm of the pressure correction and x-momentum residuals, and the total drag of the simulation for the propeller in the cavitation tunnel in Case 3.1 conditions. The figures top to bottom on the left show the convergence histories of the wetted flow simulations. The figures top to bottom on the right show the convergence histories of the cavitating flow simulations. The convergence histories at the fine, medium, and coarse grid levels are depicted by #1, #2, and #3, respectively.

4.1.2 Global performance

Table 7 shows a comparison between the measured and calculated thrust, torque, and efficiency of the propeller at the three investigated grid levels at J = 1.0 in non-cavitating

open water conditions. The performance characteristics are given for the propeller blades only. The influence of the propeller hub and cap are subtracted from the open water results both in the measurements and in the calculations. As the table shows, the calculated thrust and torque are 1% lower and 1.5% higher at the finest grid level, respectively, compared to the measured values. The calculated efficiency is 2.4% lower than in the measurements. Figure 27 reveals that the good agreement between the measurements and the calculations are maintained over the whole investigated range of open water curves.

Table 7. Global performance characteristics of the PPTC propeller in non-cavitating open water conditions at $J = 1.0$ calculated with three grid resolutions. The relative differences of the calculated figures compared to measured figures are also shown. Measured figures provided by SVA Potsdam.

	K_T	ΔK_T [%]	10 K_Q	ΔK_Q [%]	η_O	$\Delta \eta_O$ [%]
Coarse grid	0.375	-3.7	0.972	+0.7	0.609	-4.4
Medium grid	0.383	-1.7	0.986	+1.2	0.619	-2.9
Fine grid	0.386	-1.0	0.989	+1.5	0.622	-2.4
Measurements	0.390	–	0.975	–	0.637	–

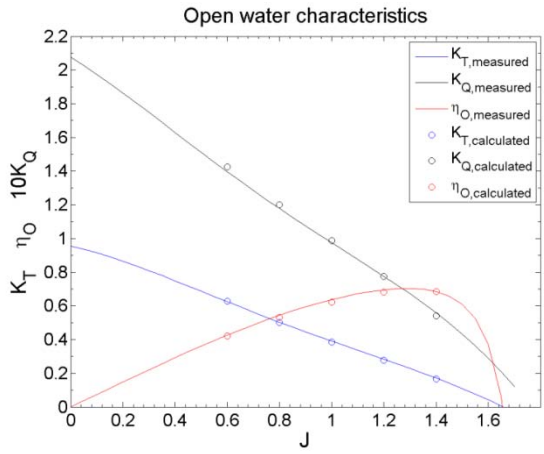

Figure 27. Polynomial fits of the measured open water curves and the calculated figures from the finest grid level in non-cavitating conditions. Measured data provided by SVA Potsdam.

The error estimate for global thrust and torque was made according to the Richardson's extrapolation method, see also Mikkola (2009). For a general integral variable ϕ the error on a grid level $i > 1$ is defined as:

$$err_i(\phi) = |\phi_i - \phi_1| \tag{151}$$

where $\phi_1$is the intergral variable's value on the finest grid level.

The order of accuracy is evaluated from the one-term error estimation:

$$err_i(\phi) = a\Delta\tilde{x}^p \tag{152}$$

where $\Delta\tilde{x}$ is a general measure of discretization, p is the order of accuracy, and a is a constant. The inverse of the cubic root of the number of elements N_i was used as the discretization measure. The parameters a and p were obtained by fitting the function to the numerical results. By solving the parameter p from the above equation it follows that for $i > 1$:

$$p^{\phi} = \frac{\ln err(\phi_{i-1}) - \ln err(\phi_i)}{\ln\left(\sqrt[3]{N_{i-1}}\right) - \ln\left(\sqrt[3]{N_i}\right)} \tag{153}$$

The error estimates of the thrust and torque on the second and third grid levels with respect to the finest grid results are shown in Figure 28. As the figure shows, the slope of the curves connecting the error estimates, i.e. the order of accuracy of the thrust and torque are p^{thrust} =1.9 and p^{torque} =2.5, respectively.

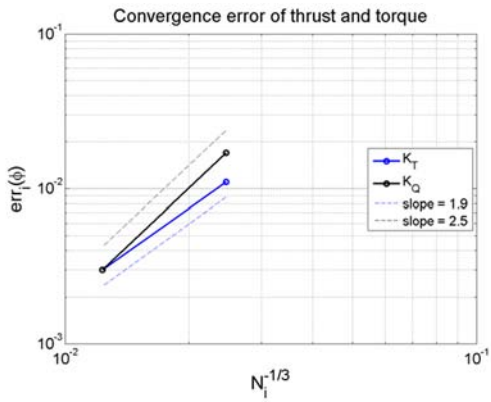

Figure 28. The thrust and torque convergence errors. The slopes of 1.9 and 2.5 are also shown.

Extrapolation of the simulated thrust and torque to the infinitely dense grid result was performed using the generalized Richardson's extrapolation method described in the ITTC guidelines (ITTC, 2008). The error estimate $\delta^{*(1)}_{RE_{i,1}}$ is calculated using the equation:

$$\delta^*_{RE_{i,1}} = \frac{err_i(\phi)}{r_i^{p\phi} - 1} \tag{154}$$

where r_i is the refinement ratio of the grid, i.e. $r_i = \Delta\tilde{x}_{i-1}/\Delta\tilde{x}_i$. The ITTC (2008) recommends that a multiplicative correction factor is used to take into account the effects of higher-order terms, and for the estimation of errors and uncertainties. The error is then defined as:

$$\delta^*_{i,1} = C_i \delta^*_{RE_{i,1}} \tag{155}$$

where the correction factor C_i is calculated as:

$$C_i = \frac{r_i^{p_i} - 1}{r_i^{p_{i,est}} - 1} \tag{156}$$

The parameter $p_{i,\mathrm{est}}$ is an estimate for the limiting order of accuracy of the simulation as the spacing goes to zero and the asymptotic range is reached so that $C_i \rightarrow 0$. Here an estimation of $p_{i,est} = 2$ is utilized. The extrapolated result at the infinite dense grid is calculated by $S_{C,\phi} = S_1 - \delta^*_{i,1}$, where S_1 is the simulation result at the finest grid level.

The uncertainty U_i of the error $\delta^*_{i,1}$ is calculated by the formula

$$U_i = (2|1 - C_i| + 1)\left|\delta^*_{RE_{i,1}}\right| \tag{157}$$

The outcome of the error estimation is summarized in Table 8. The figures presented in Table 7 were used to define the uncertainty analyses. It is seen that the estimated thrust and torque at an infinitely dense grid differ from the values predicted at the finest grid level by 1.5 and 0.6%, respectively. The uncertainties of those integral values are 1.7 and 0.7%, respectively.

Table 8. Verification of the predicted integral variables in the simulations.

ϕ	p	$\delta^*_{RE_{i,1}}$	C_i	$\delta^*_{i,1}$ [%]	U_i [%]	S_C
K_T	1.9	-0.0060	0.9565	-1.5	1.7	0.3918
10 K_Q	2.5	-0.0050	1.1556	-0.6	0.7	0.9948

The validation of the simulated integral values was also made according to the recommended procedure of the ITTC (ITTC, 2008). The error E between the measured D and simulated $S = S_i$ values is defined as:

$$E = D - S \tag{158}$$

The uncertainty of the validation is defined as:

$$U_V = \sqrt{U_{SN}^2 + U_D^2} \tag{159}$$

where U_{SN} and U_D are the uncertainties related to the numerical simulation and the measurements, respectively. In the present case, the experimental uncertainty is not known. The experimental uncertainty was therefore approximated to be U_D/D = 2%. The iterative unsteadiness U_I was found to be very small at all grid levels (less than 0.1%), thus the ambiguity related to the numerical simulation U_{SN} was estimated to consist only the grid convergence part U_G, i.e. $U_{SN} = U_I + U_G = U_G$. The uncertainty related to the grid convergence is calculated as:

$$U_G = \left|C_i \delta^*_{RE_{i,1}}\right| + \left|(1 - C_i)\delta^*_{RE_{i,1}}\right| \tag{160}$$

In this case $C_i = C_G$ since the iterative unsteadiness was assumed to be negligible.

The validation study can also be performed with the corrected values for the infinitely dense grid. The error E_C between measured and corrected simulated values are determined as:

$$E_C = D - S_C \tag{161}$$

The validation uncertainty U_{V_C} is calculated from:

$$U_{V_C} = \sqrt{U_{S_CN}^2 + U_D^2} \tag{162}$$

where $U_{S_CN} = U_{G_C}$. The uncertainty related to the corrected grid convergence is calculated from:

$$U_{G_C} = \left|(1 - C_G)\delta^*_{RE_{i,1}}\right|. \tag{163}$$

Table 9 summarizes the results of the validation activities performed with the values of the integral variables given in Table 7. The validation at the finest grid level and at the infinitely dense grid is given in the table. As the table shows, in all cases the validation uncertainty is higher than the discrepancy between the measured and simulated figures. Thus, validation has been achieved for the global performance characteristics from the programmatic standpoint.

Table 9. Validation of the predicted integral variables in the simulations.

ϕ	E [%]	U_V [%]	U_D [%]	U_{SN} [%]
K_T	+1.0	2.1	2.0	0.6
$K_{T,C}$	-0.5	2.0	2.0	<0.1
10 K_Q	-1.4	2.1	2.0	0.7
10 $K_{Q,C}$	-2.0	2.0	2.0	<0.1

4.1.3 Propeller wake field

To validate the simulation results of the propeller wake field, the numerical results were compared to the LDV measurements performed in the cavitation tunnel in wetted conditions. The comparison between the LDV measurements and the simulation results was conducted on two planes located at x/D = 0.1 and x/D = 0.2 downstream from the propeller plane. The plane normals were parallel to the axial direction. The first plane was located very close to the trailing edge of the propeller. The second plane was located some distance downstream from the propeller. Figure 29 shows the locations of the measurement planes.

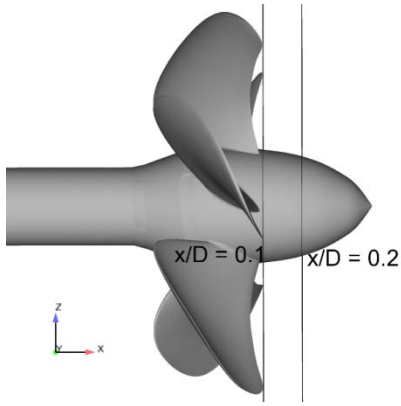

Figure 29. The locations of the wake measurement planes in the slipstream of the propeller.

The calculations were made according to the thrust identity with the measurements. The advance speed in the calculations was iteratively adjusted so that the thrust in the calculations matched the measured thrust. The outcome of the iteration process is shown in Table 10. As can be seen, the advance coefficient in the simulations is about 1.8% lower than in the measurements.

Table 10. The global parameters used in the propeller wake field simulation case compared to the values used in the measurements. The simulated figures are taken from the finest grid level. The measured figures are provided by SVA Potsdam.

Case 2	K_T	ΔK_T [%]	J	ΔJ [%]	10 K_Q	ΔK_Q [%]	η_O	$\Delta \eta_O$ [%]
Simulation	0.250	-0.3	1.253	-1.8	0.725	0.0	0.689	-2.2
Measurements	0.251	–	1.275	–	0.725	–	0.704	–

Figure 30 shows the axial component of the propeller wake field at $x/D = 0.1$ behind the propeller plane. The figure is focused on the tip vortex and the wake of the blade at the 12 o'clock position. The raw data of the LDV measurements and the RANS solution at the finest grid level are given in the figure. The spatial resolution applied in the LDV measurements is also shown. The resolution is 0.25 degrees in the circumferential direction. The radial resolution varies, being at its finest in the vicinity of the tip vortex.

It can be seen from Figure 30 that the tip vortex location is slightly lower in the simulations than in the measurements. The reason for this is not exactly known. It is, however, difficult to fully control the wake field of a propeller in experimental conditions, and there may have been a small inclined velocity component in the main flow in the tunnel. The propeller wake field may have been influenced slightly by this factor.

To be able to compare the strength of the measured and simulated tip vortices, the circumferential distributions of the wake components were plotted at constant radii at the two measurement planes. The radii of the comparison sections were chosen so that they match

the maximum and minimum axial wake location in the tests and in the simulations. The corresponding radii at $x/D = 0.1$ were $r/R = 0.995$ and $r/R = 0.973$ in the tests, and in the simulations $r/R = 0.995$ and $r/R = 0.963$. In addition, the measured and simulated strengths of the blade wake were compared at a radius of $r/R = 0.7$. Figure 31 shows the wake components at the investigated radii at $x/D = 0.1$ over one cyclic section of the whole circumference of the domain.

As can be seen, the shape of the tip vortex and the blade wake are relatively similar in the measurements and in the simulations. The tip vortex and the wake of the blade are, however, somewhat stronger in the simulations compared to the measurements. The distance between the maximum and minimum axial velocities in the simulations is slightly higher than in the measurements. The sharp peaks in the wake components are caused by the wake of the blade. These peaks are stronger in the simulations than in the measurements.

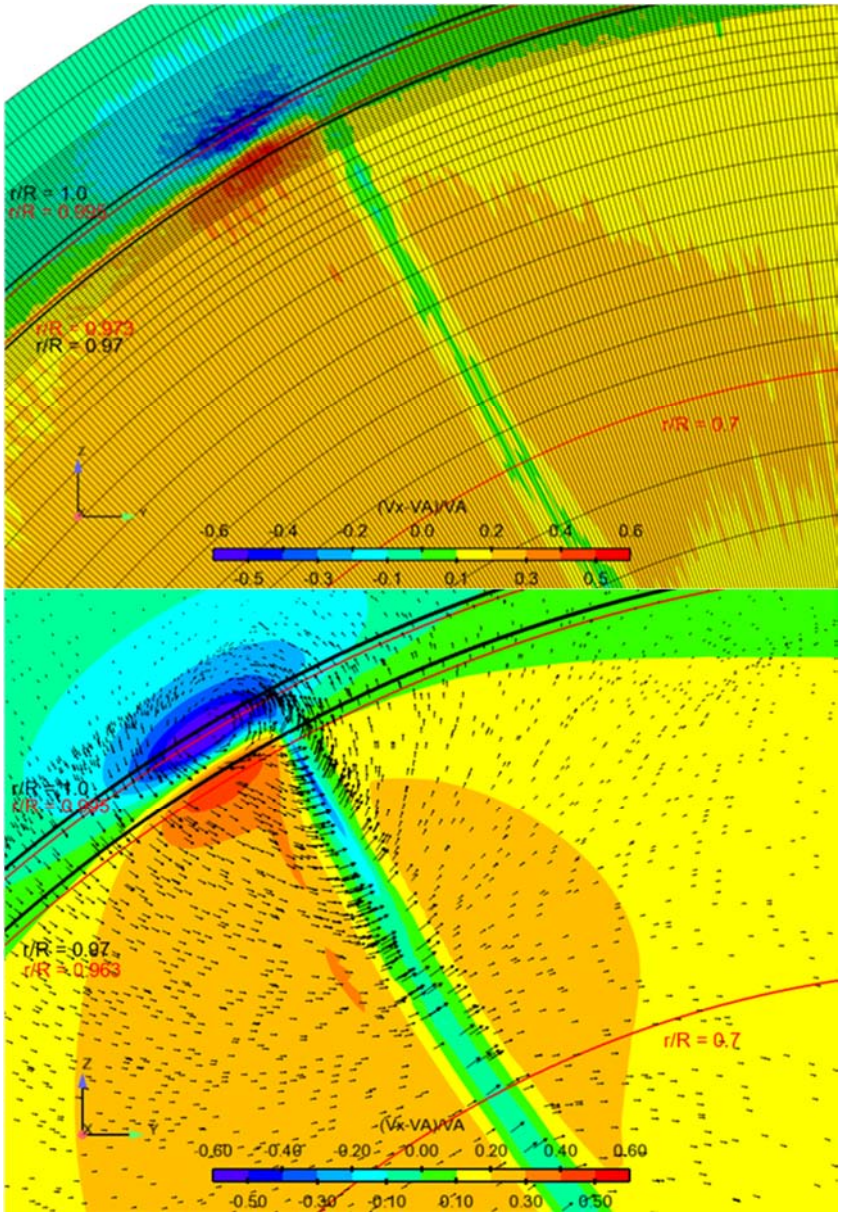

Figure 30. The axial wake at a plane normal to the axial direction at $x/D = 0.1$. The upper figure shows the outcome of the LDV measurements together with the spatial resolution of the measurements. The lower figure shows the RANS analysis result for the finest grid level with the projected velocity vectors. The red radii depict the reference radii at the minimum and maximum axial wake locations, and the radius $r/R = 0.7$. The black radii at $r/R = 1.0$ and 0.97 are given for reference. Measured data provided by SVA Potsdam.

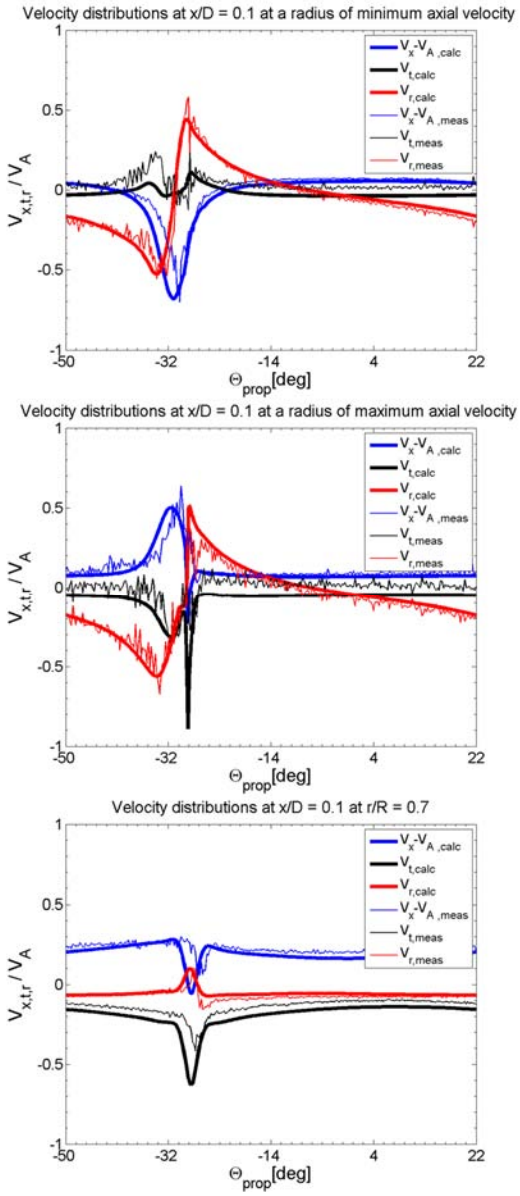

Figure 31. The axial, tangential, and radial wakes over a circumferential period of the wake at constant radii at $x/D = 0.1$. The thick lines are the RANS predictions at the finest grid level. The thin lines are the results of the LDV measurements. At the top: the radius of the minimum axial wake; in the middle: the radius of the maximum axial wake; at the bottom: the radius of $r/R = 0.7$. Measured data provided by SVA Potsdam.

Figure 32 shows the axial component of the propeller wake at $x/D = 0.2$ behind the propeller plane. The tip vortex and the blade wake shown in this figure are from the preceding blade of the one at the 12 o'clock position.

The circumferential distribution of the wake components were again compared at the radii of the minimum and maximum axial wake locations in the tip vortex, and at the radius $r/R = 0.7$. The minimum and maximum wake locations were at $r/R = 0.988$ and $r/R = 0.966$, respectively, in the measurements. In the calculations, the corresponding radii were at $r/R = 0.973$ and $r/R = 0.930$. Figure 33 shows the circumferential distributions of the wake components at the investigated radii. The distribution is given for one cyclic period of the whole wake field.

The tip vortex and the blade wake had higher velocities in the simulations than in the measurements at $x/D = 0.2$. The tip vortex was wider in the simulations than in the measurements. The roll-up of the blade wake into the tip vortex was evident from both the measurements and the simulations. The locations of the tip vortex and the blade wake were close to each other in the tests and the simulations. The blade wake near the tip vortex was seen clearer in the simulations than in the measurements.

To gain an impression of the grid convergence of the simulation results, the velocity field calculated with the three grid resolutions are compared in Figure 34. The wake components at $x/D = 0.2$ at the maximum axial velocity radius are shown at the three different grid resolutions. It can be seen that the coarse grid cannot solve the strength and the details of the propeller tip vortex. The medium grid solves the details of the tip vortex, but the magnitude of the tip vortex differs somewhat from the fine grid result. The location of the tip vortex is the same at all grid resolutions.

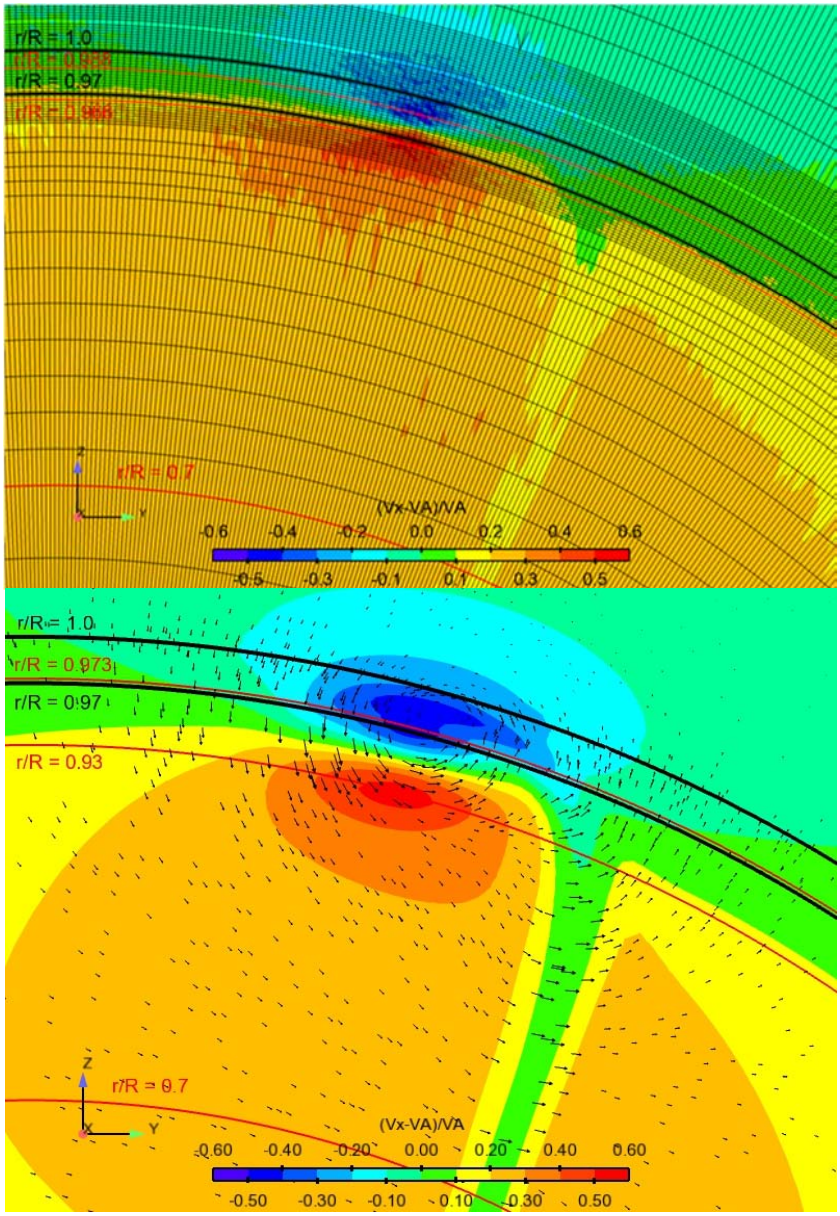

Figure 32. The axial wake at a plane normal to the axial direction at $x/D = 0.2$. The upper figure shows the outcome of the LDV measurements together with the spatial resolution of the measurements. The lower figure shows the RANS analysis result for the finest grid level with the projected velocity vectors. The red radii depict the reference radii at the minimum and maximum axial wake locations, and the radius $r/R = 0.7$. The black radii at $r/R = 1.0$ and 0.97 are given for reference. Measured data provided by SVA Potsdam.

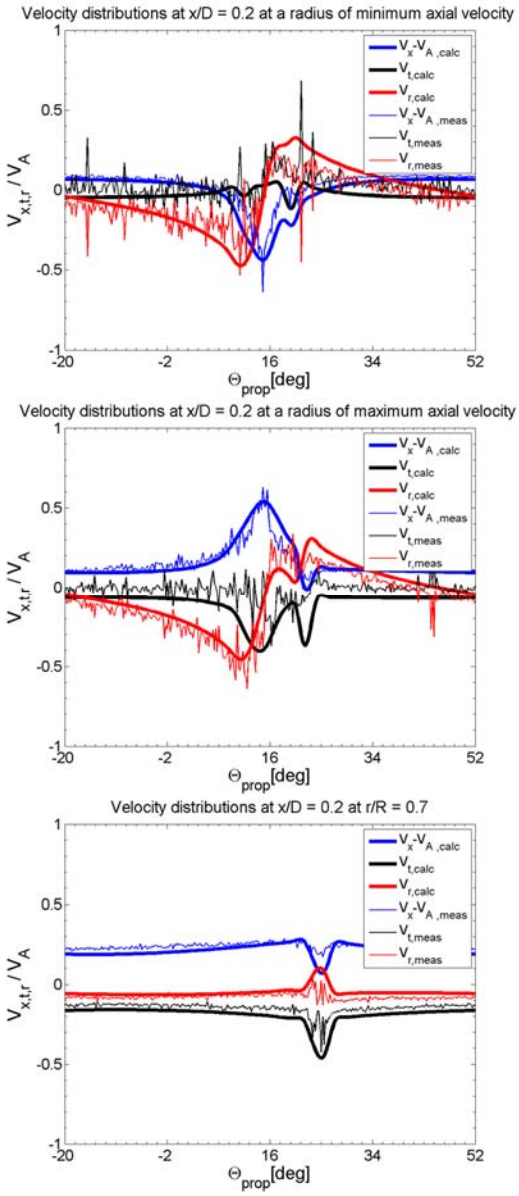

Figure 33. The axial, tangential and radial wakes over a circumferential period of the wake at constant radii at $x/D = 0.2$. The thick lines are the RANS predictions for the finest grid level. The thin lines are the LDV measurements. At the top: the radius of the minimum axial wake; in the middle: the radius of the maximum axial wake; at the bottom: the radius $r/R = 0.7$. Measured data provided by SVA Potsdam.

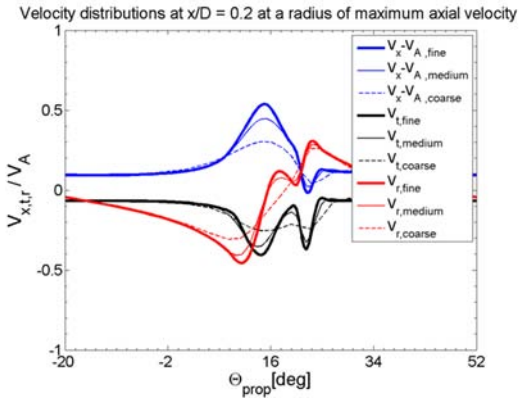

Figure 34. The axial, tangential, and radial wake components over a circumferential period of the wake at a radius of the maximum axial velocity at x/D = 0.2. The results are shown from the three grid resolutions. The thick solid, thin solid, and thin dashed lines represent the results of the fine, medium, and coarse grids, respectively.

4.1.4 Cavitation patterns

To validate the simulation results of the cavitating PPTC propeller, a comparison of the cavitation extent in the experiments and in the simulations was made at three different flow conditions. In one of the conditions a strong cavitating tip vortex was present. This case is studied in more detail.

The cavitation tests were conducted according to the thrust identity in wetted conditions. The inflow velocity was iteratively adjusted in the simulations to ensure that the propeller thrust in the simulations is the same as in the tests. The propeller thrust in the cavitating conditions was also measured. Table 11 shows the flow parameters and global performance characteristics. Table 11 also reveals the effect of cavitation on the global performance characteristics of the propeller.

As the table shows, the thrust identities in wetted conditions are reached by increasing the advance number by a maximum of 1.4% from the values used in the tests. The calculated propeller torques and efficiencies in the wetted conditions are also very close to the measured ones.

Cavitation had no significant effect on the thrust or torque in Case 3.1 in the tests and in the simulations. In contrast, cavitation induced a significant thrust breakdown in Cases 3.2 and 3.3. The thrust breakdown was observed in both the tests and the simulations. The discrepancy between the measured and calculated global performance characteristics is slightly higher in the cavitating conditions than in the wetted conditions.

Table 11. The global performance characteristics of the cavitation investigation cases in wetted and cavitating conditions. The simulated figures are given from the fine grid results. The differences between the simulated and measured values are also shown. Measured data provided by SVA Potsdam.

Case	K_T	ΔK_T [%]	J	ΔJ [%]	10 K_Q	ΔK_Q [%]	η_O	$\Delta \eta_O$ [%]
#3.1 σ_n = 2.024								
Simul.(wetted)	0.388	0.3	1.025	0.6	0.988	1.3	0.640	-0.6
Meas. (wetted)	0.387	–	1.019	–	0.975	–	0.644	–
Simul.(cav.)	0.386	3.2	1.025	0.6	0.979	0.9	0.643	2.8
Meas. (cav.)	0.374	–	1.019	–	0.970	–	0.625	–
# 3.2 σ_n = 1.424								
Simul.(wetted)	0.245	0.0	1.286	1.3	0.708	0.0	0.707	1.2
Meas. (wetted)	0.245	–	1.269	–	0.708	–	0.699	–
Simul.(cav.)	0.202	-1.9	1.286	1.3	0.620	-1.7	0.666	1.0
Meas. (cav.)	0.206	–	1.269	–	0.631	–	0.660	–
# 3.3 σ_n = 2.000								
Simul.(wetted)	0.167	0.0	1.428	1.4	0.541	-0.7	0.700	1.9
Meas. (wetted)	0.167	–	1.408	–	0.545	–	0.687	–
Simul.(cav.)	0.142	4.4	1.428	1.4	0.496	1.4	0.650	4.3
Meas. (cav.)	0.136	–	1.408	–	0.489	–	0.623	–

Figure 35 shows the streamlines and the pressure distribution on a propeller blade, and the cavitation patterns in the Case 3.1 conditions. The results are shown at the three grid levels. A sketch of the observed cavitation extent is also shown. The pressure distribution and surface restricted streamlines in non-cavitating conditions are also given for comparison.

A strong cavitating tip vortex was present in both the cavitation tests and the simulations. It is to be noted that the first mode of tip vortex was clearly visible both in the tests and in the simulations. Root cavitation was also present in both the tests and the simulations. The extent of sheet cavitation was significantly greater in the simulations than in the tests. Sheet cavitation incepted at around radius r/R = 0.5 in the simulations, whereas in the tests the inception radius was about r/R = 0.9.

The effect of the grid resolution on the cavitating tip vortex was very clear. At the coarsest grid level the cavitating tip vortex was not captured at all. At the medium grid the tip vortex was weaker compared to the finest grid solution. The sheet cavitation extent was not that strongly dependent on the grid resolution.

The effect of the sheet cavitation on the surface restricted streamlines was significant. It can be seen in Figure 35 that the re-entrant jet reflects upwards at the closure line of the sheet cavitation. As a result, the vapour in the sheet cavity escapes through the tip vortex. As a consequence, the natural shedding of the sheet cavity did not occur and the cavity remained stable. In the wetted flow solution the streamlines travelled over the blade with nearly constant radii.

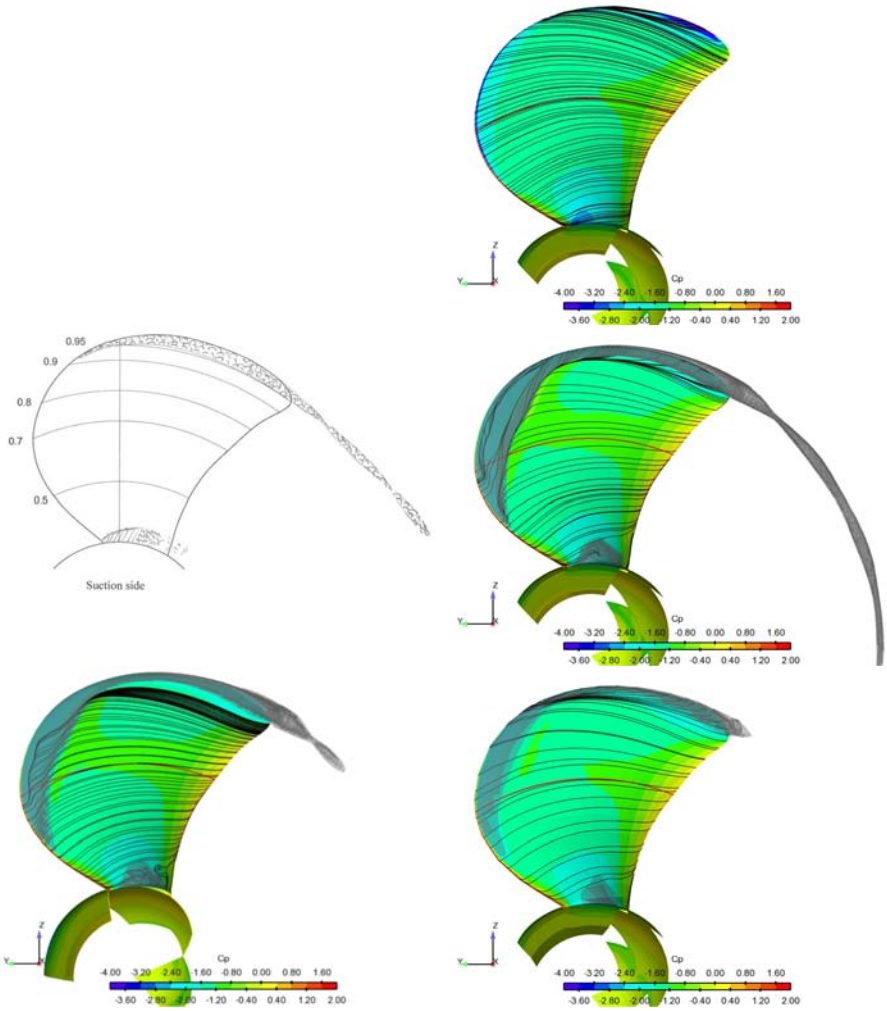

Figure 35. Cavitation extent in Case 3.1 conditions. The grey transparent isosurfaces depict the vapour volume fraction α_v = 0.5. At top: the wetted solution from the fine grid. Middle left: a sketch of the observed cavitation extent. Middle right: the fine grid solution. Bottom left: the medium grid solution. Bottom right: the coarse grid solution. The blade colour indicates the pressure difference. The surface restricted streamlines are also shown. The red lines depict the radius *r/R* = 0.7. Cavitation test data provided by SVA Potsdam.

Table 12 shows the total vapour volume $V_{v,tot}$ in the calculation domain calculated as $V_{v,tot} = \int_{domain} \alpha_v(x,y,z)\mathrm{d}V$. It is seen that the total vapour volume in the domain increases with increasing grid density. The simulation at the coarse grid level predicts about 17 % lower vapour volume compared to the fine grid result. The simulation at the medium grid level gives about 6 % lower vapour volume content than the finest grid.

The pressure distribution on the blade surface at the radius $r/R = 0.7$ in Case 3.1 is visualized in Figure 36. The pressure distribution is shown in wetted and cavitating conditions at the three investigated grid levels. As can be seen, there is a very strong and sharp pressure peak in the wetted conditions. In the cavitating conditions, the low pressure peak is cut at the vapour pressure. The pressure on the blade is at the vapour pressure under the sheet cavity. The pressure in the wetted conditions is higher at the suction side of the blade behind the low pressure peak due to the absence of the cavity. There is a pressure peak at the closure of the sheet cavity where the wetted flow travelling over the cavity hits the blade, as illustrated in Figure 9. Outside the influence of the cavity the pressure distribution in the wetted and cavitating conditions are nearly identical.

The magnitude of the low-pressure peak at the blade leading edge in the wetted conditions is very sensitive to the grid resolution. The extent of the sheet cavity is also clearly dependent on the grid resolution, as seen from the sectional pressure distribution. The same holds also for the magnitude of the pressure peak present at the closure of the sheet cavity. Outside the above-mentioned regions, the pressure distributions predicted at the different grid levels are very close to each other.

Table 12. Total vapour volume in the calculation domain at different grid resolutions in Case 3.1 conditions.

	Total vapour volume [m^3]	Difference to the fine grid result [%]
Coarse grid	1.334×10^{-6}	-17.3
Medium grid	1.514×10^{-6}	-6.1
Fine grid	1.613×10^{-6}	–

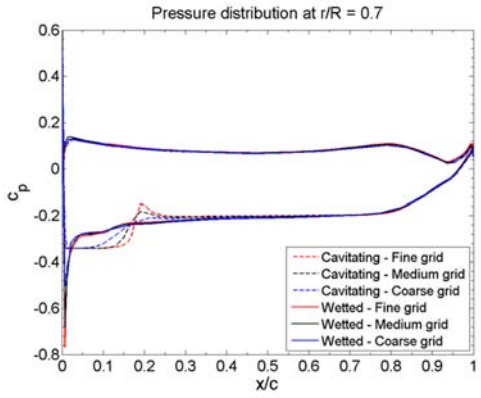

Figure 36. Pressure distributions on the blade surface at the radius $r/R = 0.7$. The results are shown for cavitating and wetted conditions at the three grid levels in Case 3.1 conditions.

Figure 37 reveals the vapour volume fraction and the evaporation rate inside the vaporous regions in the Case 3.1 conditions. The variables are visualized at the axial cuts of the cavity with a spacing of $x/D = 0.05$. It can be seen that the sheet cavity is thin and contains almost pure vapour. At the closure of the sheet cavity a mixture with a lower vapour content is present. At the tip of the propeller there are two separate regions of high vapour content in the cuts of the mixture. One is attached to the blade, the other is detached from the blade surface and is connected to the detached leading edge tip vortex. The core of the tip vortex is filled with a mixture with a very high concentration of vapour. In the root cavity the highest vapour concentration is present at the blade–hub joint.

Evaporation is high at the leading edge of the sheet cavity, whereas condensation is high in the closure of the sheet cavity. At the outer radii of the cavitating tip vortex the mixture condensates weakly. The core of the vortex evaporates due to the presence of low pressure. The diameter of the cavitating tip vortex varies along its helical path. Condensation is higher in the regions where the diameter of the tip vortex is wider, while evaporation is stronger in the regions where the diameter of the tip vortex is smaller.

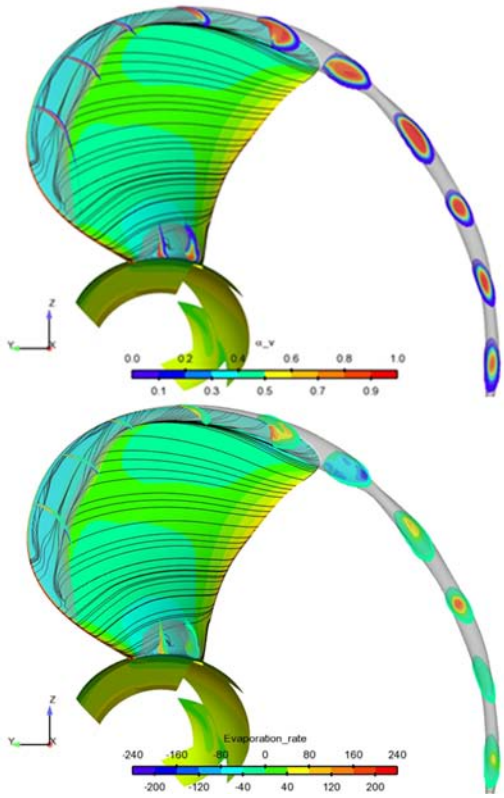

Figure 37. Axial cuts of the cavity with a spacing of $x/D = 0.05$ in the Case 3.1 flow conditions. At top: the vapour volume fraction is visualized inside the cavity isovolume of $\alpha_v > 0.01$. At bottom: the evaporation rate [kg/(sm^3)] is visualized. The negative values depict condensation and the positive values evaporation.

Figure 38 shows the pressure distribution, the axial wake together with the projected velocity vectors, and the eddy viscosity at an axial cut at $x/D = 0.2$ for the wetted and cavitating conditions of Case 3.1. It can be seen that the size and shape of the tip vortices are relatively similar in the wetted and cavitating conditions. The pressure in the cavitating tip vortex is cut at the vapour pressure.

The axial wake distribution is slightly modified by cavitation in the core of the vortex. The roll-up of the turbulent wake of the blade into the tip vortex is clearly visible in the eddy-viscosity distributions. The eddy viscosity is significantly affected by cavitation in the vortex core. In the wetted flow the eddy viscosity is at its highest in the core of the tip vortex. In the cavitating conditions the eddy viscosity diminishes in the vaporized core of the vortex. It cannot be confirmed whether the latter is due to physical effects.

Figure 39 shows a circumferential distribution of the pressure, the wake components, the eddy viscosity, and the vapour volume fraction over one circumferential period at $x/D = 0.2$ at the radius of the tip vortex core at $r/R = 0.951$. It can be seen that the pressure in the cavitating vortex core is cut at the vapour pressure. In the wetted flow the pressure is below the vapour pressure in the vortex core. Outside the vortex core the pressure distributions are close to each other in the wetted and cavitating conditions.

Regarding the grid dependency, it can be clearly seen that the pressure peak in the vortex core is highly dependent on the grid resolution. In the cavitating condition the pressure distribution at the finest and medium grid level are close to each other. The vortex core is in a slightly different position in the cavitating conditions compared to the wetted conditions.

The most significant difference in the wake distributions between the cavitating and wetted conditions are the additional peaks present in the cavitating conditions. The peaks are caused by the modified eddy viscosity due to the high vapour content in the tip vortex core. The eddy viscosity is seen to decrease dramatically as the vapour content exceeds about 50%.

The gradient of the vapour volume fraction in the cavitating tip vortex is very deep. In the vortex core the fluid mixture is almost pure vapour. The separate peaks in the wake components and in the eddy viscosity at around the 20 degrees position are caused by the wake of the blade.

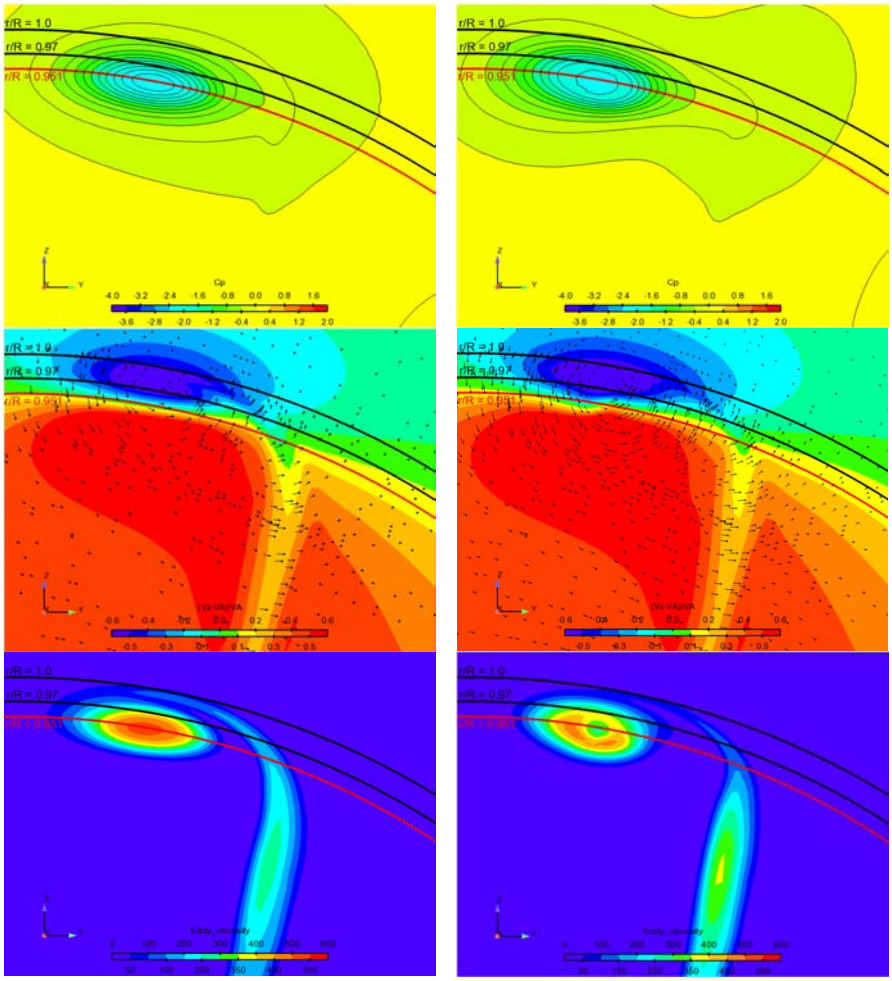

Figure 38. Axial cut of the flow field at $x/D = 0.2$ in the vicinity of the tip vortex in Case 3.1 conditions. At top: the pressure distribution. Middle: the axial wake and the projected velocity vectors. At bottom: the eddy viscosity. Left top to bottom: wetted flow solution. Right top to bottom: cavitating flow solution. The red circles refer to the radius of the tip vortex core at $r/R = 0.951$. The black circles at the radii $r/R = 0.97$ and $r/R = 1.00$ are given for a reference.

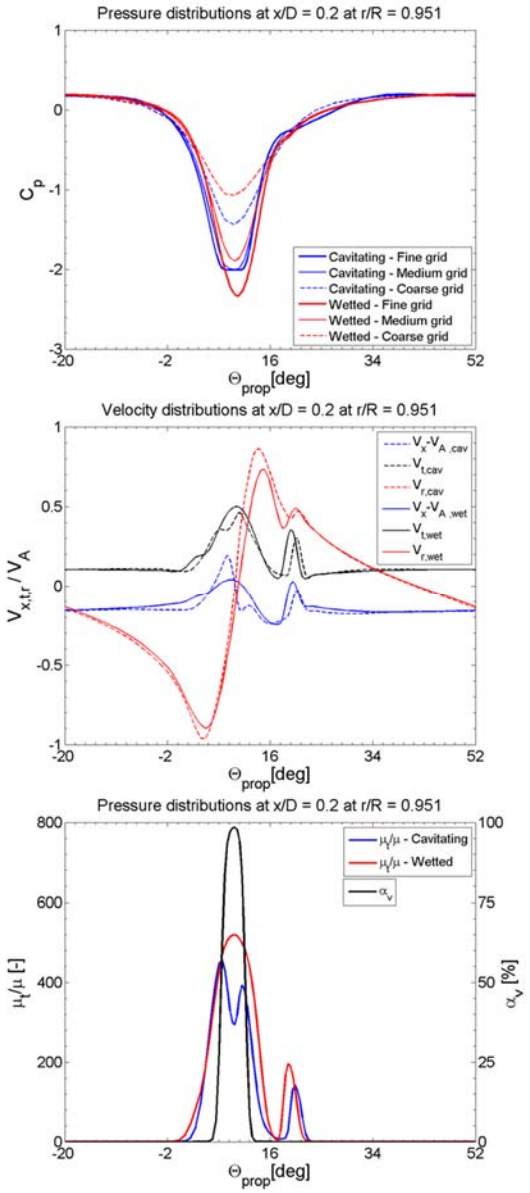

Figure 39. Flow parameters in the Case 3.1 cavitating and wetted conditions over a circumferential period of the wake at $x/D = 0.2$ at the radius of the tip vortex core. At top: the pressure distribution calculated with three grid resolutions. Middle: the wake components at the finest grid level. At bottom: the eddy viscosity together with the vapour volume fraction at the finest grid level.

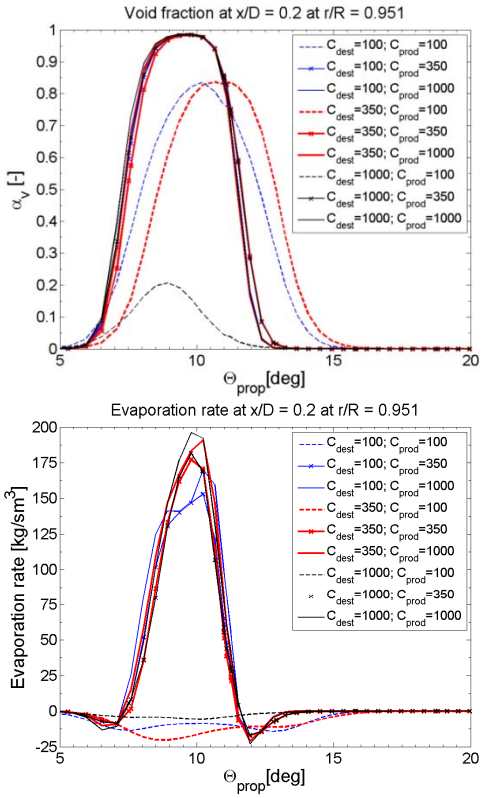

Figure 40. Influence of the empirical constants in Merkle's model on the void fraction (top) and the evaporation rate (bottom) in the core of a cavitating tip vortex. The circumferential distributions of the flow quantities in the propeller slipstream at x/D = 0.2 are presented.

The effect of the empirical constants in Merkle's mass-transfer model in Eq. (143) was investigated by altering them systematically. The calculation matrix consisted of the values 100, 350, and 1000 for both constants which gives total of 9 combinations. The results of the study are shown in Figure 40 in which the void fraction and the evaporation rate are plotted at the radius of the wetted tip vortex core at x/D = 0.2. The plotted distribution is limited in the vicinity of the tip vortex since no cavitation is present outside the vortex core.

The figure shows that the simulation results are close to each other when the empirical constant C_{prod} is higher than 100. The other constant C_{dest} has only a small effect on the simulation results. The cavitating tip vortex does not converge well with the value of C_{prod} = 100 and the location of the tip vortex alters from its location in the wetted conditions. That is clearly seen in the circumferential distributions of the void fraction and the evaporation rate.

The tip vortex core is filled with almost pure vapour. The evaporation rate is at its highest in the core of the tip vortex. At the outer side of the vortex core condensation takes place. The absolute rate of condensation at the outer side of the vortex is significantly smaller than the evaporation rate in the core of the vortex. It is seen that the higher values of C_{prod} and C_{dest} induce more evaporation in the vortex core and more condensation at the outer side of the core. The differences between the simulations with C_{dest} = 350 and C_{dest} = 1000 are small. The evaporation rate in the simulations performed with C_{dest} = 100 differ significantly from the other simulations.

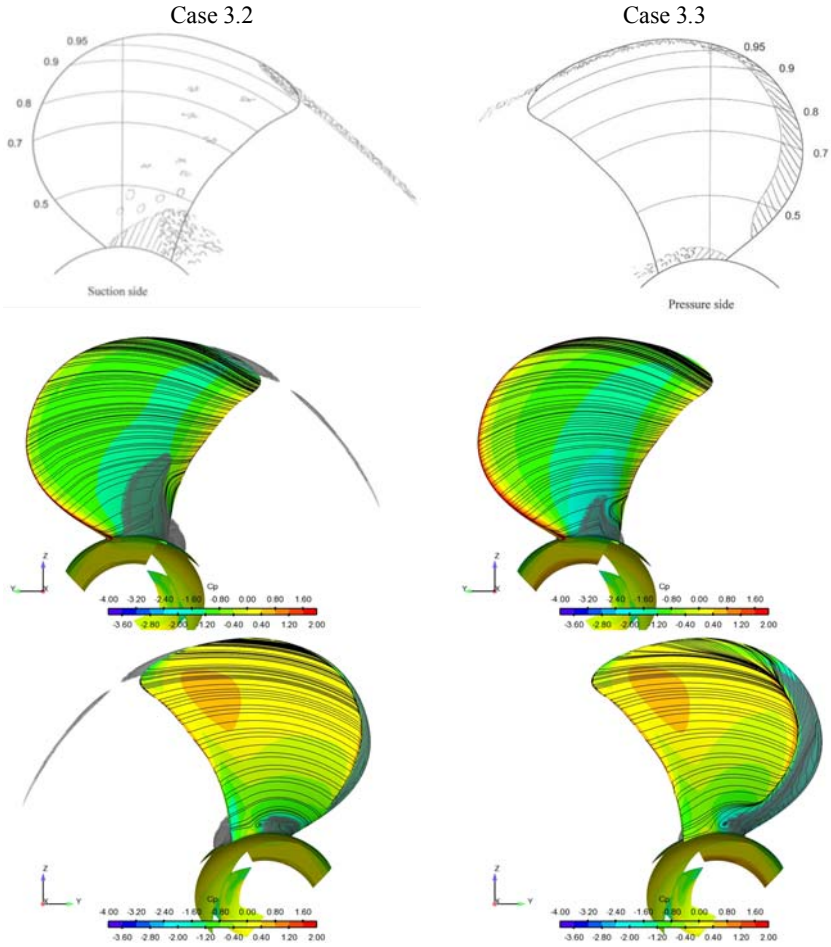

Figure 41. Cavitation patterns in the Case 3.2 (left) and Case 3.3 (right) conditions. The pressure distributions on the blades and the surface restricted streamlines are also shown. At top: sketches of observed cavitation patterns in the tests. Middle: the suction side of the blade. At bottom: the pressure side of the blade. The isosurfaces of the vapour volume fraction α_v = 0.5 are shown. Cavitation test data provided by SVA Potsdam.

Figure 41 shows the observations made in the tests and the simulation results of the cavitation extents in the flow conditions of Cases 3.2 and 3.3. The flow conditions of Cases 3.2 and 3.3 are described in Table 2. The predicted cavitation extents are visualized with the isosurfaces of the vapour volume fraction $\alpha_v = 0.5$. The surface restricted streamlines and the pressure distributions on the blade surfaces are also shown.

In the Case 3.2 conditions, tip vortex cavitation exists without the presence of sheet cavitation in both the tests and the simulations. Tip vortex cavitation is continuous in the tests. The simulated isosurfaces with lower vapour volume fractions are also continuous. Root cavitation on the suction side of the blade is also present both in the tests and in the simulations. There is also sheet cavitation on the pressure side of the blade. Root cavitation exists also on the pressure side of the blade in the Case 3.2 conditions. Sheet and root cavitation were also observed in the tests on the pressure side of the blade, although these are not shown in Figure 41.

Sheet cavitation is extensive on the pressure side of the blade both in the tests and in the simulations in the Case 3.3 conditions. The major difference between the simulations and the tests is that, in the tests, the sheet cavitation extends up to the tip of the blade and merges with the cavitating tip vortex.

4.2 Propeller in a wake field

The results of the propeller working in a wake field consist of numerical predictions of the global performance characteristics at the working point. The thrust and torque in the wetted simulations are compared to the measurements, and the cavitation extents at the different blade positions are compared to the observations.

4.2.1 Convergence

A propeller working in a wake field is an unsymmetrical problem. As such, a quasi-steady approach cannot be utilized. Instead, a time-accurate simulation was performed. The time-step in the calculations is $\Delta t = 45.54 \times 10^{-6}$ s, referring to a half degree of propeller revolution. Eighty internal iterations were performed within each time step. The quasi-steady solution of the problem was used as the initial guess for the time-accurate simulations.

The Courant number of the internal iterations within a time step was $CFL = 1.0$. The under-relaxation factors for the pressure and the velocity were $\alpha_p = 0.01$ and $\alpha_u = 0.5$, respectively. A third-order upwind-biased scheme was utilized for the discretization of the convection terms, while a second-order central-difference scheme was used for discretization of the diffusion terms. The simulations were performed with Chien's low Reynolds number k-ε turbulence model.

The convergence history of the propeller thrust and torque, and the blade thrust in the time-accurate simulations in the wetted and cavitating conditions are given in Figure 42. As the figure shows, the propeller thrust and torque converged to their final periodic shapes after about half a propeller revolution. However, to ensure the convergence, the calculations were continued for two propeller revolutions. The period of the thrust and torque for the whole propeller is one quarter of a full propeller revolution due to the sym-

metry of the four-bladed propeller. The period of a single blade thrust is one propeller revolution.

It is seen that the average thrust and torque of the cavitating propeller in the cavitating condition are slightly below those of the fully wetted propeller. The amplitude of thrust and torque in cavitating conditions are also slightly below those in wetted conditions.

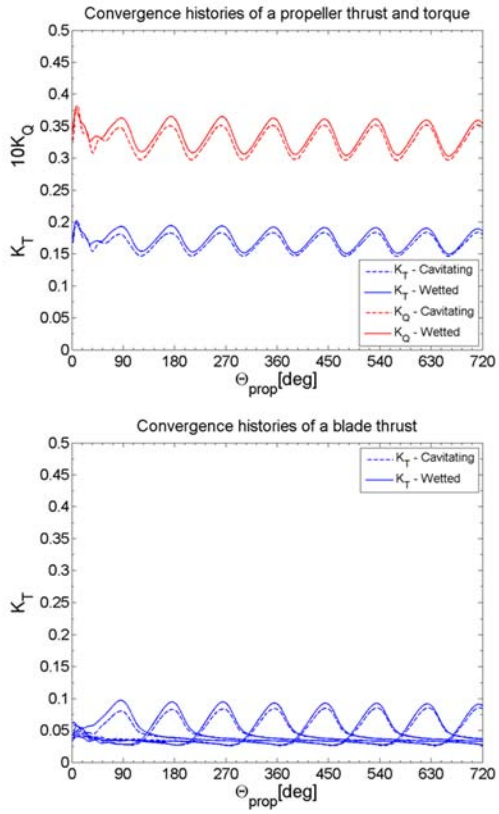

Figure 42. Convergence histories of the propeller thrust and torque (top) and the individual blade thrust (bottom) in the cavitating and wetted conditions. The quasi-steady solution is used as the initial guess in the time-accurate calculations.

4.2.2 Cavitation patterns

The average propeller thrust and torque were measured during the tests in the wetted conditions. No thrust measurements were made in the cavitating conditions. The total wake between the wake generator and the propeller plane at x/R = -0.52 was also measured by means of LDV. The cavitation observations were photographed at the different blade positions in the wake field.

Table 13 shows the calculated thrust and torque for the propeller in the wetted and cavitating conditions. The measured average values in wetted conditions are also shown. The relative peak-to-peak amplitudes of the calculated thrust and torque are slightly over 20% of the average values. The thrust amplitude in wetted conditions is slightly higher than in cavitating conditions, while the relative amplitude of the torque is practically the same in both conditions. The average thrust and torque in the cavitating conditions are slightly lower than in the wetted conditions. The calculated average thrust and torque are within a few per cent of the measured values in the wetted conditions.

Table 13. Measured and calculated thrust and torque of the propeller working in the wake field. The mean value and peak-to-peak amplitudes of the calculated characteristics are given in wetted and cavitating conditions. The discrepancy between the measured and calculated global performance characteristics in the wetted conditions are also shown. Measured data provided by CNR-INSEAN.

	K_T mean	K_T ampl.[%]	ΔK_T [%] mean	10 K_Q mean	K_Q ampl.[%]	ΔK_Q [%] mean
Simul. (wetted)	0.170	23.3	-2.9	0.331	16.9	-0.9
Simul. (cav.)	0.165	22.4	–	0.325	17.0	–
Measurements (wetted)	0.175	–	–	0.334	–	–

Figure 43 shows the calculated and measured axial total wakes at the axial plane located between the wake generator and the propeller at x/R = -0.52. The spatial resolution applied in the LDV measurements is also shown in the figure. The circumferential resolution of the measurement points is ten degrees.

The shape of the total wake is similar between the calculations and the measurements. The influence of the horizontal bars of the wake generator is clearly visible in the simulation results. The experimental results do not show the details of the total wake distribution due to the relative coarse resolution applied in the LDV measurements. The simulated average total axial velocity at the wake measurement plane inside a circle delimited by the propeller radius is 5.8% lower compared to the measurements.

The pressure distribution on a blade at the 12 o'clock position in the wetted conditions together with the surface restricted streamlines is shown in Figure 44. It can be seen that there is a very strong and narrow pressure peak at the leading edge of the blade. The leading edge vortex detaches from the leading edge of the blade at the outer propeller radii, as seen from the pressure distribution and the streamlines. Near the blade tip the streamlines are oriented nearly radially due to the high loading of the blade tip behind the wake generator.

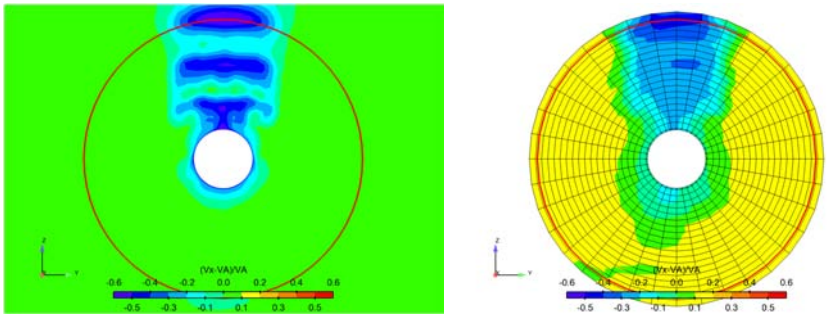

Figure 43. The axial total wake between the wake generator and the propeller at x/D = -0.52. On the left is the calculation result. On the right is the result of the LDV measurements together with the spatial resolution of the measurements. The red circles depict the propeller radius. Measured data provided by CNR-INSEAN.

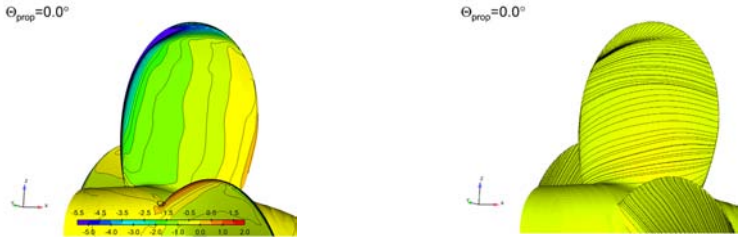

Figure 44. Propeller blade in wetted conditions at the 12 o'clock position. At left: the pressure distribution on the blade. At right: the surface restricted streamlines.

The pressure distributions on the blade at different blade positions behind the wake generator are shown in Figure 45 together with the surface restricted streamlines and the isosurfaces of the vapour volume fraction α_v = 0.1. The figures are given between the blade angular positions of Θ_{prop} = -20° … +20° with a spacing of $\Delta\Theta_{prop}$ = 10°. The photographs from the cavitation tests at the corresponding blade positions are also shown.

The low-pressure peak at the leading edge of the propeller is cut at the vapour pressure. The low pressure regions are wider in the cavitating conditions than in the wetted conditions. The streamlines are directed towards the blade tip under the cavity due to the re-entrant jet reflected from the closure of the sheet cavity. In the wetted conditions the streamlines stay more circular close to the tip of the blade.

The simulated cavitation patterns agree well with the observations. The inception of the sheet cavity is close to that of the experiments. The predicted extents of the sheet cavities at different blade positions are close to the observations made in the tests. There is a weak cavitating tip vortex present at the blade positions of Θ_{prop} = +10° and +20° in the tests that is not present in the simulations. A very weak detached sheet cavity is present in the tests at the blade position of Θ_{prop} = +20° that is not found in the simulation.

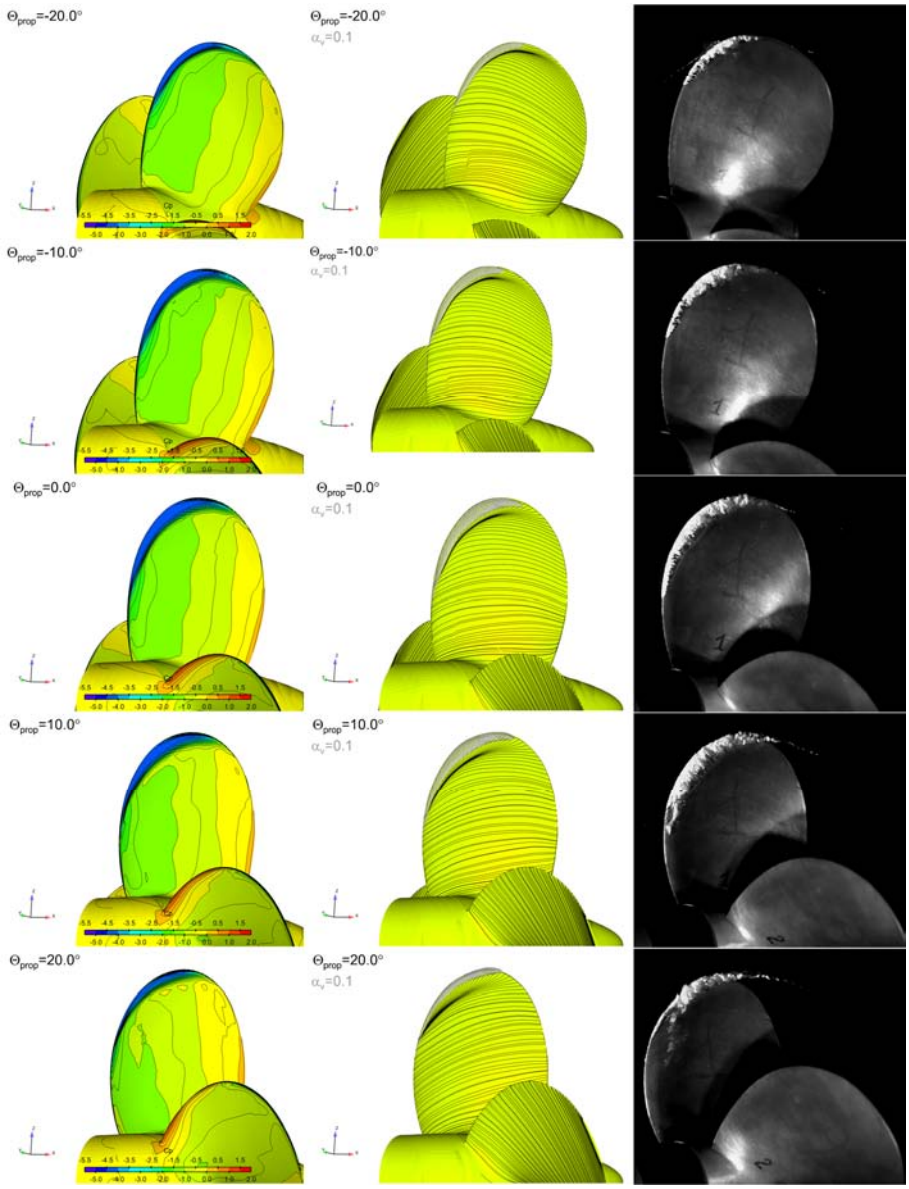

Figure 45. Cavitating propeller at different blade positions behind the wake generator. At left: the pressure distributions on the blade. Middle: the surface restricted streamlines and the isosurfaces of the vapour volume fraction $\alpha_v = 0.1$. At right: photographs of the cavitating propeller in the tests. The blade positions are from Θ_{prop} = -20° (top) to Θ_{prop} = +20° (bottom) with a spacing of $\Delta\Theta_{prop}$ = 10°. (Test photographs courtesy of CNR-INSEAN.)

5. Discussion

The cavitation model implemented in FINFLO was validated for model-scale ship propeller flows using the RANS approach. The flow equations were solved using the pressure correction method. The implemented cavitation model is homogeneous and the mass transfer rate is driven by the difference between local pressure and vapour pressure. The FINFLO code solves the continuity equation for each phase and the momentum and turbulence equations for the mixture of phases. The simulations were performed with Chien's low Reynolds number k-ε turbulence model. The mass transfer model used is similar to that of Merkle et al. (1998).

The convergence of the pressure correction method in the wetted and cavitating conditions is good. A minor drawback is that the multigrid method cannot be applied in the multiphase calculations. However, due to increased computing power, calculation time in quasi-steady cases is no-longer critical, even without the multigrid method. In time-accurate calculations, the multigrid method is not that significant from the CPU time point of view.

The results of the simulated global propeller performance characteristics agreed well with the experimental results in wetted open water conditions over a wide range of the investigated advance numbers. The global performance characteristics have traditionally been predicted well with FINFLO. An estimate of the order of accuracy of the numerical simulations was performed for the global performance characteristics of the propeller using the Richardson extrapolation method. The order of accuracy for thrust and torque were found to be 1.9 and 2.5, respectively. The verification and validation of the simulations were carried out for the global performance characteristics in accordance with the ITTC recommended procedure. It was found that validation was achieved by the simulations.

A more challenging task was to accurately predict the propeller tip vortices and the wake field composed of the detached boundary layers of the blades. It was found that the wake field of the propeller dissipates too much unless an appropriate grid resolution is set for the regions of large velocity gradient, i.e. over the tip vortices and the blade wakes. A reasonable grid convergence is achieved when the resolution in the cross section of the tip vortex is about 20 × 20 cells. In the cross section of the blade wake about 10 cells are needed.

The difficulty in simulating the wake field of a propeller is that the exact locations of the tip vortices and the blade wakes are not known before the simulations are performed. The entire slipstream of the propeller cannot be filled with a high resolution grid as this

would increase the calculation time excessively. Therefore, in the calculations presented in this thesis the slipstream grid is created iteratively. The pitch and contraction of the propeller slipstream are first estimated. The exact locations of the tip vortices and the blade wakes are then determined from the initial simulations. The grid is then adjusted so that the high resolution regions of the grid match the locations of the tip vortices and the blade wakes. An alternative to focusing cells on the tip vortex and blade wake regions would be to use overlapping grids. This was not done here, although the method is implanted in the FINFLO code.

The simulated tip vortices were more dissipative compared to the LDV measurements in the tests. Nevertheless, the circumferential distributions of the wake components in the tip vortex regions show that a reasonable agreement with the test measurements is achieved. It is generally known that the k-ε turbulence models produce too much eddy viscosity in the flow field. The k-ε model was chosen to be used in these initial validation calculations of two-phase flows due to VTT's extensive experience of applying the model to single-phase propeller flows. Initial trials conducted with the SST k-ω model gave less dissipation in the propeller tip vortices than the k-ε model. Comparison of the turbulence models is omitted from the scope of this thesis.

The predicted sheet cavitation on the suction side of the PPTC propeller was more extensive in the high propeller loading conditions of Case 3.1 than that observed in the tests. This discrepancy is likely to be caused by laminar separation of the flow at the leading edge of the blade in the experiments. The cavitation inception is delayed in the laminar flow conditions.

Merkle's mass transfer model activates as the pressure drops below the vapour pressure. As the angle of attack of the flow is practically the same in both the experiments and the simulations, the low pressure peak at the leading edge of the blade should be about the same in the experiments and in the simulations. The absence of sheet cavitation in the tests at the lower blade radii is therefore most likely to be caused by laminar separation of the flow.

The above assumption is confirmed by the fact that in the smp'11 workshop (Abdel-Maksoud, 2011), at which PPTC propeller cases were studied, participants who utilized Singhal's mass transfer model in their calculations predicted a similar sheet cavitation extent as observed in the tests. Singhal's mass transfer model is activated only in a turbulent flow regime.

It can be further speculated that the experimental results would be closer to the simulated results if the tests were performed with a higher Reynolds number, or if turbulence stimulators were applied at the leading edge of the model propeller. At the full scale, the sheet cavitation extent is likely to be closer to the simulation result since the whole flow field would then be turbulent.

The effect of sheet cavitation on the surface restricted streamlines under the cavity is clearly visible. The re-entrant jet is reflected at the closure line of the cavity to its normal direction. This phenomenon is in agreement with the experimental observations. In the wetted flow conditions the streamlines travel over the blade at almost constant radii.

The sectional pressure distributions at radius $r/R = 0.7$ on the blade shows that the low-pressure peak at the leading edge is cut at the vapour pressure in the cavitating conditions. Furthermore, a high pressure peak exists at the cavity closure line where the wetted flow

travelling over the cavity hits the blade surface, as explained in Chapter 1.2.2. It is also seen that the cavitation extent is sensitive to the grid resolution. This holds especially for tip vortex cavitation.

The simulation results for the cavitating tip vortex do not seem to be very sensitive to the empirical constants in Merkle's mass transfer model. A reasonable choice for the constants seems to be between 350 and 1000. It was found that the convergences of the simulations with higher constant values were less stable.

One could expect that the natural shedding of the sheet cavity would occur at least at the lower propeller radii in the case where an extensive sheet cavity is present on the suction side of the blade. It is repeatedly reported that the RANS models are not capable of producing natural shedding of a sheet cavity due to over prediction of the eddy viscosity at the closure of the sheet cavity, see for example Reboud et al. (1998), Coutier-Delgosha et al., (2003), Goncalves et al. (2010), Hoekstra et al. (2011), and Bensow (2011). To overcome this problem, Reboud et al. (1998) introduced the following ad hoc modification of the k-ε turbulence model in order to reduce the eddy viscosity in a mixture:

$$\mu_t = f(\rho) C_\mu \frac{k^2}{\varepsilon} \tag{164}$$

where the weighting function $f(\rho)$ is defined as

$$f(\rho) = \rho_v + \left(\frac{\rho_v - \rho}{\rho_v - \rho_l}\right)^n (\rho_v - \rho_l) \tag{165}$$

with n being a large value. Parameter n has been given values from 10 to 1000 in the literature. The modified turbulence model described above is not used in the present simulations, as implementing the modified model could induce natural shedding of the turbulence. Moreover, the works of Bensow (2011) and Li and Grekula (2008), for example, have shown that the dynamics of the shedding mechanism can be predicted more precisely by means of LES or DES.

The influence of varying eddy viscosity in the mixture on the flow velocity is also evident in the vaporous core of the propeller tip vortex. The altering eddy viscosity induces additional humps and hollows in the circumferential distribution of the wake components in the tip vortex region. In the wetted conditions, the eddy viscosity is at its highest at the centre of the core. In the cavitating conditions the eddy viscosity is at its highest around the region in the tip vortex with a vapour volume fraction of $\alpha_v = 0.5$. The eddy viscosity decreases as the vapour volume fraction further increases in the vortex core. The vapour volume fraction is very close to unity in the core of the tip vortex. The slope of the vapour volume fraction is steep in the tip vortex.

The first mode of the cavitating tip vortex in the simulation agrees well with the observations in the cavitation tests. The evaporation and condensation behaviours of the tip

vortex were also found to be qualitatively reasonable. The evaporation rate is high in the low-pressure core of the vortex, while the mixture condensates weakly at the outer radii of the tip vortex. Condensation is higher in the regions where the radius of the tip vortex is large, while the tip vortex evaporates more in the regions where the tip vortex diameter is small.

The thrust break down is connected to the pressure side cavitation in the low-loading conditions in the tests and in the simulations. The simulated cavitation extent on the pressure side of the blade agrees well with the observations made in the tests.

The cavitation model was validated also for a case where a propeller is working in a wake field. The wake field was created by an artificial wake generator. The geometry of the wake generator was modelled in the calculation domain. The simulated and measured total wakes between the propeller and the wake generator are similar in shape. The influence of the structural details of the wake generator on the total wake is more clearly visible in the simulations than in the tests. This is due to the rather coarse spatial resolution used in the LDV measurements.

The cavitation extent on the propeller blades is rather small in the analyzed flow conditions in the wake field. The thrust and torque variations are therefore rather similar in the wetted and cavitating conditions. The simulated averaged thrust and torque agree well with the measured results.

The simulated cavitation inception location and cavitation extent on the propeller in the wake field are close to the observations made in the tests. The flow from the wake generator to the propeller is turbulent. This ensures that there is no delay in the cavitation inception in the tests due to laminar separation of the flow. The weak cavitating tip vortex present in the tests was not found in the simulations. It can be expected that the cavitating tip vortex would have been found in the simulations if a denser grid had been utilized.

6. Conclusions and future work

Based on the simulations presented in this thesis it is concluded that the cavitation model implemented in the RANS equation solver FINFLO gives a good estimation of cavitation inception and extent in propeller flows. The global performance characteristics in the simulations agree well with those measured in tests, both in the wetted and cavitating conditions. The validation of the simulated global propeller performance characteristics has been achieved according to the methodology recommended by the ITTC. The thrust breakdown related to the pressure side cavitation was observed in the tests and in the simulations.

The tip vortices and the wakes from the blades must be covered with a dense grid in order to solve them accurately. The entire slipstream cannot be filled with a high density grid due to the limitations in computing power. The cells must therefore be concentrated mainly over the tip vortices and the blade wakes to limit the total number of cells in the domain. The exact locations of the tip vortices and blade wakes are not known a priori, so that the grid must be created iteratively in the slipstream of the propeller. The simulation of the cavitating tip vortices is not very sensitive to the empirical coefficients in Merkle's mass transfer model. The values of $C_{dest} = C_{prod} = 350$ seem to be a reasonable choice for the parameters. Lower values ruin the solution and higher values destabilize the convergence.

It is important to also keep in mind the uncertainties related to the tests when comparing the numerical results with the outcome of the experiments. The inception of sheet cavitation was significantly delayed in the tests conducted in a uniform inflow compared to the numerical results in one of the simulated cases. This can be attributed to laminar separation of the flow at the leading edge of the model propeller in the tests. In the case where the propeller was working in a turbulent wake field, the observed and simulated cavitation inception points were similar.

The high viscosity in the mixture at the closure line of the sheet cavity dissipates the reentrant jet and prevents the natural shedding of the sheet cavity that would have been expected in some of the simulated cases. The applied eddy viscosity turbulence model is known to overestimate the turbulent viscosity in a mixture of vapour and water.

Regarding future work, a modified eddy viscosity model should be implemented in the code. The dynamics of the sheet and tip vortex cavitation could also be studied using a LES/DES approach.

References

Abdel-Maksoud, M. (editor), 2011. Proceedings of smp'11 Workshop on Cavitation and Propeller Performance. smp'11, The Second International Symposium on Marine Propulsors. Hamburg, Germany, 17.–18.6.2011. 322 p. ISBN: 978-3-86342-238-7. url: http://www.marinepropulsors.com/smp/files/downloads/smp11_workshop/smp11_workshop/ index.htm.

Aït-Bouziad, Y., 2006. Physical Modelling of Leading Edge Cavitation: Computational Methodologies and Application to Hydraulic Machinery. Ph.D. Thesis. Ecole Polytechnique Fédérale de Lausanne. 209 p.

Anonym, 1981. Turbinia. Tyne And Wear Museum Service booklet on Turbinia. The American Society of Mechanical Engineering. 12 p. url: http://files.asme.org/ASMEORG/Communities/ History/ Landmarks/5652.pdf.

Arakeri, V., 1975. Viscous Effects on the Position of Cavitation Separation from Smooth Bodies. Journal of Fluid Mechanics, Vol. 68, pp. 779–799.

Arndt, R., Song, C., Kjeldsen, M., He, J., Keller, A., 2000. Instability of Partial Cavitation: A Numerical/Experimental Approach. Proceedings of 23rd Symposium on Naval Hydrodynamics. Pp. 599–615. Val de Ruil, France, 17.–22.9.2000.

Baer, M., Nunziato, J., 1986. A Two-Phase Mixture Theory for the Deflagration-to-Detonation Transition (DDT) in Reactive Granular Materials. International Journal of Multiphase Flow, Vol. 12, pp. 861–889.

Bark, G., Berchiche, N., Grekula, M., 2004. Application of Principles for Observation and Analysis of Eroding Cavitation – The EROCAV Observation Handbook. Ed. 3.1. Dept. of Naval Architecture and Ocean Engineering, Chalmers University of Technology. 186 p.

Barkmann, U., 2011. Potsdam Propeller Test Case (PPTC) Open Water Tests with the Model Propeller VP1304. SVA Potsdam Model Basin Report No. 3752. 32 p. url: http://www.sva-potsdam.de/assets/files/smp11/SVA%20report%203752.pdf.

Bensow, R., 2011. Simulation of the Unsteady Cavitation on the Delft Twist11 foil Using RANS, DES and LES. Second International Symposium on Marine Propulsors smp'11, Workshop: Cavitation on foil. Hamburg, Germany, 17.–18.6.2011. 9 p. url: http://www.marinepropulsors.com/smp/files/downloads/smp11_workshop/smp11_workshop/I-2.1_Bensow.pdf.

Berg, A., Iben, U., Meister, A., Schmidt, J., 2005. Modeling and Simulation of Cavitation in Hydraulic Pipelines Based on the Thermodynamic and Caloric Properties of Liquid and Steam. Shock Waves, Vol. 14, No. 1–2, pp. 111–121.

Brennen, C., 1995. Cavitation and Bubble Dynamics. Oxford University Press. 254 p. ISBN 0-19-509409-3. url: http://authors.library.caltech.edu/25017/1/cavbubdy nam.pdf.

Briggs, L., 1950. Limiting Negative Pressure of Water. Journal of Applied Physics, Vol. 21, No. 721, pp. 721–722.

Brujan, E.-A., 2011. Cavitation in Non-Newtonian Fluids. Springer. 269 p. ISBN 978-3-642-15342-6.

Burgers, J., 1948. A Mathematical Model Illustrating the Theory of Turbulence. Advances in Applied Mechanics, Vol. 1, pp. 171–199.

Carlton, J., 1994. Marine Propellers and Propulsion. Butterwoth-Heineman Ltd. 498 p. ISBN 0-7506-1143-X.

Chien, K.-Y., 1982. Predictions of Channel and Boundary-Layer Flows with a Low-Reynolds-Number Turbulence Model. AIAA Journal, Vol. 20, No. 1, pp. 33–38.

Coutier-Delgosha, O., Fortes-Patella, R., Reboud, J., 2003. Evaluation of the Turbulence Model Influence on the Numerical Simulations of Unsteady Cavitation. Journal of Fluids Engineering, Vol. 125, Issue 1, pp. 38–45.

Coutier-Delgosha, O., Deniset, F., Astolfi, J., Leroux, J., 2007. Numerical Prediction of Cavitating Flow on a Two-Dimensional Symmetrical Hydrofoil and Comparison to Experiments. Journal of Fluids Engineering, Vol. 129, No. 3, pp. 279–292.

Daily, J., Johnson, V. Jr., 1956. Turbulence and Boundary Layer Effects on Cavitation Inception from Gas Nuclei. Transactions of ASME, Vol. 78, pp. 1695–1706.

de Lange, D., de Bruin, G., van Winjgaarden, L., 1996. Numerical Modeling of Unsteady 2-D Sheet Cavitation. 3èmes Journées Cavitation. Grenoble, Switzerland, 13.–14.11.1996.

de Lange, D., de Bruin, G., 1998. Sheet Cavitation and Cloud Cavitation, Re-Entrant Jet and Three-Dimensionality. Applied Scientific Research, Vol. 58, pp. 91–114.

Dieval, L., Arnoud, M., Marcer, R., 1998. Numerical Modeling of Unsteady Cavitating Flow by a VoF Method. Proceedings of the Third International Symposium on Cavitation, Vol. 2, pp. 243–248. Grenoble, France, 7.–10.8.1998.

Dular, M., Bachert, R., Schaad, C., Stoffel, B., 2007. Investigation of a Re-Entrant Jet Reflection at an Inclined Cavity Closure Line. European Journal of Mechanics B/Fluids, Vol. 26, pp. 688–705.

Duttweiler, M., Brennen, C., 1998. Partial Cavity Instabilies. Proceedings of US-Japan Seminar: Abnormal Flow Phenomen in Turbomachnines, Osaka, Japan. 9 p.

FINFLO, 2012. FINFLO User Guide. Version 8.1. Finflo Ltd. 100 p.

Foeth, E.J., van Terwisga, T., 2006. The Structure of Unsteady Cavitation. Part I: Observation of an Attached Cavity on a Three-Dimensional Hydrofoil. Proceedings of the 6th International Conference on Cavitation CAV2006. 18 p. Wageningen, The Netherlands, 11.–15.9.2006.

Foeth, E.-J., 2008. The Structure of Three-Dimensional Sheet Cavitation. Ph.D. Thesis. Delft University, the Netherlands. 221 p. ISBN 978-90-6464-236-4. url: http://repository.tudelft.nl/view/ir/uuid%3A61690ddb-1433-4205-954c-85d839dab4cf.

Fortes-Patella, R., Reboud, J.L., Briancon-Marjollet, L., 2004. A Phenomenological and Numerical Model for Scaling the Flow Aggressiveness in Cavitation Erosion, Proceedings of EROCAV Workshop. Val de Ruil, France, 27.–28.5.2004.

Franc, F.-P., Michel, K.-M., 1985. Attached Cavitation and the Boundary Layer: Experimental Investigation and Numerical Treatment. Journal of Fluid Mechanics, Vol. 154, pp. 63–90.

Franc, F.-P., Michel, J.-M., 2004. Fundamentals of Cavitation. Springer. 264 p. ISBN 0-4020-2233-8.

Fruman, D., Dugué, C., Pauchet, A., Cerrutti, P., Briancon-Marjollet, L., 1992. Tip Vortex Roll-Up and Cavitation. Proceedings of the 19th International Symposium on Naval Hydrodynamics. Pp. 633–651. Seoul, Korea, August 24–28.

Fureby, C., Grinstein, F., 2002. Large Eddy Simulation of High-Reynolds-Number Free and Wall-Bounded Flows. Journal of Computational Physics, Vol. 181, pp. 68–97.

Geurst, I., 1961. Linearized theory of two-dimensional cavity flows. Ph.D. Thesis. Delft University, the Netherlands. 222 p. url: http://repository.tudelft.nl/assets/uuid:d61a016e-a7fe-4830-b079-41c9ca2dd8bb/84513339.pdf.

Goncalves, E., Decaix, J., Patella, R., 2010. Unsteady Simulation of Cavitating Flows in Venturi. Journal of Hydrodynamics, Vol. 23, No. 5, pp. 753–758.

Hallander, J., 2002. Influence of Acoustic Interaction between Cavities That Generate Cavitation Noise. Ph.D. Thesis. Chalmers University of Technology. 62 p. ISBN 91-7291-124-7.

Hammit, F., 1963. Observations on Cavitation Damage in a Flowing System. Transaction of ASME, Journal of Basic Engineering, 3 p.

Hammit, F., 1980. Cavitation and Multiphase Flow Phenomena. McGraw-Hill Inc. 423 p. ISBN 0-07-025907-0.

Harvald, S., 1983. Resistance and Propulsion of Ships. John Wiley & Sons, Inc. 353 p. ISBN 0-471-06353-3.

Heinke, H.-J., 2011. Potsdam Propeller Test Case (PPTC) Cavitation Tests with the Model Propeller VP1304. SVA Potsdam Model Basin Report No. 3753. 68 p. url: http://www.sva-potsdam.de/ asets/files/smp11/SVA%20report%203753.pdf.

Hellsten, A., 2004. New Two-Equation Turbulence Model for Aerodynamics Applications. Ph.D. Thesis. Helsinki University of Technology. 191 p. ISBN 951-22-6933-3. url: http://lib.tkk.fi/Diss/2004/isbn9512269341/ isbn9512269341.pdf.

Hemilä, S., Utriainen, J., 1991. Lämpöoppi. 2nd edition. Suomen Fyysikkoseuran julkaisuja 3. 194 p. In Finnish. ISBN 951-96117-2-X.

Hirt, C., Nichols, B., 1981. Volume of Fluid (VoF) method for the dynamics of free boundaries. Journal of Computational Physics, Vol. 39, Issue 1, pp. 201–225.

Hoekstra, M., van Terwisga, T., Foeth. E.-J., 2011. smp'11 Workshop – Case 1: DelftFoil. Second International Symposium on Marine Propulsors smp'11. Workshop: Cavitation on foil. 5 p. Hamburg, Germany, 17.–18.6.2011. url: http://www.marinepropulsors.com/smp/files/downloads/smp11_workshop/smp11_workshop/I-1_Hoekstra.pdf.

Huuva, T., 2008. Large-Eddy Simulation of Cavitating and Non-Cavitating Flow. Ph. D. Thesis, Chalmers University of Technology. 97 p.

Iben, U., Wrona, F., Munz, C.-D., Beck, M., 2002. Cavitation in Hydraulic Tools Based on Thermodynamic Properties of Liquid and Gas. Journal of Fluids Engineering, Vol. 124, No. 4, pp. 1011–1017.

ITTC, 1999. The Specialist Committee on Computational Method for Propeller Cavitation. Final Report and Recommendations to the 22nd ITTC. Proceedings of the 22nd International Towing Tank Conference, Vol. 3. 35 p. url: http://ittc.sname.org/Computational%20Methods%20for%20Propeller%20Cavitation.pdf.

ITTC, 2002. ITTC – Recommended Procedures and Guidelines, Testing and Extrapolation Methods, Propulsion; Cavitation, Description of Cavitation Appearances. ITTC Report 7.5-02 03-03.2, Revision 1, Propulsion Committee of 23rd ITTC. 7 p. url: http://ittc.sname.org/ 2006_recomm_proc /7.5-02-01-03.pdf.

ITTC, 2008. ITTC – Recommended Procedures and Guidelines, Uncertainty Analysis in CFD Verification and Validation, Methodology and Procedures. ITTC Report 7.5-03-01-01, Revision. 02. 12 p. url: http://ittc.sname.org/CD%202011/ pdf%20 Procedures %202011/7.5-03-01-01.pdf.

ITTC, 2011. ITTC – Recommended Procedures, Fresh Water and Sea Water Properties. ITTC Report 7.5-02-01-03, Revision 2, 26th ITTC Specialist Committee on Uncertainty Analysis. 45 p. url: http://www.laboceano.coppe.ufrj.br:8080/ittc2011/ documents/2011/pdf%20Procedures% 202011/7.5-02-01-03.pdf.

Jameson, A., Yoon, S., 1986. Multigrid Solution of the Euler Equations Using Implicit Schemes. AIAA Journal, Vol. 24, No. 11, 9 p.

Johanssen, P., Davidson, L., 1995. Modified Collocated SIMPLEC Algorithm Applied to Buoyancy-affected Turbulent Flow Using a Multigrid Procedure. Numerical Heat Transfer, Part B, Vol. 28, pp. 39–57.

Kato, H., Konno, A., Maeda, M., Yamaguchi, H., 1996. Possibility of Quantitative Prediction of Cavitation Erosion without Model Test. Journal of Fluids Engineering, Transaction of ASME, Vol. 118, No. 3, pp. 582–588.

Kawanami, Y., Kato, H., Yamaguchi, H., 1998. Three-Dimensional Characteristics of the Cavities Formed on a Two-Dimensional Hydrofoil. Proceedings of the 3rd International Symposium of Cavitation, Vol. 1, Grenoble, France. Pp. 191–196.

Kawanami, Y., Kato, H., Yamaguchi, H., Maeda, M., Nakasumi, S., 2002. Inner Structure of Cloud Cavity on a Foil Section. JSME International Journal, Series B, Vol 45, No. 3, pp. 655–661.

Kerwin, J., Kinnas, S., Wilson, M., McHugh, M., 1986. Experimental and Analytical Techniques for the Study of Unsteady Propeller Sheet Cavitation. Proceedings of the 16th Symposium on Naval Hydrodynamics. 28 p. Berkeley, USA, 13.–16.7.1986.

Kinnas, S., 1985. Non-Linear Corrections to the Linear Theory for the Prediction of the Cavitating Flow around Hydrofoils. Ph.D. Thesis. M.I.T. 144 p. url: http://dspace.mit.edu/bitstream/handle/1721.1/15257/13321424.pdf?sequence=1.

Kinnas, S., Griffin, P., Choi, J., Kosal, E., 1998. Automated Design of Propeller Blades for High-Speed Ocean Vehicle Application. Transaction of SNAME, San Diego, USA.

Koop, A., 2008. Numerical Simulation of Unsteady Three-Dimensional Sheet Cavitation. Ph.D. Thesis. University of Twente. 241 p. url: http://doc.utwente.nl/61072/1/thesis_A_Koop.pdf.

Kubota, A., Kato, H., Yamaguchi, H., 1992. A New Modelling of Cavitating Flows; A Numerical Study of Unsteady Cavitation on a Hydrofoil Section. Journal of Fluid Mechanics, Vol. 240, pp. 59–62.

Kuiper, G., 1981. Cavitation Inception on Ship Propeller Models. Netherlands Ship Model Basin, Publication No. 655, 231 p.

Kuiper, G., 2011. Lecture notes on course Cavitation in Ship Propulsion, Delft University. url: http://ocw.tudelft.nl/courses/marine-technology/cavitation-on-ship-propellers/readings/.

Kuntz, R., Boger, D., Stinebring, D., Chyczewski, Lindau, J., Gibeling, H., Venkateswaran, S., Govindan, T., 2000. A Preconditioned Navier-Stokes Method for Two-Phase Flows with Application to Cavitation Prediction. Computers and Fluids, Vol. 29, No. 8, pp. 849–875.

Laberteaux, K., Ceccio, S., 2001a. Partial Cavity Flows. Part 1 – Cavities Forming on Models without Spanwise Variation. Journal of Fluid Mechanics, Vol. 431, pp. 1–41.

Laberteaux, K., Ceccio, S., 2001b. Partial Cavity Flows. Part 2 – Cavities Forming on Test Objects with Spanwise Variation. Journal of Fluid Mechanics, Vol. 431, pp. 43–63.

Lamb, H., 1932. Hydrodynamics. 6th Edition. Cambridge University Press. 738 p.

Le, Q., Franc, J.-P., Michel, J.-M., 1993. Partial Cavities: Global Behavior and Mean Pressure Distribution. Journal of Fluids Engineering, Vol. 115, pp. 243–248.

Lee, H., Kinnas, S., 2004. Application of a Boundary Element Method in the Prediction of Unsteady Blade Sheet and Developed Tip Vortex Cavitation on Marine Propellers. Journal of Ship Research, Vol. 48, No. 1, pp. 15–30.

Lemonier, H., Rowe, A., 1988. Another Approach in Modeling Cavitating Flows. Journal of Fluid Mechanics, Vol. 195, pp. 557–580.

Li, D.-Q., Grekula, M., 2008. Prediction of Dynamic Shedding of Cloud Cavitation on a 3D Twisted Foil and Comparison with Experiments. Proceedings of 27th Symposium on Naval Hydrodynamics. Pp. 399–415. Seoul, Korea, 5.–10.10.2008.

Li, T., Matusiak, J., Lehtimäki, R., 2001. Numerical Simulation of Viscous Flows with Free Surface around Realistic Hull Forms with Transom. International Journal for Numerical Methods in Fluids, Vol. 37, No. 5, pp. 601–624.

Lu, N.-X., 2010. Large Eddy Simulation of Cavitating Flow on Hydrofoils. Licentiates thesis. Chalmers University of Technology. 47 p.

Mach, K.-P., 2011. Potsdam Propeller Test Case (PPTC) LDV Velocity Measurements with the Model Propeller VP1304. SVA Potsdam Model Basin Report No. 3754. 70 p. url: http://www.sva-potsdam.de/assets/files/smp11/SVA%20report%203754.pdf.

Martio, J., Sipilä, T., Sánchez-Caja, A., Saisto, I., Siikonen, T., 2011. Evaluation of the Propeller Hull Vortex Using a RANS Solver. Proceedings of the Second International Symposium on Marine Propulsors smp'11. Pp. 278–283. Hamburg, Germany, 15.–17.6.2011.

Matusiak, J., 1992. Pressure and Noise Induced by a Cavitating Marine Screw Propeller. Ph.D. Thesis, Helsinki University of Technology. VTT Technical Research Centre of Finland, Ship Laboratory. VTT Publications 87. 102 p. ISBN 951-38-4065-4.

Matusiak, J., 2000. Laivan propulsio. Helsinki University of Technology. Report M-176. 133 p. In Finnish. ISBN 951-22-1694-9.

McCormick, B., 1962. On Cavitation Produced by a Vortex Trailing from a Lifting Surface. Journal of Basic Engineering, pp. 369–379.

Menter, F., 1994. Two-equation eddy-viscosity turbulence models for engineering applications. AIAA Journal, Vol. 32, No. 8, pp. 1598–1605.

Merkle, C., Feng, J., Buelow, P. 1998. Computational Modeling of the Dynamics of Sheet Cavitation. Proceedings of Third International Symposium on Cavitation, Vol. 2. Pp. 307–311. Grenoble, France, 7.–10.8.1998.

Mikkola, T., 2000. Implementation of an Implicit Scheme into a Free Surface RANS Solver in Order to Improve the Convergence. Helsinki University of Technology report M-257. 80 p.

Mikkola, T., 2009. Simulation of Unsteady Free Surface Flows – Code Verification and Discretisation error. Ph.D. Thesis, Helsinki University of Technology. 259 p. ISBN 978-952-248-136-8. url: http://lib.tkk.fi/Dis/2009/ isbn/9789522481375/.

Neaves, M., Edwards, J., 2006. All-Speed Time-Accurate Underwater Projectile Calculations Using a Preconditioning Algorithm. Journal of Fluid Engineering, Vol. 128, No. 2, pp. 284–296.

NIST Chemistry Webbook. National Institute of Standards and Technology. url: http://webbook.nist.gov/.

Oseen, C., 1912. Über Wirbelbewegune in Einer Reiben-Den Flussigkeit. Arkiv för matematik, astronomi och fysik, Vol. 7, pp. 14–21.

Pereira, F., Salvatore, F., Di Felice, F., 2004a. Measurement and Modelling of Propeller Cavitation in Uniform Inflow. Journal of Fluids Engineering, Vol. 126, pp. 671–679.

Pereira, F., Salvatore, F., Di Felice, F., Soave, M., 2004b. Experimental Investigation of a Cavitating Propeller in Non-Uniform Inflow. Proceedings of the twenty-fifth ONR Symposium on Naval Hydrodynamics. 13 p. St. John's, Canada, 8.–13.8.2004.

Plesset, M., 1949. The Dynamics of Cavitation Bubbles. ASME Journal of Applied Mechanics, pp. 27–232.

Plesset, M., Prosperetti, A., 1977. Bubble Dynamics and Cavitation. Annual Review of Fluid Mechanics, Vol. 9, pp. 145–185.

Pope, S., 2000. Turbulent Flows. Cambridge University Press, United Kingdom. 771 p. ISBN 978-0-521-59886-6.

Pylkkänen, J., Sánchez-Caja, A., Sundell, T., Piippo, H., 1998. FINFLO RANS solver validation calculations for propeller open water flow and ship hull flow. 2nd International Shipbuilding Conference – ISC'98. 9 p. St. Petersburg, Russia, 24.–26.11.1998.

Rankine, W., 1869. A Manual of Applied Mechanics. 5th Edition, revised. Charles Griffin and Company, Stationers' Hall Court. 648 p.

Rayleigh, J., 1917. On the Pressure Developed in a Liquid During the Collapse of a Spherical Cavity. London, Edinburgh and Dublin Philosophical Magazine, Vol. 34, pp. 94–98.

Reboud, J., Delannoy, Y., 1994. Two-Phase Flow Modeling of Unsteady Cavitation. Proceedings of Second International Symposium on Cavitation. Pp. 39–44. Tokyo, Japan, 5.–7.4.2004.

Reboud, J., Stutz, B., Coutier, O., 1998. Two-Phase Flow Structure of Cavitation: Experiment and Modeling of Unsteady Effects. Proceedings of the Third International Symposium on Cavitation, Vol. 2. Pp. 203–208. Grenoble, France, 7.–10.8.1998.

Rhie, C., Chow, W., 1983. Numerical Study of the Turbulent Flow past an Airfoil with Trailing Edge Separation. AIAA Journal, Vol. 21, No. 11, pp. 1525–1532.

Rott, N., 1958. On the Viscous Core of a Line Vortex. Zeitschrift für Angewandte Mathematik und Physik (ZAMP), Vol. 9b, pp. 543–553.

Saito, Y., Takami, R., Nakamori, I., 2007. Numerical Analysis of Unsteady Behavior of Cloud Cavitation around a NACA0015 Foil. Computer Mechanics, Vol. 40, No. 1, pp. 85–96.

Sánchez-Caja, A., Veikonheimo, T., Pylkkänen, J., 2006a. RANS Predictions for Flow Patterns around a Compact Azipod. Proceedings in 2nd International conference on technical advances in Podded propulsion TPOD2. Paper No. 29. 8 p. Brest, France, 3.–5.10.2006.

Sánchez-Caja, A., Sipilä, T., Pylkkänen, J., 2006b. Simulation of the Incompressible Viscous Flow around an Endplate Propeller Using a RANSE Solver. Proceedings of 26th Symposium on Naval Hydrodynamics, Vol. 3, pp. 137–149. Rome, Italy, 17.–22.9.2006.

Sánchez-Caja, A., 2010. Lecture notes on course Potential Flow Theory for Lifting Surfaces, Aalto University. 152 p.

Sauer, J., Schnerr, G., 2000. Unsteady Cavitating Flow – A new Cavitation Model Based on a Modified Front Capturing Method and Bubble Dynamics. Proceedings of 2000 ASME Fluid Engineering Summer Conference. Pp. 1073–1080. Boston, USA, 11.–15.6.2000.

Saurel, R., Lemetayer, O., 2001. A Multi-Phase Model for Compressible Flows with Interfaces, Shocks, Detonation Waves and Cavitation. Journal of Fluid Mechanics, Vol. 431, pp. 239–271.

Schmidt, S., Sezal, I., Schnerr, G., 2006. Compressible Simulation of High-Speed Hydrodynamics with Phase Change. Proceedings of ECCOMAS CFD. 20 p. Egmond aan Zee, The Netherlands, 5.–8.9.2006.

Senocak, I., Shyy, W., 2004a. Interfacial Dynamics-Based Modeling of Turbulent Cavitating Flows. Part 1: Model Development and Steady-State Computations. International Journal for Numerical Methods in Fluids, Vol. 44, No. 9, pp. 975–995.

Senocak, I., Shyy, W., 2004b. Interfacial Dynamics-Based Modeling of Turbulent Cavitating Flows. Part 2: Time-Dependent Computations. International Journal for Numerical Methods in Fluids, Vol. 44, No. 9, pp. 997–1016.

Siikonen, T., 1987. Numerical Method for One-Dimensional Two-Phase Flow. Numerical Heat Transfer, Part B: Fundamentals, Vol. 12, No. 1, pp. 1–18.

Siikonen, T., Hoffren, J., Laine, S., 1990. A Multigrid LU Factorisation Scheme for the Thin-Layer Navier-Stokes Equations. Proceedings of the 17th ICES Congress, Vol. 90, No. 6. Pp. 2023–2034. Stockholm, Sweden, 9.–14.9.1990.

Siikonen, T., Pan, H., 1992. Application of Roe's Method for the Simulation of Viscous Flow in Turbomachinery. Proceedings of the First European Computational Fluid Dynamics Conference ECCOMAS. Elsevier Science Publischers B.V., Computational Fluid Dynamics '92, Vol 2. Pp. 635–641. Brussels, Belgium, 7.–11.9.1992.

Siikonen, T., 1995. An Application of Roe's Flux-Difference Splitting for k-e Turbulence Model. International Journal for Numerical Methods in Fluids, Vol. 21, pp. 1017–1039.

Siikonen, T., 2006. Lecture notes on course Virtaussimulointi (Simulation of Fluid Flows), Aalto University. In Finnish.

Siikonen, T., Reksoprodjo, H., Miettinen, A., 2008. Continued Development of Two-Phase Modelling in FINFLO. Project report D4.3.5b in 6th Framework Programme project VIRTUE, Project 516201, TIP5-CT-2005-516201. 24 p.

Siikonen, T., 2011. Developments in Pressure Correction Methods for a Single and Two Phase Flow. Aalto University, CFD-Group, Memo No CFD/MECHA-10-2011. 63 p., in preparation.

Singhal, A., Athavale, M., Li, H., Jiang, Y., 2002. Mathematical Basis and Validation of the Full Cavitation Model. Journal of Fluids Engineering, Vol. 124, pp. 617–624.

Sipilä, T., Martio, J., 2008. FINFLO Analysis of Cavitating and Non-cavitating Propeller Flows in Uniform and Non-uniform Inflow. VIRTUE WP4 Workshop II on Propeller RANS Calculations. 44 p. Rome, Italy, 29.–30.10.2008.

Sipilä, T., Siikonen, T., 2012. RANS predictions of a cavitating tip vortex. Proceedings of the 8th International Symposium on cavitation CAV2012, Paper No. 61. 6 p. Singapore, USA, 13.–16.8.2012.

Sipilä, T., Siikonen, T., Saisto, I., Martio, J., Reksoprodjo, H., 2009. Cavitating Propeller Flows Predicted by RANS Solver with Structured Grid and Small Reynolds Number Turbulence Model Approach. Proceedings of the 7th International Symposium on cavitation CAV2009, Paper No. 45. 11 p. Ann Arbor, USA, 17.–22.8.2009.

Sipilä, T., Siikonen, T., Saisto, I., 2011. FINFLO RANS-Predictions for Propeller Performance. Proceedings of Second International Symposium on Marine Propulsors smp'11, Workshop: Propeller performance. Pp. 114–121. Hamburg, Germany, 17.–18.6.2011.

Smagorinsky, J., 1963. General Circulation Experiments with the Primitive Equations: I. The Basic Equations. Monthly Weather Review, Vol. 91, pp. 99–164.

van Terwisga, T., Fitzsimmons, P., Ziru, L., Foeth, E.-J., 2009. Cavitation Erosion – A Review of Physical Mechanisms and Erosion Risk Models. Proceedings of the 7th International Symposium on Cavitation CAV2009, Paper No. 41. 13 p. Ann Arbor, USA, 17.–22.8.2009.

Ubbink, O., 1997. Numerical Prediction of Two Fluid Systems with Sharp Interfaces. Ph.D. Thesis, Imperial College of Science, Technology & Medicine. 137 p.

Wallis, G., 1969. One-Dimensional Two-Phase Flow. McGraw-Hill Book Company. 408 p.

White, F., 1991. Viscous Fluid Flow. 2nd Edition. McGraw-Hill Book Co., Singapore. 614 p. ISBN 0-07-100995-7.

Wu, J.-Z., Ma, H.-Y., Zhou, M.-D., 2006. Vorticity and Vortex Dynamics. Springer. 780 p. ISBN-10 3-540-29027-3.

Yuan, W., Sauer, J., Schnerr, G., 2001. Modeling and Computtation of Unsteady Cavitation Flows in Injection Nozzles. Mécanique & industries, Vol. 2, pp. 383–394.

Zwart, P., Gerber, A., Belamri, T., 2004. A Two-Phase Flow Model for Predicting Cavitation Dynamics. Proceedings of ICFM 2004 International Conference on Multiphase Flow, Paper No. 152. 11 p. Yokohama, Japan, 30.5.–3.6.2004.

Series title and number
VTT Science 22

Title	**RANS analyses of cavitating propeller flows**
Author(s)	Tuomas Sipilä
Abstract	This publication presents validation studies for the cavitation model implemented in the Reynolds-averaged Navier-Stokes equation solver FINFLO. The validation studies relate to ship propellers in uniform and non-uniform inflow conditions. The main physical phenomena involved in cavitation are first introduced. Then, the cavitation phenomena related to marine applications are presented, and the physics behind sheet and vortex cavitation are explained. As cavitating flows are strongly related to turbulence, the physics behind turbulence and its simulation methods are also introduced. The benefits and uncertainties related to cavitation tests are described. It is important to understand the drawbacks of experimental methods when comparing the simulation results with the test observations. A brief description of the existing cavitation models is also given, and the utilized cavitation model and its numerical implementation are described in detail. The validation cases are introduced and the simulation results are compared to the outcome of the cavitation tests. The simulation results generally showed good correlation with the experiments. Sheet cavitation was observed in the tests on both the suction and pressure sides of the blades in the validation cases, which was also found in the simulations. The cavitating tip vortices were also found to be similar in the experiments and simulations. The propeller slipstream must be discretized with a high resolution grid in order to predict the cavitating tip vortices and the wakes of the blades with reasonable accuracy. A verification and validation analysis was performed for the global propeller performance characteristics according to the methodology recommended by the ITTC. The influence of the empirical constants in the utilized mass transfer model on the cavitating tip vortices is studied. Finally, explanations for the similarities and differences between the results of the experiments and the simulations are discussed. The main differences are found to be caused by laminar flow separation at the leading edge of the blades in the tests, and the limitations of the turbulence and cavitation models utilized in the present simulations.
ISBN, ISSN	ISBN 978-951-38-7946-4 (soft back ed.) ISSN 2242-119X (soft back ed.) ISBN 978-951-38-7947-1 (URL: http://www.vtt.fi/publications/index.jsp) ISSN 2242-1203 (URL: http://www.vtt.fi/publications/index.jsp)
Date	October 2012
Language	English, Finnish abstract
Pages	136 p.
Name of the project	VIRTUE, VIRKOOT, CFDShip, UNNO
Commissioned by	EU, Tekes, VTT, FIMECC
Keywords	Cavitation, CFD, hydrodynamics, propeller, RANS, simulation, tip vortex, turbulence
Publisher	VTT Technical Research Centre of Finland P.O. Box 1000, FI-02044 VTT, Finland, Tel. 020 722 111

Julkaisun sarja ja numero
VTT Science 22

Nimeke	**Kavitoivien potkurivirtausten RANS-analyysi**
Tekijä(t)	Tuomas Sipilä
Tiivistelmä	Työssä on esitetty validointilaskentaa Reynolds-keskiarvoistettujen Navier-Stokes-yhtälöiden ratkaisijaan FINFLOhun implementoituun kavitaatiomalliin. Validointilaskennat liittyvät laivapotkurisovelluksiin sekä tasaisessa että epätasaisessa sisääntulovirtauksessa. Kavitaatioon liittyvät tärkeimmät fysikaaliset ilmiöt on selitetty opinnäytteen alussa. Tämän jälkeen on esitetty laivasovelluksissa esiin tulevat kavitaatioilmiöt. Levy- ja kärkipyörrekavitaation fysiikka on selitetty tarkasti. Koska kavitaatio liittyy läheisesti virtauksen turbulenttisuuteen, on myös turbulenssin fysiikka ja sen simulointi- ja mallinnusmenetelmät kuvattu. Kavitaation kokeelliseen tutkimukseen liittyvät edut ja epävarmuudet ovat myös esitetty. On tärkeää ymmärtää kokeelliseen toimintaan liittyvät epävarmuudet, kun verrataan kavitaation simulointituloksia koetuloksiin. Olemassa olevia erilaisia kavitaatiomalleja on lyhyesti kuvattu. Työssä käytetty kavitaatiomalli ja sen numeerinen implementointi on selitetty yksityiskohtaisesti. Validointitapaukset on esitetty ja simulointituloksia on verrattu kavitaatiokokeiden tuloksiin. Simulointitulokset ovat yleisesti ottaen lähellä kokeellisia tuloksia. Kokeissa ja laskennassa levykavitaatiota havaittiin sekä imu- että painepuolilla lapaa eri validointitapauksissa. Kavitoiva kärkipyörre oli samankaltainen kokeissa ja simulointituloksissa. Jättövirtauksen diskretointi on tehtävä huolellisesti laskennoissa, jotta kavitoiva kärkipyörre sekä lavan vanavesi tulevat mallinnettua tarkoituksenmukaisella tarkkuudella. Lasketuille potkurin toimintaa kuvaaville globaaleille suureille on tehty verifiointi- ja validointitarkastelu ITTC:n suosittelemalla tavalla. Käytetyssä massansiirtomallissa olevien empiiristen kertoimien vaikutusta kavitoivan kärkipyörteen laskentatuloksiin on myös tutkittu. Työn lopussa on selitetty syitä kokeellisten ja laskennallisten tulosten vastaavuuksiin ja eroihin. Tärkeimmät syyt tulosten eroihin ovat levykavitaation synnyn viivästyminen kokeissa lavan johtoreunalla ilmenevän laminaarisen virtauksen johdosta sekä simuloinnissa käytettyjen turbulenssi- ja kavitaatiomallien rajoitukset.
ISBN, ISSN	ISBN 978-951-38-7946-4 (nid.) ISSN 2242-119X (nid.) ISBN 978-951-38-7947-1 (URL: http://www.vtt.fi/publications/index.jsp) ISSN 2242-1203 (URL: http://www.vtt.fi/publications/index.jsp)
Julkaisuaika	Lokakuu 2012
Kieli	Englanti, suomenkielinen tiivistelmä
Sivumäärä	136 s.
Projektin nimi	VIRTUE, VIRKOOT, CFDShip, UNNO
Toimeksiantajat	EU, Tekes, VTT, FIMECC
Avainsanat	Cavitation, CFD, hydrodynamics, propeller, RANS, simulation, tip vortex, turbulence
Julkaisija	VTT PL 1000, 02044 VTT, Puh. 020 722 111

VTT Technical Research Centre of Finland is a globally networked multitechnological contract research organization. VTT provides high-end technology solutions, research and innovation services. We enhance our customers' competitiveness, thereby creating prerequisites for society's sustainable development, employment, and wellbeing.

Turnover: EUR 300 million
Personnel: 3,200

VTT publications

VTT employees publish their research results in Finnish and foreign scientific journals, trade periodicals and publication series, in books, in conference papers, in patents and in VTT's own publication series. The VTT publication series are VTT Visions, VTT Science, VTT Technology and VTT Research Highlights. About 100 high-quality scientific and professional publications are released in these series each year. All the publications are released in electronic format and most of them also in print.

VTT Visions

This series contains future visions and foresights on technological, societal and business topics that VTT considers important. It is aimed primarily at decision-makers and experts in companies and in public administration.

VTT Science

This series showcases VTT's scientific expertise and features doctoral dissertations and other peer-reviewed publications. It is aimed primarily at researchers and the scientific community.

VTT Technology

This series features the outcomes of public research projects, technology and market reviews, literature reviews, manuals and papers from conferences organised by VTT. It is aimed at professionals, developers and practical users.

VTT Research Highlights

This series presents summaries of recent research results, solutions and impacts in selected VTT research areas. Its target group consists of customers, decision-makers and collaborators.

RANS analyses of cavitating propeller flows

Cavitation is an important and complex phenomenon in ship propeller flows. Cavitation induces vibrations to the ship structures, and noise to the interior of the ship and to the environment encumbering people on board and underwater fauna. Cavitation may also cause erosion to propellers, rudders, and other ship structures limiting the service time of vessels.

This publication discusses numerical modelling of cavitation incepting in propeller flows. The cavitation model implemented in FINFLO, a general purpose CFD code, has been validated for quasi-steady and time-dependent propeller flow problems. The validation of the numerical model has been performed against model test results performed in cavitation tunnels. The results of the implemented numerical model and the tests are found to have good correlation.

CFD-based methods give a way to understand the physics inside the cavities more deeply. Numerical investigations of cavitating propeller flows in the early propulsor and ship design stage help to decrease the noise and vibration levels of vessels.

ISBN 978-951-38-7946-4 (soft back ed.)
ISBN 978-951-38-7947-1 (URL: http://www.vtt.fi/publications/index.jsp)
ISSN 2242-119X (soft back ed.)
ISSN 2242-1203 (URL: http://www.vtt.fi/publications/index.jsp)